Biorheology (Part I) & Numerical Investigation of Flow-Induced Vibration (Part II)

By

Harsa Mitra

A thesis submitted to the Department of Mechanical Engineering,

Cullen College of Engineering

in partial fulfillment of the requirements for the degree of

MASTER OF SCIENCES

in Mechanical Engineering

Chair of Committee: Dr. Rodolfo Ostilla Mónico

Co-Chair of Committee: Dr. Kamran Alba

Committee Member: Dr. Ralph Metcalfe

Committee Member: Mr. Frank Koeck

University of Houston

May 2020

Dedication

Dedicated to my maa, baba,

and to the loving memory of my grandaunt, Nilima Dutta,

my grandfather Jitendra Lal Mitra,

and my brother Iman Maity.

Acknowledgements

First of all, I would like to thank my advisors, Dr. Kamran Alba and Dr. Rodolfo Ostilla Mónico, for providing me with the opportunity to work on the research projects during my Master's program. I am very grateful to the collaborators at Baylor College of Medicine, Dr. Prathap Jayaram and Andrew Bratsman for their collective efforts and constructive discussions to make the research biorheology research possible. I would also like to extend my thankfulness to Mr. Frank Koeck, Mr. Dan Williams, and the whole team at Master Flo Valve (USA) Inc. for their continuous help and support in the flow-induced vibration research. Special thanks to Dr. Alba for his advice and support, for which I have developed a sense of adventure in regards to complex fluids research, a quality which I forever will carry in my scientific endeavors. Thank you very much for your invaluable support and guidance.

Also, members of the Complex Fluids lab for providing me with an enjoyable environment to work in, especially, Gaarthick Ravichandran, Nima Mirzaeian, Trevor Gabel, Olamide Oladosu and several others for sharing their ideas and valuable inputs which immensely helped me in completing my thesis. I would like to express my thankfulness to Dr. Amit Amritkar and the staff at the Research Computing Data Core (RCDC) of the University of Houston and the STAR-CCM+ team at SIEMENS for their suggestions and technical support with the simulations. I am thankful to my thesis committee members, Dr. Ralph Metcalfe and Mr. Frank Koeck for taking a keen interest in my work and their valuable comments. Finally, I would like to mention that this thesis would not have been possible without the continuous ideas and assistance from Trevor Gabel and also would like to specially thank my family, friends and amazing roommates, who were and are always there for me when I need them the most. I am very grateful to everyone who has helped me to get to this level.

Abstract

This Master's thesis work is composed of two research categories. The first part seeks to develop a better understanding of the rheological properties of platelet-rich plasma (PRP), a blood-derived product used as a therapy for osteoarthritis and tendon injuries and the second part aims at evaluation of the flow-induced vibration (FIV) within a subsea choke valve. Blood-derived products, particularly PRP, have received increased attention in the past several years due to their great potential as a therapy for osteoarthritis and tendon injuries. Therefore, characterizing the mechanical properties of PRP becomes important to better understand its therapeutic efficacy. Rheological characterization of PRP provides further insight into its mechanism of action. Flow-sweep, Small Amplitude Oscillatory Shear (SAOS), Large Amplitude Oscillatory Shear (LAOS), and thixotropy tests have been performed at room and physiological temperatures to characterize the non-Newtonian properties of PRP samples. Flow-sweep tests reveal shear-thinning behavior (also observed in LAOS experiments), with higher apparent viscosity observed at temperature. Rheological models such as Carreau, Casson, power-law, and Herschel-Bulkley have been fitted to the flow-sweep data with the latter showing the closest agreement. The calculated boundaries of low/high-shear rates in flow-sweep tests as well as minimum-torque, sample-inertia, and instrument-inertia limits in SAOS frequency-sweep experiments are correspondingly provided for accurate interpretation of the results. Although, the window of interpretable SAOS results is found to be narrow. Furthermore, the non-linear and transient viscoelasticity is quantified with the help of the LAOS tests. The thixotropic behavior of PRP solutions is further quantified through the peak-hold test, and further compared against the results of whole blood previously published in the literature. Part two of the thesis investigates a wellhead choke valve, a type

of control valve, which is mostly used to control the flow and pressure of fluids from a reservoir in an oil and gas production. A numerical study is performed using STAR-CCM+ software to study and visualize the complex physics of the compressible flow in question. Our study is carried out on a subsea choke valve model obtained from Master Flo Valve (USA) Inc., FIV investigation on dominant frequency modes within the flow has been conducted using fast-Fourier transform (FFT). The dominant frequency is then compared against the experimental natural frequency of vibration of the valve assembly to assess the risk of resonance and mechanical failure. To complement the FFT analysis, the Mach number, pressure, and temperature contours have been presented on three orthogonal planes within the valve.

Table of Contents

List of Tables

List of Figures

Nomenclature

Part I: Dimensional

$\hat{\lambda}$	Relaxation time
$\hat{\dot{\gamma}}$	Shear rate (strain rate)
$\hat{\eta}$	Apparent viscosity
$\hat{\eta}_0$	Zero-shear viscosity
$\hat{\eta}_{ideal}$	Ideal apparent viscosity due to sole shear flow
$\hat{\eta}_\infty$	Infinite-shear viscosity
$\hat{\kappa}$	Flow consistency index
$\hat{\lambda}_{wave}$	Wavelength of the propagating wave in a sample
$\hat{\rho}$	Density
$\hat{\tau}$	Stress
$\hat{\tau}_0$	Herschel-Bulkley yield stress or the wall shear stress as when specified
$\hat{A}$	Differential area of the rheometer geometry or otherwise specified
$\hat{B}$	Binormal vector
$\hat{F}_\tau$	Minimum torque limit coefficient
$\hat{G''}$	Loss modulus
$\hat{G'}$	Storage modulus

$\hat{G'}_L$	Large strain elastic shear modulus
$\hat{G'}_M$	Minimum strain elastic shear modulus
$\hat{G}$	Complex modulus
$\hat{G}''_t(\hat{t})$	Dynamic non-linear viscous response modulus
$\hat{G}'_t(\hat{t})$	Dynamic non-linear elastic response modulus
$\hat{H}$	Gap height of the rheometer geometry
$\hat{I}$	Combined inertia of the rheometer and its geometry
$\hat{R}$	Radius of the rheometer geometry
$\hat{r}$	Radial location on the rheometer geometry
$\hat{T}$	Temperature/Torque as when specified
$\hat{t}$	Time
$\hat{T}_0$	Ideal torque due to shear flow in the rheometer geometry
$\hat{T}_{\text{min}}$	Minimum measurable torque by the rheometer
$\hat{\eta}'_M$	Large-rate dynamic viscosity
$\hat{\eta}'_M$	Minimum-rate dynamic viscosity

Part II: Dimensional

$\Delta\hat{t}$	Physical time step
$\hat{\bar{u}}_i$	Mean flow velocity
$\hat{\beta}$	Coefficient of thermal expansion

$\hat{\Delta}$	Largest distance between the cell center under consideration and the cell centers of the neighboring cells around it in for the finite volume scheme
$\hat{\dot{m}}_f$	Mass flow rate at a cell face
$\hat{\epsilon}$	Turbulent energy dissipation rate
$\hat{\Gamma}$	Face diffusivity across a polyhedral cell face
$\hat{\Gamma}_f$	Harmonic average of face diffusivity from the cells
$\hat{\hat{c}}$	Speed of sound
$\hat{\kappa}_c$	Thermal conductivity
$\hat{\mu}$	Enthalpy of an expansion process
$\hat{\mu}_t$	Turbulent eddy viscosity
$\hat{\mu}_J$	Joule-Thomson coefficient
$\hat{\phi}$	A conserved quantity
$\hat{\phi}_{MUSCL3}$	Reconstructed value of a conserved quantity from the MUSCL3 scheme
$\hat{\rho}$	Density
$\hat{\hat{\mu}}$	Modified diffusivity
$\hat{\varphi}$	Normalized amplitude of the resonant frequency
$\hat{a}$	Variable cross sectional area of a duct
$\hat{a}_f$	Surface area vector for a polyhedral cell face in the finite volume method
$\hat{C}$	Specific heat capacity
$\hat{C}_p$	Specific heat capacity of the gas at constant pressure

$\hat{C}_v$	Specific heat capacity of the gas at constant volume
$\hat{d}$	Dimensionless distance to the wall
$\hat{f}$	A polyhedral cell face in the finite volume method
$\hat{k}$	Turbulent kinetic energy
$\hat{l}_{LES}$	LES length scale for DDES SST $\hat{k}-\hat{\omega}$ model
$\hat{l}_{RANS}$	RANS length scale for DDES SST $\hat{k}-\hat{\omega}$ model
$\hat{l}_{ratio}$	Ratio of RANS and LES length scale in context to the DDES SST $\hat{k}-\hat{\omega}$ model
$\hat{M}_w$	Mean molecular weight of the gas
$\hat{P}$	Pressure
$\hat{p}^*$	Pressure at a restriction within a duct
$\hat{p}_0$	Upstream pressure
$\hat{P}_\omega$	Sum of specific dissipation production and the cross diffusion term
$\hat{p}_c$	Critical pressure of a gas
$\hat{P}_k$	Sum of the turbulent and buoyancy production
$\hat{p}_{exit}$	Exit pressure at nozzle outlet
$\hat{Q}_G$	Gas flow in standard cubic feet per hour
$\hat{R}_{ij}$	Reynolds stress tensor
$\hat{R}_s$	Specific gas constant
$\hat{R}_u$	Ideal gas constant

$\hat{S}$	Modulus of the mean rate of strain tensor
$\hat{S}_{ij}$	Mean rate of strain tensor
$\hat{T}_c$	Critical temperature
$\hat{U}$	Flow velocity within a duct
$\hat{V}$	Control volume
$\hat{u}_i'$	Fluctuating velocity
$\hat{V}_g$	Gas velocity

Part I: Dimensionless

δ	Phase angle between stress and strain
γ	Strain
γ_1	Maximum strain amplitude in a cycle during large amplitude oscillatory test
$\hat{\omega}$	Angular frequency
$\hat{\omega}$	Dissipation rate per unit turbulent kinetic energy
ϕ	Volume fraction
F_γ	Ratio of the rheometer geometry radius and the gap height
n	Harmonic of the frequency domain of fast-Fourier transform or unless specified
Re_{crit}	Critical Reynolds number for secondary flow limit
S	Strain-stiffening ratio

T	Shear-thickening ratio
θ	Angular displacement

Part II: Dimensionless

β^*	Model coefficient for $\hat{k}-\hat{\omega}$ scheme
δ_{ij}	Kronecker delta
γ	Specific heat ratio
$\hat{\omega}$	Dissipation rate per unit turbulent kinetic energy
ω	Accentric factor
ψ	Field variation factor for the total variation bounded gradient limiting scheme within MUSCL3
σ_{MUSCL3}	User defined model parameter used to control the numerical dissipation in MUSCL3 scheme
ξ	Normalized-Variable Diagram value
ζ	Damping factor/damping ratio of the mechanical system
$C_{DES,\hat{k}-\hat{\epsilon}}$	Independent calibration value of $\hat{k}-\hat{\epsilon}$ within the DDES SST $\hat{k}-\hat{\omega}$ model
$C_{DES,\hat{k}-\hat{\omega}}$	Independent calibration value of $\hat{k}-\hat{\omega}$ within the DDES SST $\hat{k}-\hat{\omega}$ model
C_{DES}	Model coefficient used for blending $\hat{k}-\hat{\epsilon}$ and $\hat{k}-\hat{\omega}$ parts of the SST $\hat{k}-\hat{\omega}$ model
C_D	Coefficient of discharge
C_{v1}	Spalart-Allamaras model coefficient

C_v	Valve flow coefficient
$CD_{k\omega}$	Non-conservative cross-diffusion term for the Menter's Shear Stress Transport $\hat{k}-\hat{\omega}$ model
F_1	Blending function for $\hat{k}-\hat{\omega}$ scheme
f_{β^*}	Free-shear modification factor for the DDES SST $\hat{k}-\hat{\omega}$ model
M	Mach number
p_{cr}	Critical pressure ratio
P_r	Pressure ratio
Re	Reynolds number
Re_τ	Friction Reynolds number
T_r	Temperature ratio
y^+	Viscous wall unit

Part I

Biorheology

1. Introduction

“ It is probable that the scheme of physics will be enlarged so as to embrace the behaviour of living organisms under the influence of life and mind. ”

—Oliver Joseph Lodge

1.1 Motivation

The complex nature of fluids in biological systems can be astonishing, even at their smallest of scales. As described by S. E. Spagnolie [1], these fluids and the systems formed by them are actively functional, heterogeneous, and comprises of a vast spectrum of length and time scales. The complexity of such fluids makes the measurement of their properties tedious and difficult. Since, the physical properties of biological fluids are key to their mechanism of action, i.e., physiological functioning, a mechanical outlook is vital in order to fully understand their behaviour. It requires a coupled understanding of physical and biological aspects of such fluids to be able to describe the complex properties. Moreover, the fluids in the human body are mostly non-Newtonian in nature, therefore, rheology takes a center stage in terms of describing their properties. Since most biological soft matter/fluids have both elastic and viscous properties, i.e., viscoelastic in nature, the use of various types of rheological tests are mandated. It is interesting to note that, given the simple platform of rheological tests, often times these measurements are not critically examined [2]. Since, basic rheology is a fundamental tool used by biologists and physicists, a more critical outlook is suggested which will be laid out later in chapter 4.

The human whole blood (WB), as an important non-Newtonian fluid, has been studied from rheological standpoint since the first half of the 21^{st} century [3]. A large

body of work exists in the literature in regards to rheology of human WB, also known as hemorheology [4–14]. Similarly, since several of blood-derived products have been clinically utilized as a therapy for a number of pathologies [15], rheological characterization of such fluids has become noticeably important. More recently, platelet-rich plasma (PRP) [16] is being used to restore tissue healing in musculoskeletal injuries [17, 18]. PRP may undergo a range of mechanical forces due to walking and/or running motion once injected into the knee space; see Refs. [19, 20] for other applications. But, unlike human WB there are only a few studies performed on PRP rheology. For instance, the recent works of Russo *et al.* [21] and Vadal *et al.* [22] have considered both biological and rheological evaluation of PRP for treatment of Osteoarthritis (OA), however, these studies evaluated PRP when blended with Hyaluronic Acid (HA) (HA -optimal gelation kinetics exploration). Due to its gelatinous properties, HA completely alters the elasto-viscoplastic behavior of PRP [23]. In addition to that, to elucidate the suitability of PRP, i.e. PRP-Hyaluronic Acid (HA) mixtures, as a visco-supplement for the synovial fluid [24] *in-vivo*, evaluating the rheological properties of the PRP becomes important.

1.2 Thesis Statement

The first part of the thesis is aimed at describing the utilization of shear (rotational) rheology in investigating the mechanical properties of solely PRP used in treatment of OA. Along with the flow-sweep tests, Small Amplitude Oscillatory Shear (SAOS) tests are carried out at two different strain rates to evaluate the linear viscoelastic behavior of the samples at room and physiological temperature. In a recent study by Sousa *et al.* [8], they investigate whole blood (WB) behaviour in Large Amplitude Oscillatory Shear (LAOS) range, reinforcing the concept of transient rheology of blood and existence of non-linear viscoelasticity (higher harmonics). A more recent study by Horner *et al.* [10], also concluded the existence of higher harmonics in the stress

response of WB, further confirming the non-linear behaviour in such complex fluid. It is worth noting that the non-linear behavior is highest for the third harmonic in unidirectional (ud)-LAOS [25, 26]. More recently, Saengow *et al.* [27] performed (ud)-LAOS and presented the existence of fractional harmonics within the transient shear stress response of WB. Therefore, following the experimental protocol of Sousa *et al.* [8], LAOS tests are performed to evaluate the non-linear viscoelastic response of PRP solutions [25, 28]. Additonally, an important feature of blood is its thixotropy [7, 29], i.e., decrease in apparent viscosity over time. The steady shear kinetics have been obtained at low shear range to quantify possible thixotropic behaviour of PRP. Hysteresis analysis for PRP remains to be further investigated using a triangular ramp test at low shear rates as evaluated for blood [13, 14, 30]. Sample preparation technique is described in Section 3 followed by corresponding cell counts and volume fraction of solutions given in Appendix A.1. Rheological results are discussed next in Section 4. Section 5 contains the conclusions drawn from the experiments performed in this study.

1.3 Platelet-Rich Plasma

PRP is an autologous WB, which contains an increased number of platelets and a wide variety of cytokines, i.e., growth factors. Platelets, which have high concentrations in PRP, are small anuclear fragments of cytoplasm produced by megakaryocytes [15]. In recent years, research studies have found evidence that makes platelets far more complex than it was previously considered. Platelets are equipped with intricate intra-cellular mechanisms, with the capability to interact with most immune cells [31–33]. Typically, the platelet concentration in PRP can go up to five times higher (called 5X PRP) than the normal platelet concentration in a healthy person's blood [18]. Within PRP, platelets serve as an abundant source of bioactive molecules that are thought to participate in tissue repair [17, 34]. PRP is thought to alter many

of the participating processes, including inflammation, and potentially regulate the balance between anabolic and catabolic mediators [15]. PRP preparations can be characterized by their concentration of platelets, red blood cells (RBC), and white blood cells (WBC). Clinically, PRP samples are, in part, largely differentiated by their leukocyte content [35], namely leukocyte-rich PRP (LR-PRP), and leukocyte-poor PRP (LP-PRP). The experiments in this thesis are carried out using both LP-PRP and LR-PRP which may also have higher erythrocytes concentration compared to average PRP [34, 36]. Whether the inflammation caused by LR-PRP facilitates the healing process is still being debated. Note that LR-PRP can have adverse effects on patients with metabolic syndromes i.e. overweight, high blood pressure, and high triglycerides [37–39]. The PRP injections performed on the knee are typically carried out in a superior-lateral position with the patient supine; entering the supra-patellar recess of the knee joint. A wide range of PRP volume is used for these injections, which can fall in the range from 1 ml to 10 ml.

A comprehensive study of the flow properties of joint fluids in patients undergoing Total Knee Arthroplasty (TKA) is presented by Mazzucco *et al.* [40]. The decrease in apparent viscosity of the joint fluids with increase in shear rate have been evaluated. Linear viscoelastic properties are also measured and it was concluded that there was a crossover of the elastic modulus over the loss modulus within the frequency range of walking and running. In other words, in a healthy joint, synovial fluid has higher viscosity at low shear rates and higher elasticity at high shear rates. Such viscoelastic property allows the knee to protect Articular Cartilage (AC) from wearing down [41]. Additionally, Bhuanantanondh *et al.* [42] concluded that synovial fluid in OA exhibits non-Newtonian shear-thinning behavior and viscoelastic properties. They, moreover, report that OA synovial fluid exhibits rheopectic behavior at a physiological temperature of 37°C. Although, the biomechanics of the knee joint [43] and the synovial fluid between the AC [44] have been well described, there is a lack of knowledge on

the rheology of PRP within the joint cavity.

2. Theory

2.1 Non-Newtonian Fluids

Unlike Newtonian fluids, non-Newtonian fluids have the viscous shear stresses generated within the fluid depend nonlinearly on the shear rate. Additionally, the fluid can also have dependence over the time history of the shear rate. Therefore, this dynamic viscosity needs to be defined with the help of models having more parameters than that of simple Newtonian fluid. Based on the behaviour of the dynamic viscosity of a non-Newtonian fluids, six broad classification have been defined. The fluid is termed as a *shear-thinning* or *shear-thickening* in nature when the viscosity decreases or increases as shear rate increases. Additionally, for some fluids there exists a minimum shear stress threshold, known as the yield stress. This stress must be exceeded in order to make the fluid flow or deform under shear. Fluids exhibiting such behaviour are termed as *viscoplastic* in nature and will deform purely elastically if the applied stress is less than the yield stress. Similarly, a non-Newtonian viscous behaviour can be accompanied by elastic behaviour, i.e., the fluid can be *viscoelastic* in nature, when undergoing deformation. Most biological fluids are viscoelastic in nature. Moreover, the viscosity at a constant applied shear rate can also be time-dependent. To classify this behaviour, at a constant applied shear rate, *thixotropic* fluids have an apparent decrease in viscosity over time and *rheopectic* fluids show an increase in viscosity over time. Therefore, the rheological behaviour of a material can be described in terms of it's elasticity, viscosity dependence on shear rate, and viscosity dependence on time. A good example of such a fluid is human WB itself, which is a shear thinning, elasto-viscoplastic, i.e., both viscoelastic and viscoplastic, and thixotropic fluid.

Therefore, in order to quantify the non-Newtonian behavior of five PRP samples,

we have used various rheological models to fit to the experimental data; e.g., see Fig. 4.3. Power-law model can be described by [1]

$$\hat{\tau} = \hat{\kappa}\hat{\dot{\gamma}}^n, \tag{2.1}$$

where $\hat{\kappa}$ is the flow consistency index and n is the flow behavior index. The Carreau model can be described as follows

$$\hat{\eta} = \hat{\eta}_\infty + (\hat{\eta}_0 - \hat{\eta}_\infty)[1 + (\hat{\lambda}\hat{\dot{\gamma}})^2]^{(n-1)/2}, \tag{2.2}$$

where $\hat{\lambda}$, $\hat{\eta}_0$, $\hat{\eta}_\infty$, and n are the relaxation time, the viscosity at zero-shear rate, the viscosity at Infinite-shear rate, and power index respectively. Herschel-Bulkley (HB) model is described as

$$\hat{\tau} = \hat{\tau}_0 + \hat{\kappa}\hat{\dot{\gamma}}^n, \tag{2.3}$$

where $\hat{\kappa}$, $\hat{\tau}_0$, n are the consistency index, HB yield stress, and the flow index respectively. Finally, the Casson model can be shown in a similar way as

$$\sqrt{\hat{\tau}} = \sqrt{\hat{\tau}_0} + \sqrt{\hat{\kappa}_c\hat{\dot{\gamma}}}, \tag{2.4}$$

where, $\hat{\kappa}_c$ and $\hat{\tau}_0$ are the Casson plastic viscosity and Casson yield stress respectively. Previously, the Casson model has been used to capture WB behavior through reversible aggregation of erythrocytes and rouleaux formation at low shear rates [3]. The corresponding fitting parameters as well as R^2 values obtained using MATLAB software are provided in Tables A.3-A.6 at both 25°C and 37°C temperatures. It should be noted that due to a wide range of fitting parameters involved in the Carreau model, error bounds can diverge significantly which are not meaningful to report.

[1] The dimensional and dimensionless parameters adopted in this thesis are consistently denoted with and without a $\hat{}$ symbol respectively.

Over a Hematocrit(Hct) range of 30% -95%, the yield stress of WB is reported to be of the orders 1 mPa -30 mPa [45]. Rheological measurements can be affected by various factors as explained and quantified in outstanding work of Ewoldt *et al.* [2]. The boundaries between which reliable results can be obtained are often fine and need to be dealt with carefully. In the sections 4.1.1, 4.1.2, 4.2.1, 4.2.2, and 4.2.3 we discuss the limits that one needs to be aware of in interpreting the rheological results.

2.2 Linear Viscoelasticity

Small amplitude oscillatory shear (SAOS) is a non-destructive test that is used to evaluate the structural changes of the material, i.e., viscoelasticity [46]. Unlike purely elastic substances, viscoelastic materials possess a time delay in response to a stimulus, and there is a loss of energy within the material itself which is quantified by the loss modulus, $\hat{G''}$. Similarly, for quantifying the elastic behaviour or the property of the material to store some of the energy, the storage modulus, $\hat{G'}$, is defined. As a result, the strain and stress relation in a viscoelastic fluid/material can be defined as

$$\gamma = \gamma_0 \sin(\hat{\omega}\hat{t}), \hat{\tau} = \hat{\tau}_0 \sin(\hat{\omega}\hat{t} + \delta), \tag{2.5}$$

where, $\hat{t}$, is time and, δ, is the phase angle between stress and strain. The viscous nature of a viscoelastic material enforces a strain rate dependence on time. On the other hand, unlike a purely elastic material, a viscoelastic material experiences a loss of energy when external stress is applied. This behaviour is also accompanied by hysteresis, which can be evaluated from the area within the stress-strain loop, which is equal to the energy dissipated. Hence, for a purely elastic solid, $\delta = 0$, and for a purely viscous fluid, $\delta = 90°$. For quantifying the elastic part, $\hat{G'}$, is defined which can be described as:

$$\hat{G'} = \frac{\hat{\tau}_0}{\gamma_0} \cos\delta, \tag{2.6}$$

and the viscous part is defined using, $\hat{G}''$, as:

$$\hat{G}'' = \frac{\hat{\tau}_0}{\gamma_0} \sin \delta, \tag{2.7}$$

which gives rise to the complex modulus, $\hat{G}$,

$$\hat{G} = \hat{G}' + i\hat{G}''. \tag{2.8}$$

The complex modulus, $\hat{G}$, is able to capture the material response to a stimuli. When the complex modulus is independent of the amplitude of applied stress/strain, the response is termed as linear viscoelasticity. Therfore, if a perfectly sinusoidal stress/strain input is given, the response strain/stress should be a perfect sinusoid. Also, the amplitude of the response should also be linearly proportional to the input stimulus [47]. When these set of criteria are violated, the response is termed as to be non-linear (see Sec: 2.3). In order to evaluate linear viscoelasticity, SAOS tests are carried out. It should be kept in mind that in the case of SAOS, the response of the material is often evaluated at small strains on the order of, $\gamma \approx$ 1% to 100%, [48]. The linear viscoelastic range can be determined by performing a amplitude sweep, i.e., varying the strain amplitude at constant specified stress. This limit is in the orders of, $\gamma \approx$ 1% to 10%, [49] for the case of structural-polymers and melts. Since, linear viscoelasticity is very well described [50], SAOS tests are able to provide very convenient rheological characterization of complex fluids/soft matter.

2.3 Non-linear Viscoelasticity

Non-linear viscoelasticity refers to the material response to large applied strains/stresses. Under such conditions, the material changes its properties undergoing the large deformations and the response is not linearly proportional to the input amplitudes. Although, these non-linearities exist in experiments such as SAOS,

they are insignificant or minute enough to go unmeasured. Hence to evaluate for the non-linear viscoelasticity, LAOS tests are generally performed. In addition to LAOS, other schemes used for similar evaluations, medium amplitude oscillatory shear (MAOS) [51], and extra extra-large amplitude oscillatory shear (XXLAOS) [52] also exist. In this study, the LAOS scheme has been used extensively.

LAOS experiments is performed at large strain amplitudes ($\gamma > 100\%$). Under such conditions, the non-linear viscoelastic properties of complex fluid can be probed [28, 49]. This non-linear rheological response in LAOS can be quantified and correlated with the microstructure of the viscoelastic sample [47, 53]. A number of schemes have been published to analyze and quantify the non-linear oscillatory response. These can be classified into two main categories, *static* schemes and *dynamic* schemes. In the static schemes such as the one shown by Ewoldt *et al.* [53], Fourier transformation (FT) and power series expansions are used, in which the measured response is represented as a static point in the derived parameter space. The results of the analyses produced from such a static scheme somewhat represent an average, over a period. On the other hand, the sequence of physical processes (SPP) scheme as described by Rogers *et al.* [54, 55] is a dynamic framework providing cycle-dependent information through the specified parameter space. Therefore, as compared to static schemes, which cloak the transient changes (over a period) in the viscoelastic properties, dynamic schemes such as the SPP are able to capture them. We use both MITlaos [53] framework (*static*) and SPP [47] interface (*dynamic*) to quantify the non-linear and transient viscoelastic properties of the PRP solutions.

The shear stress response can be described as a sum of higher harmonic contributions as [49, 53, 56]

$$\hat{\tau}(\hat{t}) = \sum_{n-\,odd} \hat{\tau}_n \sin(n\hat{\omega}\hat{t} + \delta_n) = \sum_{n-\,odd} \gamma_1 |\hat{G}_n| \sin(n\hat{\omega}\hat{t} + \delta_n), \tag{2.9}$$

where $\hat{G}_n$ and δ_n are the complex moduli and the phase angle respectively. Using the framework described by Ewoldt *et al.* [53], intra-and inter-cycle non-linearities, strain stiffening and/or softening, and shear-thinning and/or thickening behaviour can be quantified using the following set of variables: The minimum strain elastic shear modulus or tangent modulus at ($\gamma = 0$), $\hat{G}'_M$; and the large strain elastic shear modulus evaluated at the maximum imposed strain ($\gamma = \gamma_1$), $\hat{G}'_L$. According to Läuger *et al.* [56], this framework can be understood using the following parameters for a sinusoidal stress/strain input

$$\hat{G}'_M = \left.\frac{\mathrm{d}\hat{\tau}}{\mathrm{d}\gamma}\right|_{\gamma=0} = \sum_{n-\,odd} n\hat{G}'_n \tag{2.10}$$

and

$$\hat{G}'_L = \left.\frac{\hat{\tau}}{\gamma}\right|_{\gamma=\pm\gamma_1} = \sum_{n-\,odd} \hat{G}'_n(-1)^{(n-1)/2}. \tag{2.11}$$

These set of properties can be determined graphically using the Lissajous–Bowditch (LB) diagram plotting $\hat{\tau}$ as a function of γ and $\dot{\hat{\gamma}}$. The same can be quantified for viscous components using the Fourier parameters of the higher harmonic stress contributions. The minimum-rate and large-rate dynamic viscosities, $\hat{\eta}'_M$ and $\hat{\eta}'_L$, respectively, can be defined as following [56],

$$\hat{\eta}'_M = \left.\frac{\mathrm{d}\hat{\tau}}{\mathrm{d}\dot{\hat{\gamma}}}\right|_{\dot{\hat{\gamma}}=0} = \frac{1}{\hat{\omega}} \sum_{n-\,odd} n\hat{G}''_n(-1)^{(n-1)/2} \tag{2.12}$$

and

$$\hat{\eta}'_L = \left.\frac{\hat{\tau}}{\dot{\hat{\gamma}}}\right|_{\dot{\hat{\gamma}}=\pm\dot{\hat{\gamma}}_1} = \frac{1}{\hat{\omega}} \sum_{n-\,odd} \hat{G}''_n. \tag{2.13}$$

Based on these sets of variables, a strain-stiffening ratio is defined as [53]

$$S(\hat{\omega}, \gamma_1) = \frac{\hat{G}'_L - \hat{G}'_M}{\hat{G}'_L} \tag{2.14}$$

and the shear-thickening ratio

$$T(\hat{\omega}, \gamma_1) = \frac{\hat{\eta}'_L - \hat{\eta}'_M}{\hat{\eta}'_L}. \tag{2.15}$$

For cases when $S > 0$, the elastic behaviour of the material can be interpreted as intra-cycle strain-stiffening, whereas $S < 0$ indicates intra-cycle strain-softening. Also it is known that for a linear elastic response, $S = 0$. Similar to the elasic behaviour, the viscous counterpart, $T > 0$ corresponds to intra-cycle shear-thickening and $T < 0$ indicates intra-cycle shear-thinning. Also it is to be noted that, $T = 0$ corresponds to a linear viscous response [53].

In addition to the S and T parameters, to gain insight into the transient behaviour of the viscoelastic property of the PRP solutions, the stress response of the solution to an oscillatory strain can described using the SPP framework described by Rogers [47]. The SPP framework describes a dynamic trajectory in a two-dimensional space and is defined by the dynamic non-linear viscous response modulus, $\hat{G}''_t(\hat{t})$, and the dynamic non-linear elastic response modulus, $\hat{G}'_t(\hat{t})$, in a dynamic Cole–Cole plot as defined by Rogers [47]. These two time dependent moduli can be obtained by equating each of the terms in the brackets equal to zero in the following equation,

$$\left[\hat{G}'_t + \frac{\hat{B}_\gamma}{\hat{B}_{\hat{\sigma}}}\right]\gamma + \left[\hat{G}''_t + \frac{\hat{B}_{\hat{\dot{\gamma}}/\hat{\omega}}}{\hat{B}_{\hat{\sigma}}}\right]\frac{\hat{\dot{\gamma}}}{\hat{\omega}} = 0, \tag{2.16}$$

which defines the form of the non-linear response moduli needed to satisfy a full time-dependent description of an arbitrary oscillatory shear stress response which gives rise to the following moduli,

$$\hat{G}'_t(\hat{t}) = -\frac{\hat{B}_\gamma(\hat{t})}{\hat{B}_{\hat{\sigma}}(\hat{t})}, \tag{2.17}$$

and,

$$\hat{G}''_t(\hat{t}) = -\frac{\hat{B}_{\hat{\dot{\gamma}}/\hat{\omega}}(\hat{t})}{\hat{B}_{\hat{\sigma}}(\hat{t})}, \tag{2.18}$$

where $\hat{B}$ is the binormal vector, which is a differential parameter and both the moduli are not dependent on the total strain, but only changes in the strain. The temporal derivatives of the response moduli in Eq. 2.17 and Eq. 2.18 can be also defined (see Eq. 22 and Eq. 23 [47]). Evaluating the rate of change of the non-linear response moduli enables one to quantify for the amount of thickening/thinning and stiffening/softening, and also the crucial information of the instants when transitions occur [47].

3. Methods

3.1 Biological Techniques

The PRP samples in this study were formulated at the Sports Clinic of Baylor St. Lukes Medical Center, consistent with the standard procedure used in treatment of OA [34, 57–60]. The samples were prepared with a commercial product, the SmartPrep PC-30; Harvest Terumo BCT, a system used for producing autologous platelet concentrate enriched with growth factors. PRP is extracted from 30 mL of human WB (35 year old healthy male, with addition of 3 mL of the anticoagulant citrate dextrose solution). It is worth noting that Ethylenediaminetetraacetic acid (EDTA), especially K2-EDTA [61] is the commonly used anticoagulating agent. However, EDTA is known to cause platelet swelling and the mean platelet volume (MPV) values can possibly increase with its use [62]. In terms of platelet recovery, another anticoagulant agent, sodium citrate (SC) is reported to have the highest platelet recovery when compared to the other two [63], i.e., EDTA and citrate dextrose. A double-spin protocol is conducted in which an initial 1 to 3 minute spin at 2500 ± 150 RPM is followed by a secondary spin of 6 to 9 minutes at 2300 ± 150 RPM to yield a total PRP product of approximately 4 mL. More detailed procedure is given in Refs. [19, 20]. Sample preparation research protocols were approved by the Institutional Review Board (Baylor College of Medicine IRB H-42129). Five different PRP samples namely PRP1, PRP2, PRP3, PRP4, and PRP5, having varying cell counts in accordance to applicability for the therapeutic use, were chosen for the tests. Also, two more samples were characterized, namely Platelet Poor Plasma (PPP) and P3 (a solution obtained from diluting PRP3 with autologous PPP [64]).

The RBC, WBC, and platelet counts of the solutions, provided in in Appendix A.1,

are determined by scatter cytogram and platelet-integrated analysis, and compared to WB (ADVIA 120 Hematology Analyzer, Siemens). Based on the cell counts of the five samples, in terms of clinical terminology, PRP1, PRP2, and PRP3 are known as LP-PRP, although PRP3 has higher RBC count[1] as compared to an average LP-PRP [35]. Similarly, PRP4 and PRP5 can be considered as LR-PRP with lower RBC and WBC count [35]. In order to gain a better rheological understanding, bright-field microscopy was performed instantaneously after pipetting a drop of PRP3, P3, and PPP samples on a glass slide at room temperature of 23°C under live and stationary conditions (with no cover slip), using a Nikon Ti Inverted Research Microscope (Fig. 3.1). The erythrocytes can be seen in stack formations, i.e., rouleaux-type structures in Fig. 3.1a and b. Although, rheological tests were not performed for P3 and PPP solutions, the cell counts and volume fraction are reported in order to have a better interpretation of the microscopy images. Similarly, WB cell counts have been quantified for comparison purposes.

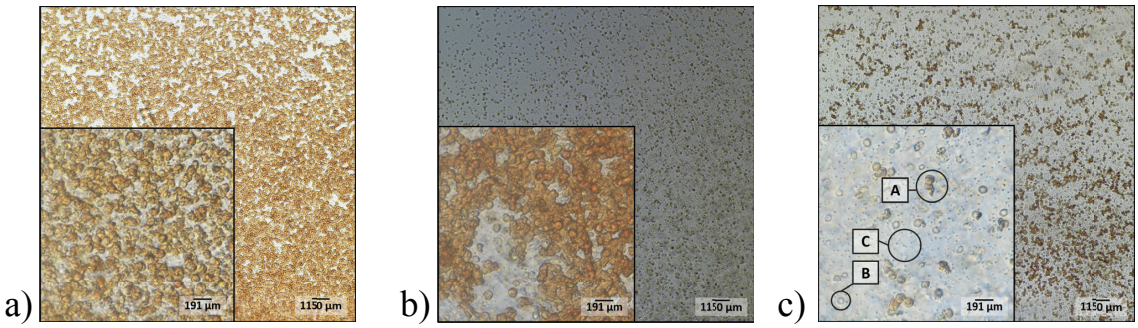

Figure 3.1: Bright-Field Microscopy Images of a) PRP3 , b) P3 (Diluted PRP3), and c) PPP solutions at 10x and 60x magnifications, with the latter presented as inset. In part c, leukocytes, erythrocytes, and platelets have been marked as A, B, and C respectively.

[1]RBC counts of our PRP samples are a bit higher than the average PRP reported in the literature [35, 36, 65].

3.2 Rheological Techniques

The rheological tests have been performed using the advanced Discovery Hybrid Rheometer (DHR3 from TA Instruments). The temperature is precisely controlled using a Peltier plate. All rheological measurements were collected via the TRIOS software provided by TA Instruments. "Correlation" sampling mode is used for data collection for all the tests, except for the LAOS tests which is performed using "transient" sampling mode. The rheology technique closely follows the procedure of Alves *et al.* [7] and Sousa *et al.* [8], which are carried out for human WB samples. Alves *et al.* have meticulously compared six various geometries (cone-and-plate at different cone angles and plate-and-plate at different gap heights) [7]. Based on the analysis and results shown in their paper, we have selected a 40-mm-diameter plate-and-plate/parallel-plate geometry (TA Instruments serial #: 107398) as an accurate tool for rheological characterization of the PRP samples. The gap of the geometry is set at relatively large value of 1000 μm which would diminish errors associated with settling of red blood cells compared to a close-gap geometry [4]. The Erythrocyte Sedimentation Rate (ESR) under quiescent conditions is known to be less than 30 mm/h ($\approx$ 8.3 μm/s) [66]. Such rate in the tests is presumed to be much less due to applying shear which causes flow agitation and suspension of blood components throughout the rheological characterization. Besides that, a 40-mm-diameter geometry is selected over 60-mm one to reduce the surface tension artifacts on measured torque [2]. Water viscosity was perfectly recovered using the chosen geometry for benchmarking purpose. A removable solvent trap case (without solvent) is additionally placed around the geometry to reduce sample evaporation (and thus under-fill) which is proven to result in significant errors [2]. All rheology experiments are intermittently filmed using Basler Ace high speed camera (acA2040-90um CMOS) to ensure proper sample fill throughout the duration of tests. All the rheological tests

were approved by UH protocol No. HPR-KA19.

3.2.1 Testing Procedure

Prior to carrying out the rheological tests and in order to ensure homogeneous PRP solutions, the samples are mixed at 50 rotations per minute (RPM) for five minutes at room temperature ($\hat{T} \approx$ 20°C). There can be slight evaporation of samples which is inevitable specially at higher temperatures even though a solvent trap case is placed around the samples. A minute amount of sample from the same agitated batch is therefore added before running each test to ensure proper fill.

A pre-shear conditioning step was added before each test to ensure re-suspending of any particulate matter which might have settled during the tests. Following the detailed procedure explained by Valant *et al.* [6], the pre-shear tasks include these steps: **i)** An initial steady shear was performed at 200 s^{-1} for 200 s; **ii)** then a steady shear is applied at 0.1 s^{-1} for 20 s; **iii)** finally a period of rest is provided for 20 s. Utilizing this method allows for instigation of turbulent mixing, followed by a period of reduced shear to slow the flow within the PRP samples and finally a period of break to allow the samples to come to rest before the test begins. For the LAOS tests, a pre-shear of 300 s^{-1} for 30 s was provided, instead of the routine pre-shear procedure, which is similar to the protocol of Sousa *et al.* [8] for WB.

Given the nature of the blood product samples, we follow the methodical protocol of Alves *et al.* [7] for both flow-sweep and frequency-sweep tests in the linear range. For LAOS, we strictly follow the procedure of Sousa *et al.* [8] for WB. All flow-sweep, frequency-sweep, and triangular ramp tests are performed at 25°C and 37°C to study the effect of temperature on samples rheology (room and physiological temperature). Additionally, LAOS and thixotropy experiments were evaluated at the physiological temperature. **i)**: The flow-sweeps are performed over a broad range of shear rate $\hat{\dot{\gamma}} \in [500 - 0.1]$ s^{-1}. Each sample is tested in a triplicate manner, following high-to-low, low-to-high, and high-to-low shear rate, $\hat{\dot{\gamma}}$, once more, to ensure reliable readings and

minimizing particle settling effects [7]. The objective of this category of tests is to characterize the apparent viscosity, $\hat{\eta}$, as a function of the shear rate, $\hat{\dot{\gamma}}$, evaluating possible non-Newtonian effects associated with PRP samples. **ii)**: It is known that the deformability and aggregation of erythrocytes in the presence of fibrinogens within blood or blood based products can cause *viscoelastic* behavior [8], which will be discussed for PRP solutions in detail in Section 4. Oscillatory tests have been carried out at both 30% and 20% strain (SAOS) to evaluate the linear viscoelastic response of samples through quantifying the elastic, $\hat{G}'$, and loss moduli, $\hat{G}''$ [7, 67]. LAOS tests are performed to measure the non-linear viscoelastic properties of PRP4. The tests are performed at 1000% strain and 0.251 rad/s [8]. In order to avoid material instability and *wall-slip*, only in LAOS tests we used a 40 mm diameter serrated plate–plate geometry, using a gap of 1000 μm, which is similar to the procedure of Sousa *et al.* [8]. For reference, the minimum gap between cartilage surfaces in a knee joint under load has been reported to be $\approx$ 0.1 μm in the literature [68], along with the walking and running frequencies of 4.39 and 18.85 rad/s respectively [40], as well as shear rate range of $\hat{\dot{\gamma}} \in [0.1 - 10^5]$ s^{-1} in a healthy knee [69]. **iii)**: Finally, for quantification of thixotropy, steady shear kinetics are also obtained at 10 s^{-1} and 20 s^{-1} to quantify any viscosity dependencies on time.

4. Results & Discussions

4.1 Flow-Sweep Tests

The dependency of the apparent viscosity, $\hat{\eta} = \hat{\tau}/\hat{\dot{\gamma}}$ (with $\hat{\tau}$ being the shear stress), on the shear rate, $\hat{\dot{\gamma}}$, for the PRP samples at 25°C is shown in Fig. 4.1. The triangular shaded areas in Fig. 4.1 and Fig. 4.2, follow equation (4.10) denoting the unreliable range of data due to the formation of secondary turbulent flows within the geometry [2]. Equation (4.8) for minimum viscosity measurable by the rheometer falls below all the data points shown here (no artifact). All the PRP samples exhibit non-Newtonian *shear-thinning* effect i.e. decrease in apparent viscosity with the shear rate [67, 70]. This effect is in line with the various other observations reported in the literature for WB [4–9, 71]. Such rheological behaviour for WB may be understood from the physiological ability of the red blood cells (erythrocytes) to deform under shear [5, 48, 72]. This deformability is reversible in nature due to the presence of fibrinogen [73–75], a soluble protein present in blood plasma. Immunoglobulins [76] and other acute proteins present in the plasma are also understood to influence this deformability but only in the presence of fibrinogen [77] (there is no available facility at Baylor College of Medicine's lab in our case to measure fibrinogen concentration in PRP samples). Moreover, at low shear rates, the erythrocytes get aggregated, which give rise to the formation of rouleaux [78]. Also, in order to understand and quantify the platelet interaction mechanisms within the PRP solutions, the von Willebrand factor (VWF) needs to be quantified, which plays a central role in primary haemostasis and mediates platelet adhesion and aggregation [79]. Further research is required with a bigger sample size to fully understand the relation between rheological behavior of PRP in terms of RBC-WBC-platelet interactions.

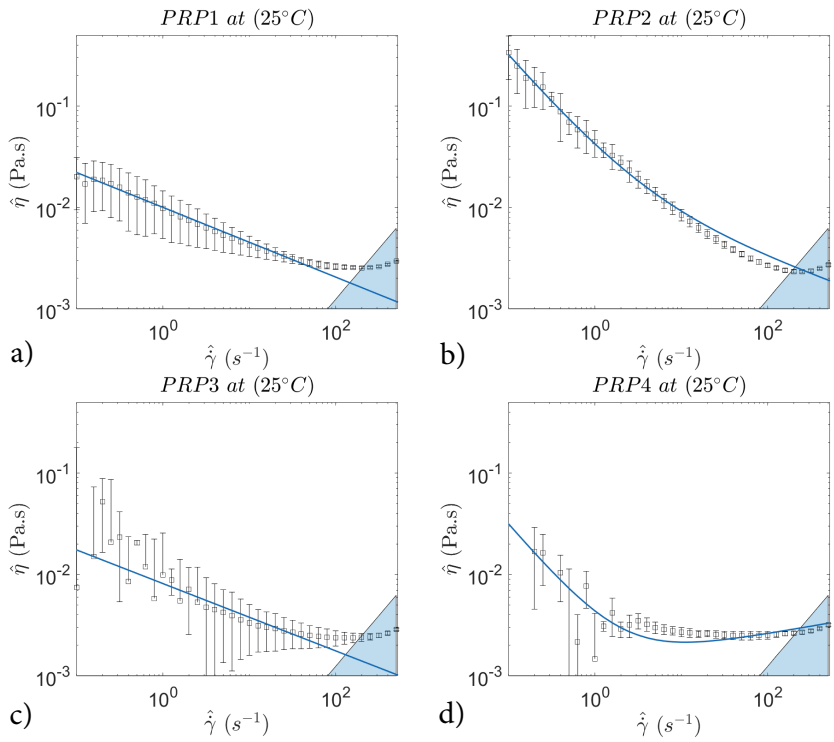

Figure 4.1: Dependency of the apparent viscosity, $\hat{\eta}$, on the shear rate, $\hat{\dot{\gamma}}$ for a) PRP1, b) PRP2, c) PRP3, d) PRP4 samples at 25°C along with the Herschel Bulkley (HB) fit presented as the continuous blue line.

4.1.1 Minimum Torque Limit

The shear stress at plate radius, $\hat{\tau}_{\hat{r}=\hat{R}}$, strain, γ, and strain rate, $\hat{\dot{\gamma}}$, as functions of torque, $\hat{T}$, angular displacement, θ, and angular velocity, $\hat{\omega}$, are given in [2] as

$$\hat{\tau}_{\hat{r}=\hat{R}} = F_\tau \hat{T}, \gamma = F_\gamma \theta, \hat{\dot{\gamma}} = F_\gamma \hat{\dot{\theta}} = \hat{R}\hat{\omega}/\hat{H}, \tag{4.1}$$

where $\hat{F}_\tau$ is a coefficient to be derived below, $F_\gamma = \hat{R}/\hat{H}$ with $\hat{H}$ being the gap height, and $\hat{r}$ and $\hat{R}$ are radial location and radius of parallel-plate geometry respectively. For parallel-plate geometry, the wall shear stress at radius, $\hat{r}$, is given as

$$\hat{\tau} = \hat{\mu}\frac{\hat{r}\hat{\omega}}{\hat{h}}. \tag{4.2}$$

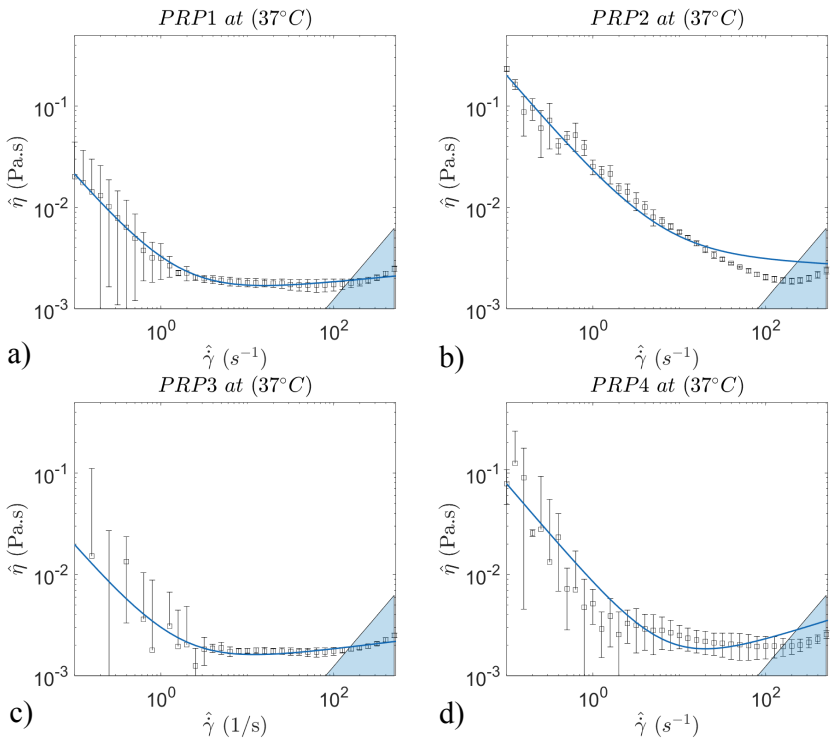

Figure 4.2: Same as Fig. 4.1 except at 37°C.

The total torque felt by rheometer as a result of shear stress imposed by the fluid can be obtained through the following integration

$$\hat{T} = \int_{\hat{A}} \hat{\tau}\hat{r}d\hat{A}, \tag{4.3}$$

where, $\mathrm{d}\hat{A} = 2\pi\hat{r}d\hat{r}$, is the differential area. It is not difficult to show that

$$\hat{T} = \hat{\mu}\frac{2\pi\hat{\omega}}{\hat{h}}\left(\frac{\hat{R}^4}{4}\right), \tag{4.4}$$

which can be also written as

$$\hat{T} = 2\pi\hat{\tau}_{\hat{r}=\hat{R}}\left(\frac{\hat{R}^3}{4}\right). \tag{4.5}$$

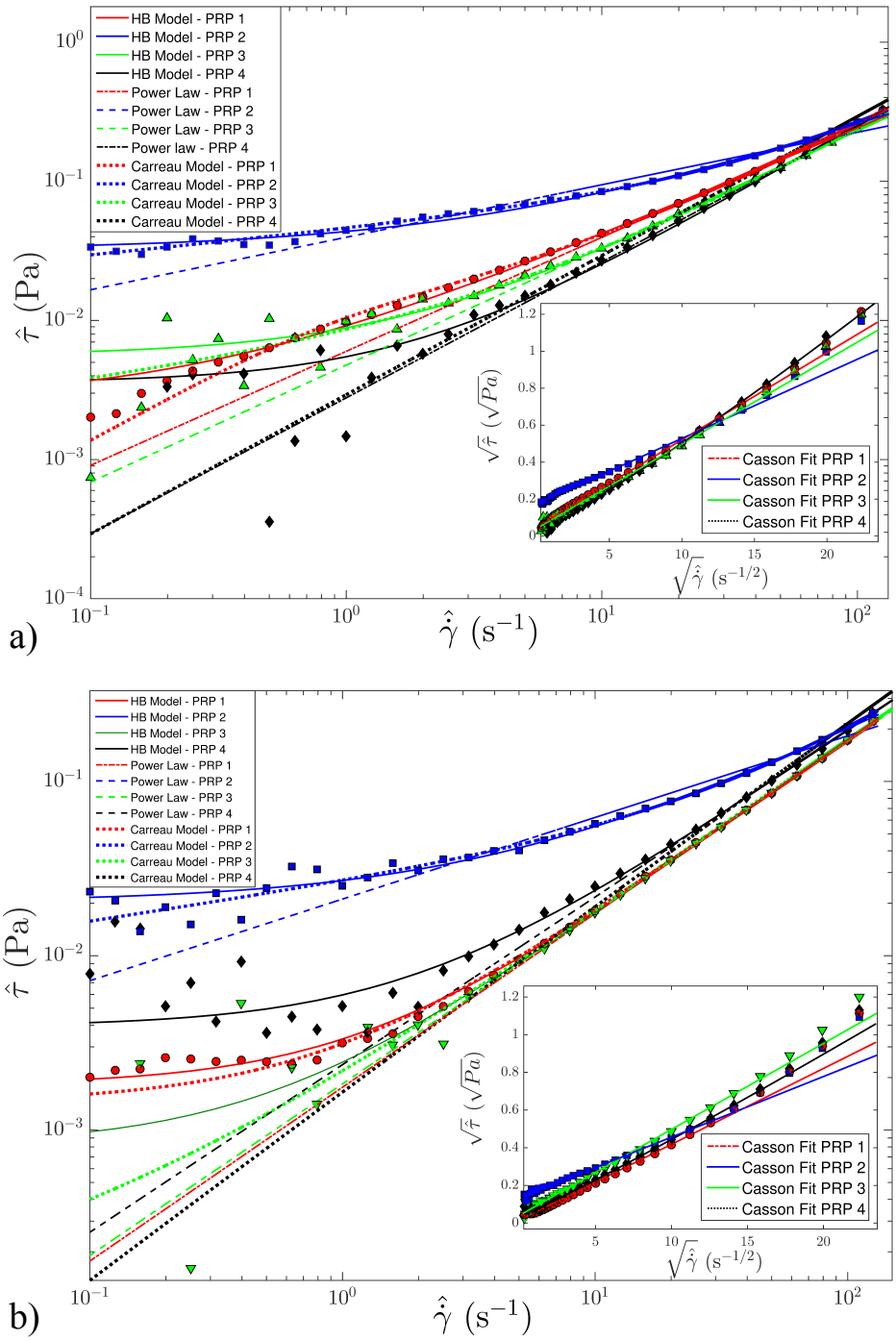

Figure 4.3: Dependency of the shear stress, $\hat{\tau}$, on the shear rate, $\dot{\hat{\gamma}}$, for PRP1 (red), PRP2 (blue), PRP3 (green), and PRP4 (black) samples at a) 25°C and b) 37°C are shown using the scatter plots. The Herschel-Bulkley (HB), power-law, Carreau model and Casson model (inset) fits are also displayed at both temperatures.

Solving for , $\hat{\tau}_{\hat{r}=\hat{R}}$, gives

$$\hat{\tau}_{\hat{r}=\hat{R}} = \frac{2}{\pi \hat{r}^3}\hat{T}. \tag{4.6}$$

Upon comparison with Eq. (4.1), $\hat{F}_\tau$ will be obtained as

$$F_\tau = \frac{2}{\pi \hat{R}^3}. \tag{4.7}$$

According to [2], the minimum apparent viscosity measurable by the machine is

$$\hat{\eta}_{\min} > \frac{F_\tau \hat{T}_{\min}}{\dot{\hat{\gamma}}}, \tag{4.8}$$

where $\hat{T}_{\min}$ is the minimum measurable torque by the rheometer which, in this case, is $\hat{T}_{\min} = 5 \times 10^{-9}$ N.m. In Fig. 4.1, we have confirmed that all the data points locate above the threshold defined in Eq. (4.8), confirming the reliability of the measurements. Ewoldt *et al.* [2] discuss that due to surface tension effects at low shear rates, the actual minimum measurable viscosity is often above the limit set in Eq. (4.8). The relatively larger error bars in Fig. 4.1 at lower share rate values confirm this fact. As shear rate is increased beyond $\dot{\hat{\gamma}} \approx$ 1 s^{-1}, surface tension artifact is decreased which is reflected in overall smaller error bars in Fig. 4.1.

4.1.2 Secondary Flow Limit

After addressing the rheology limitation at low range of shear rate, $\dot{\hat{\gamma}}$, it is time to discuss what precautions need to be taken at high shear rate values. The ratio of the measured torque, $\hat{T}$, to the ideal torque, $\hat{T}_0$, due to shear flow alone in parallel-plate geometry is given as [2]

$$\frac{\hat{T}}{\hat{T}_0} = 1 + \frac{3}{4900}Re^2, \tag{4.9}$$

where $Re = \hat{\rho}\hat{\omega}\hat{H}^2/\hat{\eta}_0$ is the Reynolds number, $\hat{\rho}$ is the sample density, and $\hat{\eta}_{ideal}$ is the ideal apparent viscosity due to sole shear flow. A 1% error in torque measurement results in $\hat{T}/\hat{T}_0 \approx$ 1.01 which according to Eq. (4.9) gives the critical Reynolds number,

$Re_{crit} \approx 4$, which is above turbulent transition Re [80]. Therefore, the maximum reliable apparent viscosity that can be measured by rheometer without introducing secondary turbulent flow artifacts is

$$\hat{\eta} > \frac{\hat{\rho}\hat{H}^3}{\hat{R}Re_{crit}}\dot{\hat{\gamma}}. \tag{4.10}$$

This line is plotted in Fig. 4.1 for PRP1-4. Interestingly, the line coincides to shear rate threshold above which the apparent viscosity begins to increase ($\dot{\hat{\gamma}} \approx 150\ \mathrm{s}^{-1}$). Without realizing the secondary flow limitation of rheometer, one could have falsely interpreted this behavior as *shear-thickening*.

In order to understand the effect of core body temperature on rheological properties of PRP samples, the flow-sweep measurements at 37°C are shown in Fig. 4.2. Similar to Fig. 4.1, PRP2 exhibits the highest viscosity. Moreover, upon comparing Figs. 4.1 and 4.2, a slight decrease of viscosity with temperature is observed which is common in liquids (reduced cohesive molecular force) [81, 82]. The minimum torque and secondary flow limits are further checked for high-temperature rheological measurements. All the data points fall beyond the minimum viscosity predicted by Eq. (4.8). At low shear rate values, overall larger error in $\hat{\eta}$ is observed due to surface tension effects. The error bars at 37°C (Fig. 4.2) seem to be larger than those at 25°C (Fig. 4.1) indicating the sensitivity of measurements at higher temperature. This effect, which is observed in similar work in the literature, can possibly be associated with natural convection effects [83]. There are various ranges of the apparent viscosity, $\hat{\eta}$, reported in the literature regarding blood rheology [5, 7], which are approximately comparable to the results shown in Fig. 4.2. Factors such as age [84] and hematocrit [5] are amongst the most important ones. Finally, the onset of turbulence and secondary flow in Fig. 4.2 is accurately predicted by Eq. (4.10). Additionally, the fitting results of the four rheological models discussed in Appendix 2.1 are shown for both the temperatures

in Fig. 4.3. Based on the Carreau model, PRP1, PRP2, and PRP3 show similar $\hat{\eta}_\infty$, especially at 37°C, but $\hat{\eta}_0$ differs considerably (see Table A.6). Overall, based on the R^2 values in Table A.5, the HB model is predicts the rheological behaviour most accurately as compared to the other three models. In these experiments, both from Casson and HB model values of $\hat{\tau}_0$ given in Tables A.4 and A.5 respectively, we find that PRP2 overall possesses the highest yield stress among other samples [85, 86]. Additional investigations are required to understand whether the observed rheological behavior is due to classical suspension mechanics-type interactions of RBC, WBC, and platelet or simply due to sample to sample variations in biological systems. Except a few scattered data points in HB model that predict minute shear-thickening (PRP4 at 25°C and PRP1 and PRP3 at 37°C), almost all other data as in power-law, HB, and Carreau predict $n < 1$ i.e. shear-thinning behavior. Among all the rheological models used, HB shows the highest R^2 value across all PRP solutions, suggesting the effectiveness of such fit.

4.2 SAOS Tests

Following the methodology of Alves *et al.* [7] and in order to characterize the linear *viscoelastic* properties of PRP samples, frequency-sweep test results have been described here. In WB, the deformability of the erythrocytes and its aggregates (rouleaux) under shear and oscillatory forces, leads to a cyclic process of storage and release of elastic energy resulting in viscoelastic property [4–9]. Furthermore, in a recent study of Brust *et al.* [87], it is revealed that plasma exhibits viscoelastic properties as well, however, only under extensional flow conditions with a relaxation time of 0.5 ms at 37°C. Under pure shear flow conditions, plasma exhibits non-viscoelastic Newtonian behavior [72]. Similar to flow-sweep test, the rheological measurements in frequency-sweep case are not immune to artifacts and need to be interpreted very carefully. As elegantly described by Ewoldt *et al.* [2], there are three major sources

of error namely *minimum torque*, *instrument inertia*, and *sample-inertia* that may impact frequency-sweep measurements. These limits are discussed in the following sections in detail.

4.2.1 Minimum Torque Limit

Following a similar approach as shown in Section 4.1.1, it is not difficult to derive the minimum torque limit given below for modulus, $\hat{G}$ (being either $\hat{G}'$ or $\hat{G}''$) [2]

$$\hat{G}_{\min} = \frac{F_\tau \hat{T}_{\min}}{\gamma_0}, \tag{4.11}$$

where in this case, strain, $\gamma_0 = 0.3$, corresponding to 0.015 rad as per $\theta = 2\gamma\hat{H}/\hat{D}$. The horizontal line associated with minimum measurable modulus is added to Fig. 4.4.

4.2.2 Instrument-Inertia Effect

Instrument inertia is present in tests under transient conditions, such as found in the frequency sweep [2]. This inertial effect is caused by the unsteady motion present in the rheological testing apparatus, where the geometry is required to accelerate in opposite directions rapidly, introducing an additional load torque to the measurement. In order to have reliable data, the torque caused by material should exceed that of instrument i.e.

$$\hat{T}_{Material} > \hat{T}_{Instrument}, \tag{4.12}$$

or

$$\frac{\hat{G}\gamma}{F_\tau} > \hat{I}\hat{\alpha}, \tag{4.13}$$

where $\hat{\alpha} = \dot{\hat{\omega}} = \ddot{\theta}$ and $\hat{I}$ is the combined inertia of the machine and the geometry which in this case is $\hat{I} \approx \ 2.94478 \times 10^{-5}$ Nms^2. For sinusoidal loading in the form of $\theta(t) = \theta_0 \sin\left(\hat{\omega}\hat{t}\right)$, one may obtain $\hat{\alpha} = \theta_0\hat{\omega}^2$. Therefore,

$$\hat{G} > \hat{I}\frac{F_\tau\theta_0}{\gamma_0}\hat{\omega}^2. \tag{4.14}$$

Using Eqs. (4.1) and (4.7), Eq. (4.14) can be re-written as

$$\hat{G} > \frac{2\hat{I}\hat{H}}{\pi\hat{R}^4}\hat{\omega}^2. \tag{4.15}$$

The $\hat{G}$ values (either $\hat{G}'$ or $\hat{G}''$) that locate above/below the line indicated by Eq. (4.15) are valid/invalid. The hallmark of instrument-inertia in rheological tests is slope of modulus, $\hat{G}$, being 2 in log-log scale [2]. The instrument-inertia limit is indicated in Fig. 4.4. The crossover of $\hat{G}'$ and $\hat{G}''$ for PRP1 and PRP2 solutions appears to occur at a frequency corresponding to instrument-inertia limit. One may also note that $\hat{G}'$ values after instrument-inertia point follow a line with slope 2 plotted in logarithmic scale in all PRP samples [2].

4.2.3 Sample-Inertia Effect

Similar to the instrument-inertia effect, once the oscillation frequency reaches a certain level, sample inertia develops wave propagation issues [2]. For reliable rheological measurements, the wavelength of the propagating wave, $\hat{\lambda}_{wave}$, should be much larger than the geometry gap, $\hat{H}$. Following a detailed linear viscoelastic wave propagation analysis, one may arrive at the following condition for sample-inertia limit [2, 88]

$$\left|\hat{G}^*\right| > \left(\frac{10}{2\pi}\right)^2 \cos^2(\delta/2)\hat{\rho}\hat{\omega}^2\hat{H}^2, \tag{4.16}$$

where $\delta = \tan^{-1}\left(\hat{G}''/\hat{G}'\right)$ is the viscoelastic phase angle and $\left|\hat{G}^*\right| = \sqrt{\hat{G}'^2 + \hat{G}''^2}$ is the magnitude of the complex modulus. In order to determine the applicable range of frequency-sweep data, the sample-inertia limits are added to Fig. 4.4. As can be seen, the sample-inertia line is located on the right hand side of the instrument-inertia one meaning that, in this case, high-frequency artifacts may first become significant due to instrument inertia. It is hoped that in future, and for preciseness and transparency, all the researchers present their rheological measurements in presence of limitations and conditions such as minimum torque, instrument inertia, and sample-inertia [2].

The small amplitude oscillatory tests in this case have been carried out at 30% strain over a wide range of frequency, $\hat{\omega} \in [10^{-1}, 10^{2}]$ rad/s, at both 25°C (Fig. 4.4) and 37°C (Fig. 4.5). The most important information to be extracted from oscillatory tests are storage, $\hat{G}'$, and loss moduli, $\hat{G}''$ representing the degree of solid and liquid-like behavior of samples respectively. The acceptable range of data will be described below. Due to the instrument limitations and the small elastic nature of blood [8], a narrow window of data was retrievable from the SAOS tests as shown in Figs. 4.4 and 4.5. PRP1 and PRP2 exhibit loss modulus, $\hat{G}''$, slightly larger than the storage modulus, $\hat{G}'$, i.e., stronger fluid-like as opposed to solid-like response. This trend is roughly reported for WB samples as well [7]. PRP4, however, shows stronger elastic response at low-shear-rate regions. No presentable data were measured for PRP3, as they were affected by surface tension effects.

The frequency-sweep tests at core body temperature, $\hat{T} = 37$°C are presented in Fig. 4.5 with moduli values in comparable range as to those reported by Alves *et al.* [7] for WB. The experimental limits have been represented by inclined solid line, dashed line, and horizontal dotted line indicate sample-inertia limit, Eq. (4.16), instrument-inertia limit, Eq. (4.15), and minimum torque limit, Eq. (4.11), respectively. Most of the effects shown in Fig. 4.5 are consistent with those depicted in Fig. 4.4 for $\hat{T} = 25$°C, except at higher temperature, both the elastic and loss moduli are slightly decreased. In addition to the 30% strain test, we have also carried out frequency-sweep tests at 20% strain for both $\hat{T} = 25$°C and 37°C (results not shown here for brevity). The trends observed were mostly similar to 30% strain.

4.3 LAOS Tests

Similar to the studies performed by Sousa *et al.* [8], LAOS tests are conducted to investigate the non-linear viscoelastic regime of the PRP solutions in this study. Moreover, as pointed out by Sousa *et al.* [8], the SAOS tests are not suggested for

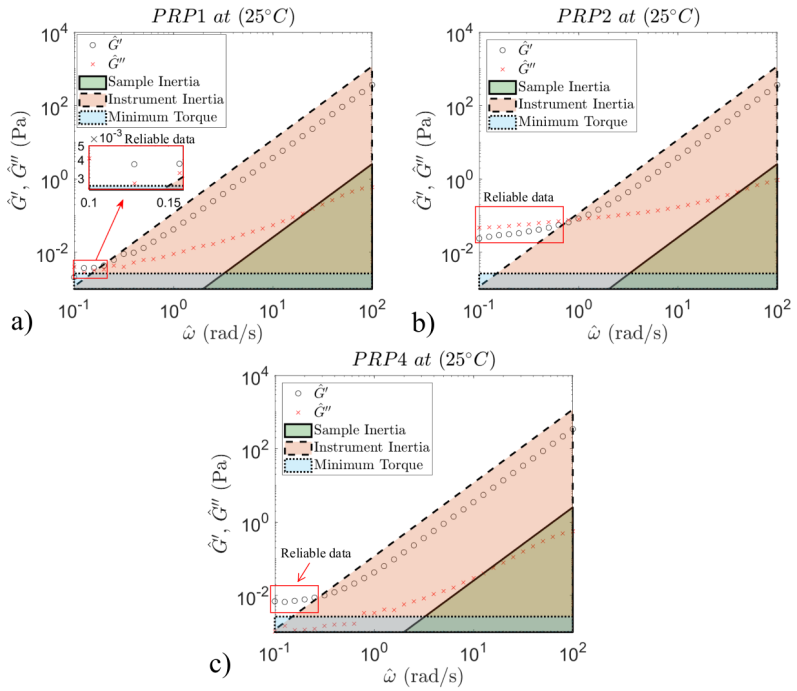

Figure 4.4: Dependency of the storage, $\hat{G}'$, and loss moduli, $\hat{G}''$, on frequency, $\hat{\omega}$, at 25°C and 30% strain. The data within the shaded regions are unreliable.

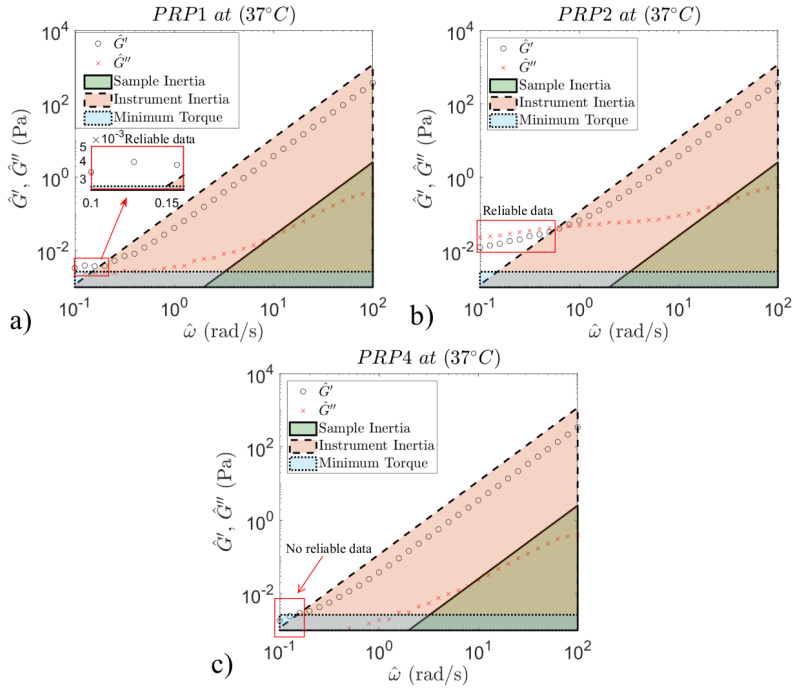

Figure 4.5: Similar to Fig. 4.4 except carried at 37°C.

viscoelastic measurements for WB. This is also seen in our case as the measurement window for SAOS is rather narrow. Prior to PRP testing, numerous benchmarking experiments were conducted. In particular, we fully recovered the results of Hyun *et al.* [49] for 4% Xanthan gum aqueous solution at strain amplitude of 10 s^{-1} and frequency of 1 rad/s using MITlaos software [25]. Note that we found LAOS results for fluids with very low viscosity such as water to be affected by surface tension artifacts. For the actual PRP solutions, we follow the experimental protocol of Sousa *et al.* [8]. The imposed strain follows a sinusoidal transient wave, $\gamma(\hat{t}) = \gamma_1 \sin(\hat{\omega}\hat{t})$, where $\hat{t}$ is the time in seconds and γ_1 is the maximum strain amplitude of the cycle. The corresponding shear stress response is measured by the rheometer which is not necessarily a sinusoidal function for a given complex fluid [26]. The imposed sinusoidal strain function as well as shear stress response are depicted in Figs. 4.6a and b respectively for PRP4 sample over five cycles. Values of $\gamma = 1000\%$ and $\hat{\omega} = 0.251$ rad/s are chosen to be consistent with study of Sousa *et al.* [8] for WB (approximate duration of 20 mins per test).

Figures 4.6c, d and e, f, demonstrate the raw data (total stress versus strain and strain rate respectively) averaged over 15 cycles during LAOS tests for PRP4 and PRP5 solutions. In addition to the total stresses, the third and fifteenth harmonics ($n = 3$ and 15) stress responses calculated using MITlaos framework are added as inset. The elastic and viscous parameters are evaluated at default $n = 15^{th}$ harmonic for PRP4 and PRP5 using the MITlaos and are represented in Table 4.1. Both the dimensionless indices indicate the two mixtures to be intra-cycle strain-softening and shear-thinning, i.e., $S < 0$ and $T < 0$ respectively. Note that the absolute values of S and T for PRP4 using $n = 3$ harmonic instead of 15 shows a decrease of 1.3% and 36.4% respectively but their signs remain unchanged; see the inset of Fig. 4.6c and d. It is interesting to note that, it has been reported by Shah and Janmey [89], that the addition of platelets to human plasma increases its stiffness. Moreover, they go

Table 4.1: Calculated elastic moduli ($\hat{G'}_M$ and $\hat{G'}_L$), dynamic viscosities, ($\hat{\eta}'_M$ and $\hat{\eta}'_L$), strain-stiffening ratio, S, and shear-thickening ratio, T, for PRP4. Evaluations are performed for γ_1=1000%, at $\hat{\omega}$=0.251 rad/s using MITlaos software.

	$\hat{G'}_M$ (Pa)	$\hat{G'}_L$ (Pa)	S
PRP4	5.37×10^{-3}	1.88×10^{-3}	-1.847
PRP5	3.415×10^{-3}	2.714×10^{-3}	-0.258
	$\hat{\eta}'_M$ (Pa.s)	$\hat{\eta}'_L$ (Pa.s)	T
PRP4	3.34×10^{-3}	2.27×10^{-3}	-0.211
PRP5	1.183×10^{-2}	7.1×10^{-3}	-0.666

on to describe strain-stiffening behaviour of PRP from their strain amplitude sweep tests ($\gamma < 100\%$). Althouh, in our case the two PRP solutions in our study show strain-softening behaviour in the non-linear regime.

Additionally, tests have been conducted at γ_1=1000% and $\hat{\omega}$=0.158 rad/s finding similar intra-cycle strain-softening behavior as to Fig. 4.6, however, affected more by surface tension effect (results not shown for brevity). Besides, the results for γ_1=5000% at $\hat{\omega}$=0.158 rad/s and $\hat{\omega}$=0.251 rad/s, showed intra-cycle strain-stiffening behaviour, which are not presented for similar surface-tension-generated errors. For the given range of strain amplitudes and frequencies, Sousa *et al.* [8] reported strain-stiffening and shear-thinning behavior for whole blood. Further investigation, perhaps over a broader range of sample types, strain amplitude, and frequency, is required to fully understand intra/inter-cycle behavior of PRP solutions.

The transient moduli in Eq. 2.17 and Eq. 2.18, and its derivatives are evaluated for PRP4 and PRP5 for over 20 cycles using the SPP framework and are presented in Fig. 4.7. It can be observed in the Cole-cole plot of PRP4, Fig. 4.7a, that the solution goes through intra-cycle thinning and stiffening (square to triangle), then onto thickening with almost negligible softening (triangle to asterisk) and finally thinning

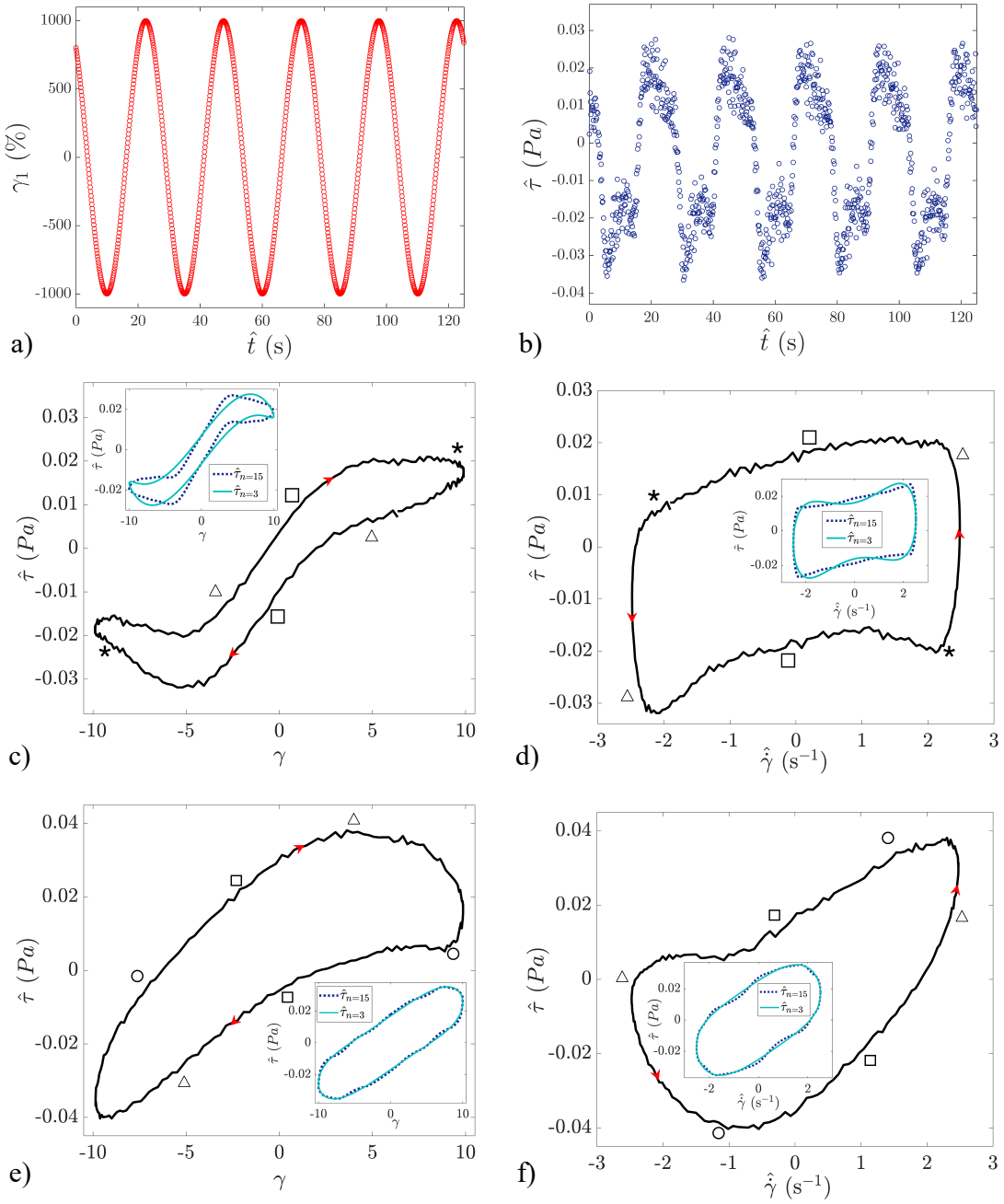

Figure 4.6: a) LAOS evaluations at 37°C with the applied strain, a and b, corresponding stress response. LB plots of total stress, c and d, for PRP4, and e and f, for PRP5. Symbols are from the SPP [54, 55] analysis.

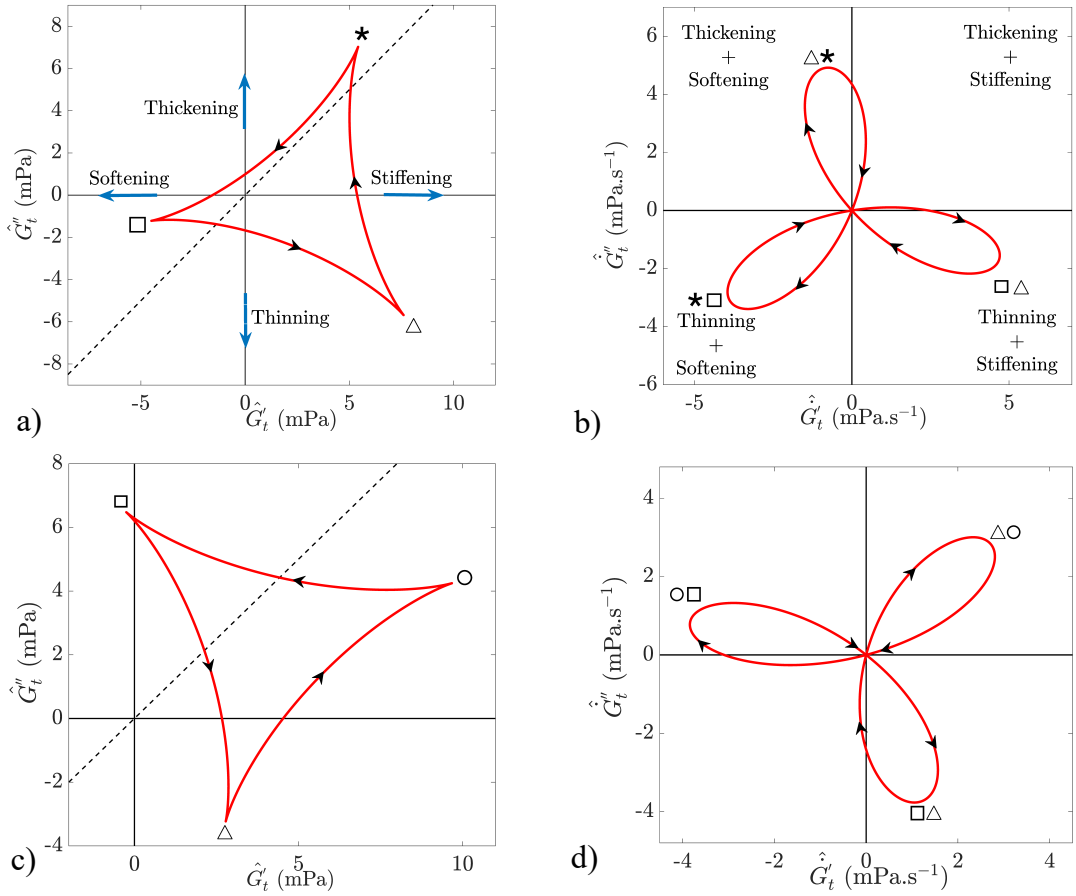

Figure 4.7: Transient evaluations of PRP4 and PRP5 using the SPP [54, 55] framework are shown in a, b and c, d, respectively. The plotted figures in b and d represent derivatives of the transient moduli.

and softening (asterisk to square). In a similar way, the transient bheaviour of the elastic and viscous moduli can be observed for PRP5 in Fig. 4.7c, initially the solution goes through intra-cycle thickening and stiffening (triangle to circle), then minute thickening occurs with softening (circle to square) and finally undergoing thinning and negligible stiffening (square to triangle). It is important to note that the dashed lines in Figs. 4.7a and c, represent, $\hat{G}''_t = \hat{G}'_t$, and along the horizontal and vertical lines, the linear viscous and elastic moduli are constant respectively.

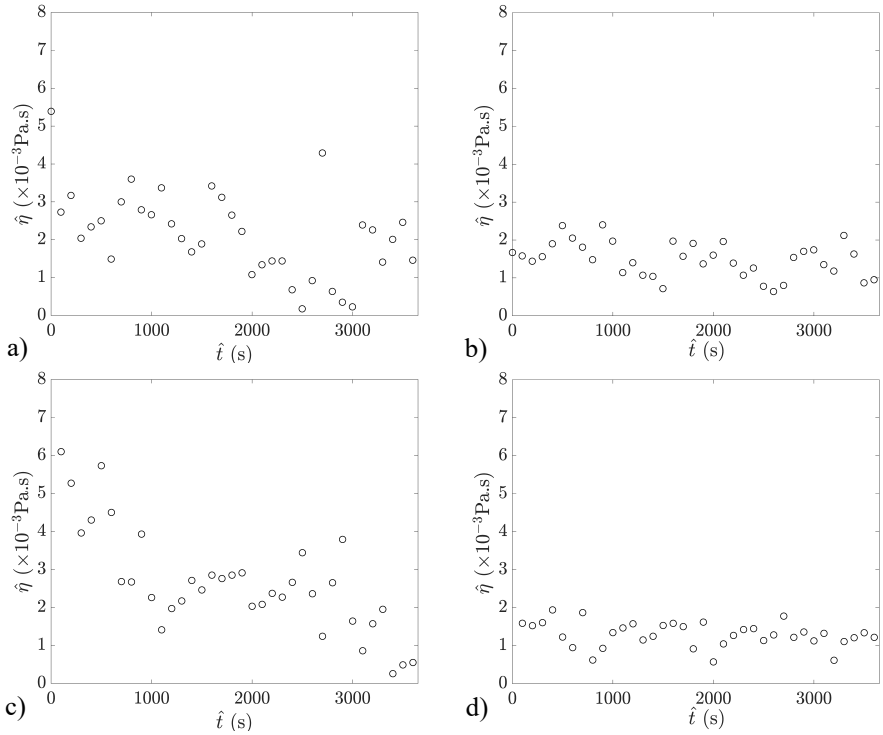

Figure 4.8: Thixotropic steady-shear kinetics measured at $\dot{\hat{\gamma}} = 10$ s^{-1} and $\dot{\hat{\gamma}} = 20$ s^{-1} for PRP4 and PRP5 solution, shown in a, b and c, d, respectively at a temperature of 37°C.

4.4 Thixotropy Tests

Following the procedure of Alves *et al.*[7] for WB, peak-hold experiments are carried out, at $\dot{\hat{\gamma}}$=10 s^{-1} and $\dot{\hat{\gamma}}$=20 s^{-1} to quantify any viscosity dependency on time. Both the tests, shown in Figs. 4.8a and b respectively, reveal a decrease in the viscosity over time for PRP4 and PRP5 samples at 37°C. As described by Alves *et al.*., such pronounced phenomenon for WB can be explained by the RBC aggregation process at low shear rates. The observations are comparable to the results presented by Alves *et al.* at respective shear rates. For both the samples at $\dot{\hat{\gamma}}$=10 s^{-1}, the decrease in $\hat{\eta}(\hat{t})$ is $\approx$ 60% and for $\dot{\hat{\gamma}}$=20 s^{-1}, the decrease is about $\approx$ 30% over a period of 60 mins.

In addition to thixotropic tests, hysteresis tests were carried out using a triangular ramp based on Bureau *et al.* [30]; see also recent studies of Apostolidis *et al.* [13]

and Armstrong *et al.* [14]. However, given the low range of shear rates in such test and possible contribution of surface tension artifacts, the results are not presented. Further investigation is required to fully understand the hysteresis behaviour of PRP solutions.

5. Conclusions

Platelet-rich plasma (PRP) has recently received increased attention due to its great potential for use in treatment of various injuries such as in sprained knee, post-traumatic osteoarthritis, and tendon as well as a remedy for arthritis. Rheological characterization of PRP thus becomes important. Following shear rheology namely, flow sweep, Small Amplitude Oscillatory Shear (SAOS), Large Amplitude Oscillatory Shear (LAOS), and thixotropy tests, we have characterized the apparent viscosity and elasticity of five different PRP mixtures with varying cell counts within the standards of therapeutic applications. The PRP solutions show non-newtonian effects such as shear-thinning, yield stress, and linear and non-linear viscoelasticity. All flow-sweep and SAOS tests are performed at 25°C as well as 37°C, apart from the LAOS and thixotropic tests which are performed only at 37°C. PRP samples exhibit shear-thinning behavior with higher apparent viscosity observed at lower temperature. Carreau, power-law, Casson, and HB models are fitted to the measured data with the latter exhibiting the closest fit.

It is also noticed that SAOS tests are found to have limited capability in quantifying the linear viscoelasticity of the PRP solutions as most of the complex viscous and elastic moduli data fall outside the reliable range of rheological measurement. Although, over the acceptable range of angular velocity, the loss modulus appears to dominate the storage modulus (except for PRP4 at 25°C) with both moduli decreasing at higher temperature. LAOS tests are also performed evaluating the non-linear and transient viscoelastic properties. The "static" analysis concluded shear-thinning and strain-softening behaviour for the two PRP samples tested. Additionally, "dynamic" analysis results are used to quantify the transient characteristics of the non-linear viscoelastic behaviour with the SPP metrics. Finally peak-hold tests at $\hat{\dot{\gamma}}$=10 s^{-1} and 20 s^{-1}

for 60 mins are performed revealing thixotropy. Moreover, this being a pilot study, a more comprehensive investigation is required to account for the various biological factors, i.e., sample-to-sample variations, fibrinogen content in plasma, VWF, inter-cell interactions, and rheological parameters, i.e., parallel-plate geometry gap, geometries, varying oscillatory amplitudes to quantify for non-linear and transient behaviour.

Part II

Numerical Investigation of Flow-Induced Vibration

6. Introduction

6.1 Motivation

Since the emergence of the oil and gas industries, techniques have been developed to control the flow, and choke-valves are an integral part of the extraction process [90]. The integrity and reliability while designing a subsea flow system is of prime importance. As the choke-valve needs to operate at a large variety of conditions, innate to the many processes, the evaluation of the integrity of such valve, therefore, its design is complex. The use of subsea wellhead choke-valves (WCV) is very common for controlling the flow of fluids from reservoirs. Most of the times, the operating conditions create large pressure drops across such choke valves which can give rise to adverse flow conditions. Such a flow can give rise to flow fluctuations and therefore large dynamic forces acting on these valves [91]. This can give rise to valve vibrations, noise and eventual failure of the valve in worst cases.

The two major phenomena that originate from the fluid flow within the valve which can cause failure are flow-induced vibration (FIV) [91–97] and acoustic-induced vibration (AIV) [98]. Although, AIV being a more commonly observed phenomenon in piping systems [99–102]. Both phenomena can cause fatigue, i.e., weakening of the material caused by a repetitive motion that results in cracks and eventual failure. AIV and FIV have been well-known in the industry since the 1970s, but lacked a clear and delineated understanding of the two. Until very recently, in 2018, Jaouhari *et al.*. [103] pointed out the differences and provided with a better understanding of the two types of vibrations, their sources, and their effects on piping systems. FIV has not received the same level of attention as compared to AIV for subsea choke valves. The major mechanism causing FIV is the vortex shedding phenomenon within turbulent flows.

Thereby, FIV can be referred to as vortex-induced vibration (VIV) under certain conditions. Such conditions are described by Blevins [94] in a comprehensive study reviewing VIV mechanism causing FIV. Blevins goes onto show the various analytical tools that can be used to analyze and investigate vibrations of a structure exposed to turbulent fluid flow. Apart from VIV, the other types of vibrations that can be induced by turbulent flows are galloping vibrations, stall flutter and vibrations induced by an oscillating flow [94, 104].

The flows within choke-valves are turbulent in nature because of the high fluid, i.e, gas or oil, production rates. Turbulence, which is known to be a broadband in nature [105], the oscillatory behaviour within the flow needs to be evaluated. Since, the highly-compressible nature of the flow in such choke valves, the flow oscillations generated can be of high pressure amplitudes. Such high-pressure oscillations will make the flow highly oscillatory. Consequently inducing higher-cyclic stresses within the valve structure over time. Hence, it becomes important to visualize the frequency spectrum of such fluid flow within such choke-valves. This will facilitate the investigation of the existence of dominant oscillatory modes within the flow. A similar comprehensive analysis has been performed by Ligterink *et al.* [106] for subsea production systems with a stress on the piping assembly. Additionally, an eigenmode analysis is performed to quantify the stress levels generated within the structure from each vibration mode. Even though such studies exist in the literature, they confine their investigation of the FIV to flow around bodies, piping systems, steam control valves. Despite the common occurance of FIV phenomenon in subsea-choke modules, it is fairly undetermined in multiple choke-valves within subsea gas production systems. Moreover, Dominick *et al.* [107] go onto show that the sensitivity of FIV with respect to geometrical design of steam control valves has been described. Such an pre-design analysis based approach can help in avoiding catastrophic consequences during gas production. Furthermore, according to the literature, the typical flow pattern within such a choke/control-valve

is transonic in nature and jet separation takes place. The flow fluctuations occur accompanied by large pressure oscillations [91, 96, 108, 109]. It was reported by Widel *et al.* [110] that such an unsteady flow excites the acoustic resonance in the valve, which results in failure and is a major thrust behind this study.

6.2 Thesis Statement

The purpose of this part of the thesis is to investigate FIV and associated dominant frequencies due to choking the flow of natural gas within a Diver Retrievable Subsea Choke Valve (P5E) from Master Flo Valve (USA) Inc. This will be conducted by performing computational fluid dynamics (CFD) computations of the natural gas flow within the valve, using STAR-CCM+ v.2019.2.1 (Build 14.04.013, win64/intel18.3vc14-r8 Double Precision) software from SIEMENS.

6.2.1 Project Specification

This main objective of this project is to analyze the gas flow within the choke valve at a critical choke position. To gain insight into the FIV generated due to this flow at a critical choke, the pressure fluctuations are probed at the walls inside the valve-nozzle (see Fig. 6.1). Finally to evaluate the dominant modes of vibrations being generated from the transient pressure oscillations, spectral analysis is performed using fast-Fourier transform (FFT). The Mach numbers have been investigated in order to identify the supersonic flow and choking, which is expected to occur due to the applied downstream to upstream pressure ratio. Additionally, temperature contours are also visualized to examine for highly underexpanded jet formation and temperature drops because of Joule-Thompson effect at the smaller ports of the nozzle.

The abovementioned quantities have been calculated at 32% of the full valve capacity, which is critical for subsea operation, e.g., Master Flo Valve (USA) Inc. reported field failures happening at this position. This choking condition of 32% is also the most commonly used choke level used during operation. This thesis is

mostly based on the computational analysis at this critical choking condition, which is performed on a simplified geometry of the P5E valve, keeping the flow domain the same as the original P5E model. This is done to reduce computational effort during mesh generation. The computations performed at 32% of the choke, has been modelled using real gas. For validation and benchmarking purposes, traditional test cases have been carried out. To make sure the compressible effects are fully captured with the code, a transonic flow is validated using the Sajben Transonic Diffuser and is described in Appendix B.1.1. In addition to that, flow over a cylinder is also simulated to validate the physics of vortex shedding effect can be fully captured with our code and is shown in Appendix B.1.3. In Appendix B.1.2 an inclined airfoil case is shown through which we want to see if we are able to fully capture the shock waves in the case of a compressible flow simulation. Additionally, the comparison with the study performed by Yonezawal *et al.*is conducted to check if the complex flow and FIV dominant frequency within a control valve of similar degree of complexity can be successfully recovered (see Appendix B.1.4). All the computations have been carried out using STAR-CCM+.

6.3 The P5E Subsea Choke Valve

The P5E subsea choke valve from Master Flo Valve (USA) Inc., as shown in Fig. 6.1, is a bolted bonnet choke valve. The P5E can handle upto maximum pressures of 340 bar and has a valve flow coefficient/valve coefficient, C_v, of 250 at fully open condition. The valve flow coefficient, C_v, equation for gasses are more intricate as compared to liquids. C_v when the upstream pressure equals/exceeds approximately two times the downstream pressure, i.e., under *choked* conditions (see Sec. 7.1) is defined as

$$C_v = \hat{Q}_G \sqrt{\frac{S_g \times \hat{T}_b}{816 \times \hat{p_0}}}, \tag{6.1}$$

where, $\hat{Q}_G$, is the gas flow in standard cubic feet per hour, S_g, is the specific gravity of the gas, $\hat{T}_b$, is the absolute temperature in °R (°F + 460) and, $\hat{p}_0$, is the upstream pressure.

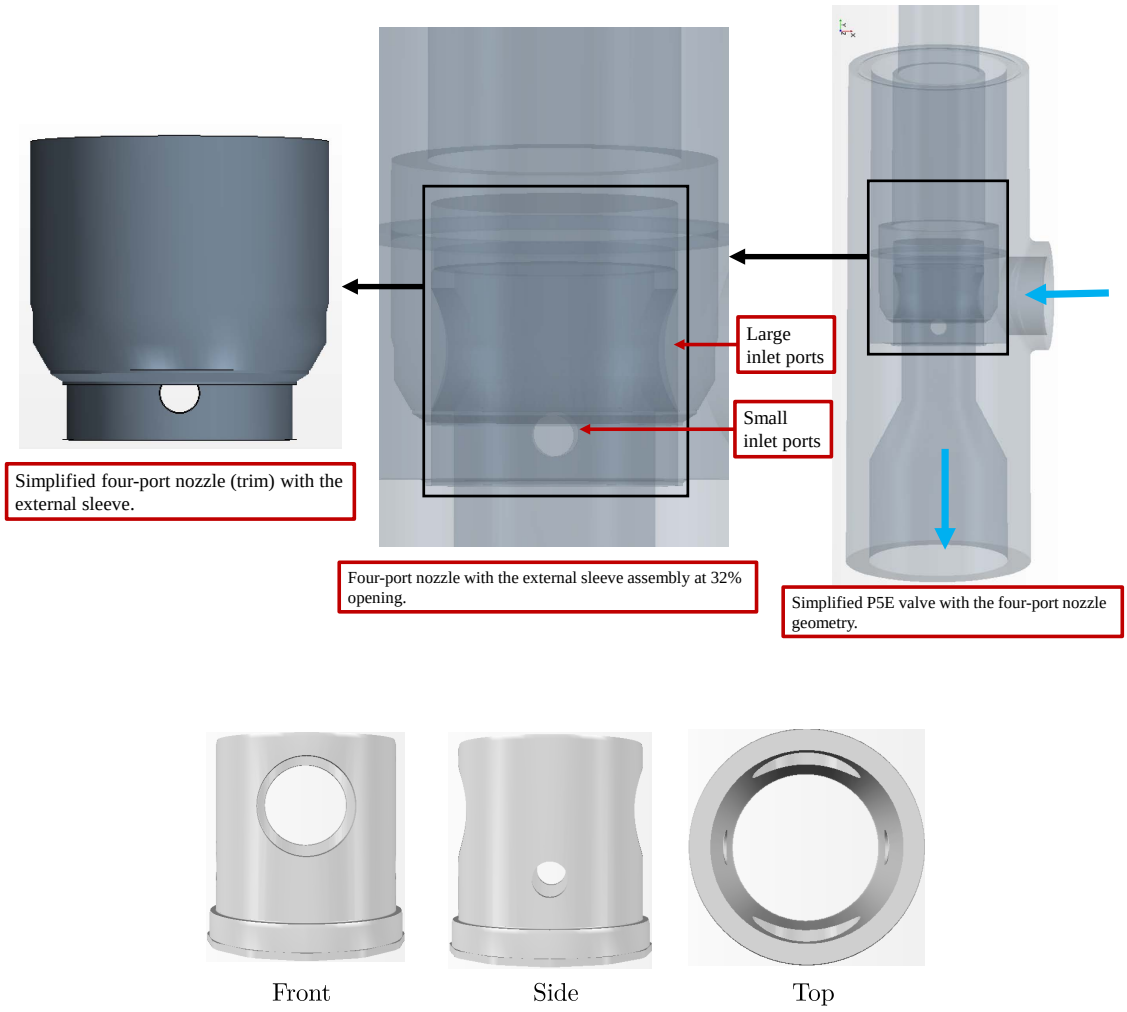

Figure 6.1: (Top) 3D-CAD view of the simplified P5E valve assembly with the FP nozzle from Master Flo Valve (USA) Inc. (Bottom) The original four-port nozzle for the P5E valve shown for comparison.

The maximum pressures depth of operation for the valve is 3300 meters below the mean sea level. A transparent 3D-Computer Aided Drafting (CAD) view of the valve assembly in Fig. 6.1 is shown at the critical 32% opening with the four-port (FP)

nozzle (see Fig. 6.1) with the external sleeve around it. At this stage, the two larger ports of the FP nozzle are fully closed and only the rest of the two smaller ports are fully open. The blue arrows in Fig. 6.1 represent the gas flow direction through the main inlet and outwards through the outlet.

7. Theory

7.1 Compressible Flow

In fluid mechanics, when the changes in density of a fluid flow are considerably high, the compressible flow behaviour of such flows become important and cannot be neglected anymore. It is convenient to assume incompressibility of the flow whenever possible as it simplifies computations, as the energy equation and temperature can be decoupled from the mass and momentum equations, unlike the case of a compressible flow. Although, it should be noted that incompressible flow (Flows with Mach number less than 0.3) does not imply that the fluid by itself is incompressible, i.e., under the right conditions even compressible fluids can be modelled as an incompressible flow. Similarly, in the case of the natural gas flow within the valve, the flow is compressible in nature and the extent of this compressibility needs to be captured as it can affect the valve performance and reliability.

To quantify the compressibility of the flow, a non-dimensional number termed as the Mach number is used, which is the ratio of gas velocity, $\hat{V}_g$, to the speed of sound within the medium, $\hat{c}$,

$$M = \frac{\hat{V}_g}{\hat{c}}, \tag{7.1}$$

where, $\hat{c}$, in dry air at standard temperature and pressure (STP) is about 344 m/s. The flow is known to be subsonic when $M < 1$ and is supersonic for $M > 1$. Regions where both subsonic and supersonic flow occurs, the flow is referred to be transonic. It is important to note that at a Mach numbers of 1, a shock is generated. By definition, a shock can be characterized by an abrupt, discontinuous, change in pressure, temperature, and density of the fluid [111, 112]. The shock propagates as a disturbance within the fluid at (or above) the local speed of sound.

Two cases arise in terms of propagation of the shock. The first case when the fluid flow is comparatively slower than the local $\hat{c}$, the resulting wave will be propagating in both the upstream and downstream direction within the flow. This is because of the fact that a part of the pressure wave will have a velocity in the upstream direction. On the contrary, if the fluid flow speed is greater or equal to the speed of sound, i.e., $\hat{V_g} \geq \hat{c}$, the propagating waves from the discontinuous shock will only propagate in the downstream direction. Hence, the fluid flow travelling from the upstream direction will experience the rapid pressure gradient (i.e. shock) when it reaches the pressure wave at $M = 1$. Therefore, such a pressure wave will be accompanied with the rapid pressure gradient. This pressure wave is known as a shock wave [111]. An important phenomena that takes place when the Mach numbers in a flow exceed one, called *choking* [113]. It is a limiting condition which implies that the mass flow rate will not change when the downstream pressure is decreased. This is because when the downstream pressure is reduced, this information of the change will propagate downstream with the speed of sound relative to the fluid, and because of the presence of a shock wave, will therefore never reach upstream.

Necessary assumptions need to be made regarding the relations between the pressure, $\hat{P}$, density, $\hat{\rho}$, and temperature, $\hat{T}$. One of the most common relations can be formed when the gas is assumed to be ideal. For an ideal gas, the equation of state (EOS) is very simple and can be described by the ideal gas law,

$$\hat{P} = \hat{\rho}\hat{R}_s\hat{T}, \tag{7.2}$$

where, $\hat{R}_s$, is the specific gas constant and is given by, $\hat{R}_s = \hat{R}_u/\hat{M}_w$, $\hat{R}_u$ is the universal gas constant given by $\hat{R}_u = 8314.472\ J/(kg \cdot K)$ and $\hat{M}_w$ is the mean molecular weight of the gas. Thus, the physical model of the gas that underlies the idea gas law EOS assumes that all the gas molecules have negligible volume, and the

potential energy associated with intermolecular forces is also negligible. Moreover, $\hat{R}_s$, can also be defined as the difference between the specific heat capacities of the gas, $\hat{R}_s = \hat{C}_p - \hat{C}_v$. Here, $\hat{C}_p$ and $\hat{C}_v$ are the specific heat values at constant pressure and volume, respectively. Now, for an isentropic flow (i.e. entropy remains constant),

$$\frac{\hat{P}}{\hat{\rho}^{\gamma}} = constant, \tag{7.3}$$

where γ is the specific heat ratio and is given by, $\gamma = \hat{C}_p/\hat{C}_v$. Generally speaking, isentropic flow assumption only holds true at boundaries, i.e., can be used to calculate boundary conditions, in the case of a compressible flow [111, 114]. This is because the boundary layer region adjacent to the wall/surface where the friction and thermal effects are strong and the shock waves, where the entropy increase across these shocks, invalidate the assumption of isentropic flow. Although it is important to note that the flow along a streamline between shocks can be subjected to a hypothetically adiabatic or isentropic stagnation process. Using this isentropic assumption, the equations defining the flow can be determined using the Bernoulli equation, which describes the correlation between velocity, pressure, temperature and density in a one dimensional space. Finally, when the steady-state adiabatic energy equation or the momentum equation is applied between two points inside a duct with variable area, the following relation can be derived [114],

$$\frac{\mathrm{d}\hat{a}}{\hat{\mathrm{A}}} = (M^2 - 1)\frac{\mathrm{d}\hat{U}}{\hat{U}}, \tag{7.4}$$

where $\hat{a}$ is the variable cross sectional area of the duct and $\hat{U}$ is the average flow velocity. Based on Eq. 7.4, it can be observed that when $M > 1$ and $\mathrm{d}\hat{a} > 0$, would result in a positive velocity increase. Whereas if $M < 1$ and $\mathrm{d}\hat{a} > 0$, velocity will decrease, a synonymous property observed for a Bernoulli flow. In addition to that, we have seen choking can occur when the flow is supersonic, i.e., $M > 1$, but irrespective

of that criteria, when a restriction is present in a flow, choked flow occurs (i.e. the flow becomes supersonic) when the ratio of the pressure at the restriction, $\hat{p}^*$, to the upstream pressure, $\hat{p}_0$, falls below the critical pressure ratio,

$$p_{cr} = \frac{\hat{p}^*}{\hat{p}_0} = \left(\frac{2}{\gamma+1}\right)^{\frac{\gamma}{\gamma-1}} = 0.54 \text{ for methane.} \tag{7.5}$$

What we have in our case is essentially a flow through a nozzle (i.e. ports), with highly pressurized gas from upstream (approx. 280 bar) will expand, i.e., reduction in pressure, as it is passed through the valve-nozzle. Because of a downstream pressure of about 90 bar, there is a large pressure drop across the nozzle with, $p_{cr} < 0.20$, the flow will form a supersonic jet right at the port exit. Since, this adverse pressure gradient (APG) is present, the pressure of this supersonic jet leaving the nozzle ports will still be above the downstream pressure. Hence, the pressure of the leaving jet won't be able to expand completely to match this lower pressure. This is known as an underexpanded jet [115, 116]. To quantitatively assess the appearance of an underexpansion in the exit jets, the following nozzle pressure ratio (NPR) is defined [115],

$$\eta_0 = \frac{\hat{p}_0}{\hat{p}_{exit}}. \tag{7.6}$$

Here, $\hat{p}_{exit}$, is the exit pressure or the ambient pressure at the outlet of the nozzle. According to Franquet *et al.* [115], highly underexpanded jets occur when the following criterion is satisfied,

$$\eta_0 \geq \frac{\hat{p}_0}{\hat{p}_c}, \tag{7.7}$$

with $\hat{p}_c$ being the critical pressure of the gas. An underexpanded jet structure consists of the Prandtl-Meyer expansion fans, barrel-shape shock, Mach disk (MD), and, reflected shock at the triple point and slip line [99, 117, 118].

Furthermore, the ideal gas EOS is unable to perfectly describe the thermodynamical behavior of the flow in cases where extreme pressure and temperature is present. To

better describe the real behavior of the gas, a factor called the coefficient of discharge, C_D, (see Appendix C in [115]) can be incorporated which provides improved estimation of mass flow rate and EOS influence at the nozzle-exit. It should be kept in mind that the abovementioned descriptions are for the case of release of a highly pressurized gas in a quiescent medium. The dynamics of the FP nozzle can be far more complex as there will be head-on turbulent jet interactions, after exiting from the two ports [119].

As discussed above, even though the ideal gas EOS can be used with reasonable accuracy for most cases, it is still a hypothetical model of a gas. When dealing with gases of high pressure, near condensation and/or critical points, real (non-hypothetical) models should, instead, be used that consider space-occupying molecules interacting with each other. Furthermore, to account for Joule-Thompson effect, real gases have to be considered. This deviation of real gasses from ideal case can be described by a gas deviation factor called the compressibility factor, given by,

$$Z = \frac{\hat{P}}{\hat{\rho}\hat{R}_s\hat{T}}. \tag{7.8}$$

There are various models describing the real gas behaviour with the most simplest one as Van der Waals EOS [114]:

$$\hat{P} = \frac{\hat{R}_u\hat{T}}{\hat{V}_m - \hat{b}_v} - \frac{\hat{a}_v}{\hat{V}_m^2}. \tag{7.9}$$

Here, $\hat{V}_m$, is the molar volume of the gas. This mode consists of two dimensional parameters, $\hat{a}_v$ and $\hat{b}_v$, that can determined empirically or be estimated from the gas's critical temperature, $\hat{T}_c$ and critical pressure, $\hat{p}_c$ using theorized relations:

$$\begin{aligned} \hat{a}_v &= \frac{27\hat{R}_u^2\hat{T}_\mathrm{c}^2}{64\hat{p}_\mathrm{c}}, \\ \hat{b}_v &= \frac{\hat{R}_u\hat{T}_\mathrm{c}}{8\hat{p}_\mathrm{c}}. \end{aligned} \tag{7.10}$$

The van der Waals EOS provides a reasonable enough approximation for gases near their critical point, where the ideal gas law loses its validity. Additionally, the Redlich–Kwong EOS is another two parameter EOS similar to Van der Waals equation, but is more accurate. The other models include Berthelot and modified Berthelot model, Clausius model, Wohl model, etc. For modeling the natural gas (i.e., 70% methane approximately) in this study, Peng-Robinson [120] EOS is used because of its unique property of being able to model liquids as well as real gases and is commonly used to model natural gas processes [121]. It is defined as

$$\hat{P} = \frac{\hat{R}_u \hat{T}}{\hat{V}_\mathrm{m} - \hat{b}} - \frac{\hat{a}\alpha(\omega)}{\hat{V}_\mathrm{m}\left(\hat{V}_\mathrm{m} + \hat{b}\right) + \hat{b}\left(\hat{V}_\mathrm{m} - \hat{b}\right)}, \tag{7.11}$$

where,

$$\begin{aligned} \hat{a} &\approx\ 0.45724 \frac{\hat{R}_u^2 \hat{T}_c^2}{\hat{p}_c}, \\ \hat{b} &\approx\ 0.07780 \frac{\hat{R}_u \hat{T}_c}{\hat{p}_c}, \end{aligned} \tag{7.12}$$

and the dimensionless parameters, α, κ, and, the accentric factor, ω, are given by,

$$\begin{aligned} \alpha(T_r) &= \left(1 + \kappa\left(1 - T_r{}^{\frac{1}{2}}\right)\right)^2, \text{ where, } T_r = \frac{\hat{T}}{\hat{T}_c}, \\ \kappa(\omega) &\approx\ 0.37464 + 1.54226\,\omega - 0.26992\,\omega^2. \end{aligned} \tag{7.13}$$

Empirically-determined accentric factor, critical volume, and critical temperature of methane has been used as reported by the Royal Dutch Shell PLC (see Table 7.1).

Additionally, there is a significant temperature drop when natural gas is choked through the nozzle of the valve. This is due to the Joule–Thomson effect, where the temperature of a real gas changes when it is throttled or undergoes expansion at the nozzle-exit under isoenthalpic conditions. Real gas models are able to capture the near nozzle-exit temperature which cannot be captured by employing ideal gas assumptions

Table 7.1: Methane gas specifications

Property	
Molecular weight	16.043 kg/kmol
Critical temperature ($\hat{T}_c$)	190.6 K
Critical pressure ($\hat{p}_c$)	46 bara
Critical volume	46 cm^3/mol
Accentric factor (ω)	0.0080
Density	0.657 kg/m^3
Dynamic viscosity	1.11906×10^{-5} Pa-s
Specific heat capacity ($\hat{C}$)	2240.07 J/kg-K
Thermal conductivity	0.0348195 W/m-K
Turbulent Prandtl number	0.9

because of the negative Joule-Thomson (JT) coefficient, defined as:

$$\hat{\mu}_J = \left[\frac{\partial \hat{T}}{\partial \hat{p}}\right]_{\hat{h}}, \tag{7.14}$$

$\hat{\mu}$ represents the enthalpy of the process. This JT coeffecient is of importance and dependent on the properties of the gas or its mixture and gas flow rate. It also accounts for negative or positive temperature at low or high pressures and is of interest for gas production/injection processes [122, 123]. The Joule-Thomson effects takes place at high NPRs as in the case of the expansion of a supersonic jet at nozzle-exit, and is predicted by Peng-Robinson EOS for real gases [124]. The real-gas EOS can also be used to predict temperatures up to cryogenic conditions upstream of the MD [125], which is accompanied by the underexpanded methane jet [126]. As reported by Hamzehloo *et al.* [127] in a comparative study between underexpanded methane and hydrogen jets, mixing was not observed for methane before the MD. This can be explained by the lack of turbulent fluctuations at the nozzle-exit. Consequently, Gortler vortices [128] are not generated and the mixing process will not be initiated before the MD.

7.2 Governing Equations

It is well-known that the quantities such as mass, mommentum, and energy are conserved, according to continuity, Newton's second law of motion and the first law of thermodynamics respectively. These three quantities can be described using the differential form of the continuity equation which describes the transport of a conserved quantity, $\hat{\phi}$, as:

$$\frac{\partial \hat{\phi}}{\partial \hat{t}} + \nabla \cdot \hat{f} = \hat{s}, \tag{7.15}$$

here, $\hat{f}$, is the flux of the conserved quantity and $\hat{s}$, being the source term. The differential forms (strong form) of the governing equations are described in this section. This form enables one to define the conditions at every point over the domain and is satisfied by the solution of it.

To begin with, the conservation of mass can be defined by the continuity equation as [114],

$$\frac{\partial \hat{\rho}}{\partial \hat{t}} + \nabla \cdot (\hat{\rho}\hat{U}) = 0, \tag{7.16}$$

where, $\hat{U}$, is the fluid velocity and , $\hat{\rho}$, is the density. Similarly, in Einstein notation,

$$\frac{\partial \hat{\rho}}{\partial \hat{t}} + \frac{\partial (\hat{\rho}\hat{U}_i)}{\partial \hat{x}_i} = 0. \tag{7.17}$$

The conservation of momentum equation, which is also known as the Navier-Stokes (NS) equations are given as [114],

$$\underbrace{\hat{\rho}\frac{\partial \hat{U}_i}{\partial t}}_{Local} + \underbrace{\hat{\rho}\hat{U}_i\frac{\partial \hat{U}_i}{\partial \hat{x}_j}}_{Convective} = \underbrace{\frac{\partial \hat{\tau}_{ij}}{\partial \hat{x}_j}}_{Diffusive} + \underbrace{\hat{\rho}\hat{G}_i}_{Source}, \tag{7.18}$$

where, the body force, $\hat{G}_i$, is the gradient of a potential function and, $\hat{\tau}_{ij}$, is the stress

on the fluid, which is defined as:

$$\hat{\tau}_{ij} = -\hat{p}\delta_{ij} + \hat{\mu}\left(\frac{\partial \hat{U}_i}{\partial \hat{x}_j} + \frac{\partial \hat{U}_j}{\partial \hat{x}_i}\right), \tag{7.19}$$

where, $\hat{p}$, is the pressure and, δ_{ij}, is the Kronecker delta. Note that the momentum Eq. 7.18 consists of three sub-equations in each spacial direction.

Similarly, considering the first law of thermodynamics the conservation of energy is described by [114],

$$\underbrace{\frac{\partial(\hat{\rho}\hat{E})}{\partial t}}_{Local} + \underbrace{\nabla \cdot (\hat{\rho}\hat{E}\hat{U}_i)}_{Convective} = \underbrace{\nabla \cdot (\hat{\kappa}_c \nabla \hat{T})}_{Diffusive} + \underbrace{\hat{q}}_{Source}, \tag{7.20}$$

where, $\hat{\kappa}_c$, the thermal conductivity, $\hat{E}$, is the total energy of the system and, $\hat{q}$, is the heat source.

Now, it can be noticed that the there are four main terms in the momentum equations, Eq. 7.18, and energy equations, Eq. 7.20, namely, the local term, the convective term, the diffusive term, and the source term as presented. In the case of turbulent flow, the pressure and velocity are always fluctuating and these fluctuations can be quantified to evaluate the strength of the turbulence. Each of these two quantities can be decomposed into a mean part and a fluctuating part using what is called the Reynolds decomposition and can be defined for the velocity part as follows,

$$\hat{u}_i = \hat{\bar{u}}_i + \hat{u}'_i, \tag{7.21}$$

where, $\hat{\bar{u}}_i$, is the mean flow velocity, which is averaged over a short time and, $\hat{u}'_i$, is the fluctuating velocity component. Substituting this velocity expression into the NS equations (Eq. 7.18) and averaging the terms with respect to time, gives rise to the equation that governs the mean flow, namely the Reynolds-averaged Navier–Stokes

(RANS) equations [129],

$$\hat{\rho}\left(\frac{\partial \hat{\tilde{u}}_i}{\partial \hat{t}} + \hat{\tilde{u}}_j \frac{\partial \hat{\tilde{u}}_i}{\partial \hat{x}_j}\right) = \hat{\rho}\hat{\tilde{G}}_i + \frac{\partial}{\partial \hat{x}_j}\left(\hat{\tilde{\tau}}_{ij} - \hat{\rho}\overline{\hat{u}_i'\hat{u}_j'}\right). \tag{7.22}$$

Moreover, because of the the non-linearity in the NS equations, the velocity fluctuations still appear in the RANS equations through the additional term, $-\hat{\rho}\overline{\hat{u}_i'\hat{u}_j'}$. This is term is called the Reynolds stress tensor, $\hat{R}_{ij}$. Upon expansion of the Reynolds stress tensor, it can be observed that, $\hat{R}_{ij}$, consists of six independent stresses. Therefore, including the turbulent fluctuations, the system now has a set of of 11 independent variables, i.e., five from NS equations and six independent stresses. But since we are still left with five equations (1 continuity, 3 momentum, and 1 energy), this gives rise to what is known as the *closure problem of turbulence*. The first to tackle this *closure problem* was Joseph Valentin Boussinesq, where he introduced the concept of *eddy viscosity* in the year of 1877 [130]. When Boussinesq hypothesis is applied to, $\hat{R}_{ij}$, a proportionality constant called the turbulence eddy viscosity, $\hat{\mu}_t$, is introduced where, $\hat{\mu}_t > 0$, as follows,

$$\overline{\hat{u}_i'\hat{u}_j'} = \hat{\mu}_t \underbrace{\left(\frac{\partial \hat{\tilde{u}}_i}{\partial \hat{x}_j} + \frac{\partial \hat{\tilde{u}}_j}{\partial \hat{x}_i}\right)}_{2\hat{S}_{ij}} - \frac{2}{3}\hat{k}\delta_{ij}, \tag{7.23}$$

where, $\hat{S}_{ij}$, is the mean rate of strain tensor and, $\hat{k}$, is the turbulent kinectic energy defined as

$$\hat{k} = \frac{1}{2}\overline{\hat{u}_i'\hat{u}_j'}. \tag{7.24}$$

Schemes following such approach are generally termed as eddy viscosity models or EVM's, such as the Spalart–Allmaras (S-A), k-ϵ (k–epsilon), and k-ω (k–omega) models. The difference between the S–A model and latter two is that S-A uses one additional equation to model turbulence viscosity transport, while the k-ϵ and k-ω models use two transport equations. overall these three models provide a relatively low-cost computation for the turbulent viscosity term, $\hat{\mu}_t$.

7.2.1 RANS Models

The $\hat{k} - \hat{\epsilon}$ turbulence model has been used for industrial applications since its introduction in 1972 by Jones and Launder [131]. It is a two-equation model that solves transport equations for the turbulent kinetic energy, $\hat{k}$, and the turbulent dissipation rate, $\hat{\epsilon}$, in order to determine the turbulent eddy viscosity,

$$\hat{\mu}_t = \hat{\rho} C_\mu \frac{\hat{k}^2}{\hat{\epsilon}}, \tag{7.25}$$

where, C_μ is a proportionality constant. The $\hat{k}-\hat{\epsilon}$ model has multiple variants available for use depending on the flow conditions. On the other hand, the S-A turbulence model is a one-equation model first introduced in 1992 [132]. It was developed for the aerospace industry and gained popularity because of its advantage of being applicable in an unstructured CFD solver. It solves a transport equation for a quantity called the modified diffusivity, $\hat{\tilde{\mu}}$, in order to determine the turbulent eddy viscosity which is defined in the S-A model as

$$\hat{\mu}_t = \hat{\tilde{\mu}} f_{v1}, \quad f_{v1} = \frac{\chi^3}{\chi^3 + C_{v1}^3}, \quad \chi = \frac{\hat{\tilde{\mu}}}{\hat{\mu}}, \tag{7.26}$$

here, C_{v1} is a model coefficient. The Reynolds Stress Transport (RST) models [133, 134], directly calculate the components of the Reynolds stress tensor, $\hat{R}_{ij}$. The RST models solve for seven equations: six equations for the symmetric tensor, $\hat{R}_{ij}$, and one equation for the isotropic turbulent dissipation, $\hat{\epsilon}$, requiring a substantial computational overhead because of these equations being numerically stiff.

Similar to the $\hat{k} - \hat{\epsilon}$ model, the $\hat{k} - \hat{\omega}$ turbulence scheme, a two-equation model introduced by D.C.Wilcox in 1998 [135, 136]. $\hat{k} - \hat{\omega}$ solves the transport equation in order to determine the turbulent eddy viscosity equations for the turbulent kinetic energy, $\hat{k}$. But instead of evaluating the turbulent dissipation rate similar to the $\hat{k} - \hat{\epsilon}$

model, it solves for the specific dissipation rate, $\hat{\omega}$, i.e., the dissipation rate per unit turbulent kinetic energy. Hence, for the $\hat{k}-\hat{\omega}$ model, the kinematic eddy viscosity required for RANS is given as

$$\hat{\nu}_t = \frac{\hat{k}}{\hat{\omega}}. \tag{7.27}$$

Wilcox [135] claims the superiority of the $\hat{k}-\hat{\omega}$ over the $\hat{k}-\hat{\epsilon}$, and how the omega transport equation is more robust over other scale equations present. A major advantage of the $\hat{k}-\hat{\omega}$ over the $\hat{k}-\hat{\epsilon}$ is its improved performance in the boundary layers, especially in the presence of APG as in the case of the flow inside the choke valve. But one of the biggest disadvantage of the $\hat{k}-\hat{\omega}$, in its original form, is that the boundary layer computations are quite sensitive to the values of $\hat{\omega}$ in the free-stream or the valve inlet in our case. But this problem was addressed by Menter in 1994 [137] via introducing a modified version of the $\hat{k}-\hat{\omega}$ model called the Menter's Shear Stress Transport (SST) $\hat{k}-\hat{\omega}$ model. The modified equation looks very similar to the $\hat{k}-\hat{\omega}$ model, but has an additional non-conservative cross-diffusion term, $CD_{k\omega} = f(\nabla\hat{k}\cdot\nabla\hat{\omega})$, (see Eq. B.7). Inclusion of this term in the $\hat{\omega}$ transport equation makes the $\hat{k}-\hat{\omega}$ model capable to produce identical results to the $\hat{k}-\hat{\epsilon}$ model. The turbulence kinetic energy equation in the SST $\hat{k}-\hat{\omega}$ can be shown as [137, 138],

$$\frac{\partial\hat{k}}{\partial\hat{t}} + \frac{\partial(\hat{U}_j\hat{k})}{\partial\hat{x}_j} = \hat{P}_k - \beta^*\hat{\omega}\hat{k} + \frac{\partial}{\partial\hat{x}_j}\left[(\hat{\nu}+\sigma_k\hat{\nu}_t)\frac{\partial\hat{k}}{\partial\hat{x}_j}\right], \tag{7.28}$$

and the specific dissipation rate equation as

$$\frac{\partial\hat{\omega}}{\partial\hat{t}} + \frac{\partial(\hat{U}_j\hat{\omega})}{\partial\hat{x}_j} = \alpha\hat{S}^2 - \hat{\beta}\hat{\omega}^2 + \frac{\partial}{\partial\hat{x}_j}\left[(\hat{\nu}+\sigma_\omega\hat{\nu}_t)\frac{\partial\hat{\omega}}{\partial\hat{x}_j}\right] + 2(1-F_1)\frac{\sigma_{\omega 2}}{\hat{\omega}}\frac{\partial\hat{k}}{\partial\hat{x}_j}\frac{\partial\hat{\omega}}{\partial\hat{x}_j}, \tag{7.29}$$

where, $\hat{\beta}$, is the coefficient of thermal expansion and, $\hat{S}$, is the modulus of the mean rate of strain tensor. A comprehensive definition for the closure coefficients and auxilary relations for the SST $\hat{k}-\hat{\omega}$ model can be found in Appendix B.2.1.

7.2.2 Scale-Resolving Models

In contrast to the RANS schemes, scale-resolving models fully resolve the large scales of turbulence and capture the small-scale motions within the flow. The two well-known models among them are the Large Eddy Simulation (LES) and Detached Eddy Simulation (DES). LES uses Kolmogorov's theory of self similarity, i.e., the large-scale eddies of the flow are dependant on the length scale of the geometry while the smaller scales are more universal in nature. This allows to explicitly solve for the larger eddies by direct calculations and implicitly account for the smaller eddies by using a subgrid-scale (SGS) model. Although LES is popularly used in flows with low Reynolds numbers, it comes with a high computational cost. This is because of the fact that in order to resolve the turbulent structures near to the wall, this model requires an excessively high mesh resolution in and near the wall boundary layer. This includes the direction normal to the wall but also in the direction of the fluid flow. As a result of the high computational costs that go along with the high cell count. On the other hand, DES is a Hybrid of LES and the RANS approach. It resolves the turbulent structures in the flow away from the wall and models the near-wall and irrotational flow regions with RANS approach [139]. Therefore, DES avoids the expensive mesh resolution that is required by LES.

One of the biggest challenges in turbulence modelling is choosing the turbulence model itself. Numerous studies investigating the appropriateness of these models for different cases of internal flows and external flows are present in the literature. In context of the flow phenomenon inside of a choke valve, one of the most most commonly used CFD schemes to simulate mean flow during turbulent flow conditions is the $\hat{k} - \hat{\epsilon}$ model [140]. Due to the presence of the APG and studies performed in the literature [91, 141, 142], a combination of a type of DES model called the Delayed Detached Eddy Simulation (DDES) with SST $\hat{k} - \hat{\omega}$ has, moreover, been used, commonly known as SST $\hat{k} - \hat{\omega}$ DDES. DDES includes the molecular and turbulent

viscosity information into the switching mechanism, i.e., between LES and RANS, so as to delay this switching in boundary layers and is more robust in terms of RANS and LES distribution. The DDES formulation for the SST $\hat{k}-\hat{\omega}$ model can be obtained by modifying the dissipation term in the transport equation for the turbulent kinetic energy, as shown by Menter and Kuntz [143],

$$\hat{\tilde{\omega}} = \hat{\omega}\phi_{DES}, \tag{7.30}$$

where, ϕ_{DES}, is defined as:

$$\phi_{DES} = \max(l_{ratio}F, 1), \tag{7.31}$$

where, l_{ratio}, is the ratio of, $\hat{l}_{RANS}$, and, $\hat{l}_{LES}$. When, $\phi = 1$, the RANS solution can be recovered, while for , $\phi > 1$, the solution tends towards the LES formulation. A complete set of definitions and coefficients can be found in Appendix B.2.2.

7.2.3 Wall Treatment

In a fluid flow, the flow close to the wall, is retarded by the wall that applies shear stress to the fluid. The part of the flow that is affected by this retardation by the wall is known as the *boundary layer*. Since, walls are where vorticity is generated in most flows, an accurate prediction of the flow and turbulence parameters across the boundary layer region is extremely essential. The inner region of the boundary layer can be divided into three sub-layers: Viscous sub-layer, buffer layer, and log layer. Viscous sub-layer is the layer in contact with the wall which is mostly dominated by viscous effects. This layer is considered to be laminar, i.e., linear velocity profile. On the other hand, the log layer receives its name from the velocity profile, which changes logarithmically with depth within this region and is dominated equally by viscous and turbulent effects. The log layer extends until the effects of the outer geometry

Table 7.2: Description of, y^+, for different layers within the boundary layer.

Wall treatment	Extent of the sub-layer	
Low y^+	$y^+ < 5$	Viscous sub-layer
Intermediate y^+	$5 < y^+ < 30$	Buffer layer
High y^+	$30 < y^+ < aRe_{\hat{\tau}}$	Log layer

become important. This is usually quantified via the friction Reynolds number, Re_τ, which is both the Reynolds number defined with the friction velocity at the wall, and a measure of the outer scales. The logarithmic layer usually extends up to aRe_τ, where a depends on the geometry and $a < 1$. The transitional layer between viscous sub-layer and log layer is the buffer layer. The velocity profile in this region is not defined as the other two, but can be calculated using interpolation functions. Since, the velocity profile varies according to the distance to the wall a non-dimensional wall distance is defined as

$$y^+ = \frac{\hat{U}_f}{\hat{\nu}}\hat{y}, \tag{7.32}$$

where, $\hat{y}$, is the distance from the wall, $\hat{\nu}$, is the kinematic viscosity and, $\hat{U}_f$, is the friction velocity defined by,

$$\hat{U}_f = \sqrt{\frac{\hat{\tau}_0}{\hat{\rho}}}, \tag{7.33}$$

here, $\hat{\tau}_0$, is the wall shear stress. The three layers can be described using the, y^+, as shown in Table 7.2.

7.2.4 Coupled Solver

The coupled solver in STAR-CCM+ offers the *Coupled flow* and *Coupled energy* solvers [144]. The coupled solver in STAR-CCM+, solves the conservation equations for continuity, momentum (NS), energy in a coupled manner. The velocity field is calculated out from the NS equations. The pressure is obtained from the continuity and density is computed from the EOS [144]. Coupled energy solver is an extension to the coupled flow solver. One of the biggest advantages of using a coupled solver in

STAR-CCM+ is that it results in a more robust and accurate solution when dealing with a compressible flow having shocks [144, 145]. As a result, the coupled solver has a high computational overhead and also the number of iterations required by the coupled algorithm is more independent from the mesh size.

7.3 Vibration In Choke Valves

The transport of natural gas from the subsea wells, which are at higher pressures need to be reduced in order to deliver it to the production lines. This is substantial pressure drop is achieved by installing a choke module within the transition system. Because of the choking, enormous power gets dissipated at the choke and can be quantified as [106],

$$\hat{P}_{dissipated} = \Delta\hat{p} \cdot \hat{\dot{Q}}, \tag{7.34}$$

where, $\Delta\hat{p}$, is pressure drop across the choke in Pascals, and, $\hat{\dot{Q}}$, is the volumetric flow rate in m^3s^{-1}. For the P5E ,the energy dissipated at each of the two smaller ports at 32% of the maximum C_v, i.e., critical operation condition, is approximately 2.91 MW. As described by Vér and Beranek [146], only a small portion of the dissipated power is coherent in nature and therefore is converted to pressure oscillations or sound. The rest of the power is dissipated as heat. The magnitude of the dissipated power at the choke is in the orders of megaWatts (MW), the sound levels produced can be in the ranges of kiloWatts (kW) which can generate significant vibrations as a consequence [106]. The vibrations can be even more significant if there is a lack of damping property within the material of the valve. The range of frequencies that can drive this vibration amplification, i.e., resonance, depends on this intrinsic mechanical damping of the assembly [106]. These vibrations can cause mechanical failure through cyclic stresses and resonance [146].

The lower frequencies have vibrational eigenmodes that are global (less than 100 Hz), i.e., larger length scales, while the eigenmodes are more local at higher frequencies,

i.e., smaller length scales, with the 500–5000 Hz range being the most troublesome [106]. Also it is interesting to note that the frequencies that generate noise are typically far higher than the more catastrophic mechanical eigenfrequencies [91, 106]. As described by Ligterink *et al.* [106], the broadband frequency spectrum mainly depends on the characteristic length scale of the choke valve geometry, $\hat{L}_{choke}$, the speed of sound within the medium, $\hat{c}$, and the flow condition, i.e., subsonic/transonic/supersonic. The peak frequency, $\hat{f}_p$, within this spectrum is defined by,

$$\hat{f}_p = \frac{c}{L_{choke}}. \tag{7.35}$$

The pressure oscillations generated within the flow, which potentially give rise to the mechanical vibrations, are typically higher when the system resonates. In this case, at resonant frequency, the transfer of the vibrational energy into kinetic energy with minimal loss and this can eventually lead to failure of the structure. Hence, at mechanical resonant frequency, the large pressure oscillations will be maximum at the wall. As a result, determination of the natural resonant frequencies of the mechanical system, i.e., the eigenfrequencies, and their corresponding eigenmodes becomes of prime importance. Nevertheless, it should be remembered that the resonance corresponds to an eigenmode for an undamped mechanical system and, as a result, the extent a material dampens out the increased pressures due to resonance should be looked at. The amount of damping in a mechanical system is typically quantified using a damping factor/ratio, ζ. Depending on this damping factor, which has a typical range of 0.02-0.04 [106], the frequency band of, $\hat{f}$, around, $\hat{f}_0$, can be described using the relation,

$$(1-\zeta)\hat{f}_0 < \hat{f} < (1+\zeta)\hat{f}_0. \tag{7.36}$$

Hence, it is clear that a small damping factor will yield a smaller band with higher peaks, as compared to a larger, ζ. At the same time, the latter makes it difficult to evaluate

for certain, which damping factor will produce the larger peak pressures. Hence, as quantified by Ligterink *et al.* [106], the dissipated power is directly proportional to the square of the normalized amplitude of the resonance, φ, and the damping factor, ζ, and defined by,

$$\hat{P}_{loss} = -\frac{\mathrm{d}\hat{E}}{\mathrm{d}\hat{t}} = 2\zeta\hat{\omega}\hat{E} \simeq \zeta\hat{\omega}\hat{\varphi}^2, \tag{7.37}$$

where, $\hat{E}$, is the internal energy. Furthermore, because of the undamped condition of resonance, the peak stresses within the system can be identified by extracting the stress information per mode.

7.4 Signal Processing

Fourier Transformations (FT) are generally used to convert a transient signal into its frequency domain, so that the dominant modes of oscillations can be identified. Generally, a time FT of a real and periodic function which depends on the position and time, $\hat{h}(\hat{x};\hat{t})$, is defined over the whole time domain. Similarly, a finite FT can be calculated by integrating over a given period, $\hat{t} \in [-\frac{\hat{T}}{2}, \frac{\hat{T}}{2}]$, as:

$$FT_{\hat{t}}\{\hat{h}(\hat{x};\hat{t})\} = \int_{-\hat{T}/2}^{\hat{T}/2} \hat{h}(\hat{x}:\hat{t})e^{-i\hat{\omega}\hat{t}}\mathrm{d}\hat{t} = \hat{H}(\hat{x};\hat{\omega},\hat{T}) \;\forall\hat{\omega} \in [-\frac{n\pi}{\hat{T}}, \frac{n\pi}{\hat{T}}], \tag{7.38}$$

here, n, is the number of sampling points and, $\hat{\omega}$, is the angular frequency. Since, at times the transient signal can be aperiodic, violating the periodicity assumption for the FT, a window function can be used. Applying a window function before the FT is evaluated which makes the signal periodic, i.e., making sure the signal has a zero amplitude at both the start and the end by tapering the ends. Window functions helps avoid spectrum *leakage* [147, 148]. Among the various window functions available, the Hann (Hanning) function (see Eq.505 in [144]), named after Julius von Hann, is used before performing the FFT in this case.

8. Numerical Modelling

In numerical methods, the models have to be transformed into a system of algebraic relations, i.e., discretizing the governing equations in both the space and time domain for an unsteady problem. As the resulting set of equations are linear, therefore, an Algebraic Multigrid Solver (AMG) is used to solve the discretized linear system of equations iteratively. This approach is also used for finite volume method (FVM) and is explained here in detail in Section 8.1. The mesh used to convert the geometry into a discrete computational domain required for the FVM approach is described in Section 8.2. Finally, Boundary Conditions (BC) required to solve the equations at the computational domain are explained in Section 8.3.

8.1 Finite Volume Method

The finite volume method (FVM) is used by STAR-CCM+ to solve for the fluid flow. Here, each cell of the computation grid within the solution domain is considered as a control volume and similarly, the whole domain is subdivided into a set of finite number of such small control volumes, corresponding to the cells of the grid. The FVM solves the discretized versions of the integral form of Eq. 7.15 to Eq. 7.20, Eq. 7.28, and, Eq. 7.29, by integrating over the volume of each cell. The calculated solutions of the different physical properties are stored at each cell center, and is evaluated as an average over the whole volume of the cell.

To begin with solving the integral form of the set of governing equations mentioned above, the volume integral of the convective and diffusive terms are rewritten into their respective surface integral forms, using the Gauss's theorem, i.e., divergence theorem. The two convective and diffusive terms are then integrated over the surface of the cell. Hence, the integral form of the transport equation for a scalar quantity, $\hat{\phi}$,

over a control volume, $\hat{V}$, and applying the divergence theorem would give:

$$\underbrace{\frac{\mathrm{d}}{\mathrm{d}\hat{t}}\int_{\hat{V}}\hat{\rho}\hat{\phi}\mathrm{d}\hat{V}}_{Local}+\underbrace{\int_{\hat{A}}\hat{\rho}\hat{U}\hat{\phi}\mathrm{d}\hat{a}}_{Convective}=\underbrace{\int_{\hat{A}}\hat{\Gamma}\nabla\hat{\phi}\mathrm{d}\hat{a}}_{Diffusive}+\underbrace{\int_{\hat{V}}\hat{S}_{\phi}\mathrm{d}\hat{V}}_{Source}, \tag{8.1}$$

where, $\hat{A}$, is the surface area of the control volume and $\mathrm{d}\hat{a}$ represents the surface vector. The FVM discretization is illustrated in Fig. 8.1 for this generic transport equation. By setting, $\hat{\phi}$, and selecting appropriate values for the diffusion coefficient, $\hat{\Gamma}$, one can easily get the integral forms of the mass, momentum, and energy conservation equations.

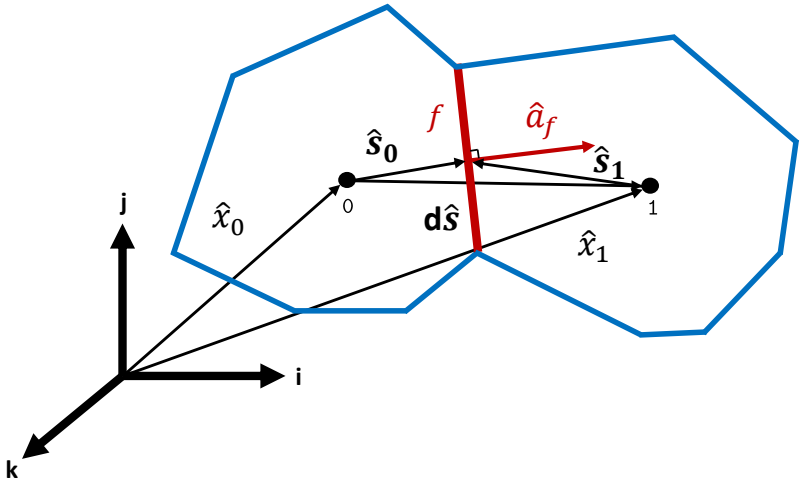

Figure 8.1: FVM discretization for two polyhedral cells. Here, $\hat{a}_f$, is the surface area vector for the face, $\hat{f}$, $\hat{s}_0$, and $\hat{s}_1$, are the source vectors from their respective cell centers and , $d\hat{s} = \hat{x}_1 - \hat{x}_0$.

The volume integrals of the local and source terms are evaluated as in their integrand forms. STAR-CCM+ offers multiple interpolation schemes which include, first-order upwind (FOU), second-order upwind (SOU), central differencing (CD), bounded central-differencing (BCD), hybrid MUSCL 3^{rd}-order/central-differencing (MUSCL3), etc. The MUSCL scheme stands for *Monotonic Upstream-centered Scheme for Conservation Laws* and the term was introduced by Bram van Leer in 1979 [149].

This was the first high-order, total variation diminishing (TVD) scheme with 2^{nd}-order spatial accuracy. Based on the problem, the MUSCL3, i.e., a 3^{rd}-order MUSCL scheme, has been used for discretizing the convective term. It is a finite volume method that provides numerical solutions with high accuracy including flows whose solutions exhibit shocks/discontinuities.

Now let us look into the discretized versions of each terms in Eq. 8.1. The convective term in Eq. 8.1, can be discretized at the cell face, $\hat{f}$, as

$$(\hat{\rho}\hat{U}\hat{\phi}.\hat{a})_f = \hat{\dot{m}}_f\hat{\phi}_f. \tag{8.2}$$

Here, $\hat{\dot{m}}_f$ is the mass flow rate at the face, $\hat{f}$. The MUSCL3 scheme uses a Normalized-Variable Diagram (NVD) value, ξ, similar to the convection scheme of BCD [144]. The NVD value is used to ensure that the MUSCL3 scheme is bounded. The scheme switches to the FOU scheme in regions having non-smooth flows and uses a blending function, which combines the MUSCL3 and a third-order CD scheme during regions of smooth local flows, which is defined by [144]:

$$(\hat{\dot{m}}\hat{\phi})_f = \begin{cases} \hat{\dot{m}}\hat{\phi}_{FOU}, \text{ for, } \xi < 0 \text{ or } \xi > 1, \\ \hat{\dot{m}}(\sigma_{MUSCL3}\hat{\phi}_{MUSCL3} + (1-\sigma_{MUSCL3})\hat{\phi}_{CD3}), \text{ for, } 0 \leq \xi \leq 1, \end{cases} \tag{8.3}$$

where, σ_{MUSCL3}, is a user-defined model parameter utilized to control the numerical dissipation which is set to 0.9 in this case based on recommendations from SIEMENS. $\hat{\phi}_{MUSCL3}$, is the reconstructed value from the MUSCL3, i.e., 3^{rd}-order upwind scheme, and , $\hat{\phi}_{CD3}$, is the face center value of a cell obtained through 3^{rd}-order CD interpolation. Although, it should be noted that the accuracy of σ_{MUSCL3} is reduced to second order near regions involving strong shocks. Therefore, MUSCL3 scheme provides reduced dissipation, i.e., monotonic [112], and is more robust while simulating high-speed compressible flows as compared to other BCD schemes.

In numerical methods, the time derivative need to be discretized differently than the spatial derivative, i.e., the total physical time interval is subdivided into numerous time steps. 2^{nd}-order temporal discretization has been used for local term. This time integration scheme is generally described by the number of time levels used for integration and also the time level at which the flux terms and source terms are being integrated. For the time derivative within the local term in this case, an *Implicit Euler* scheme, i.e., backward differencing (BD), is used. As the name suggests, the difference of the values from the current and the previous time steps are used for evaluating the derivative. The basic first-order scheme, when used to approximate the local term in Eq. 8.1 would turn to:

$$\frac{\mathrm{d}}{\mathrm{d}\hat{t}}\left(\hat{\rho}\hat{\phi}\hat{V}\right)_0 = \frac{\left(\hat{\rho}\hat{\phi}\hat{V}\right)_0^{n+1} - \left(\hat{\rho}\hat{\phi}\hat{V}\right)_0^{n}}{\Delta\hat{t}}, \tag{8.4}$$

where n is the current time level and $n+1$ is the previous time level. STAR-CCM+ also offers a high-accuracy temporal discretization, the BDF2Opt(5), i.e., the option of performing the 2^{nd}-order time discretization with five time levels. The BDF2Opt(5) is defined as:

$$\mathrm{BDF2Opt(5)} = \left(1 - \frac{1}{\sqrt{2}}\right)\mathrm{BDF4} - \left(\frac{5}{2} - 2\sqrt{2}\right)\mathrm{BDF3} + \left(\frac{1}{\sqrt{2}} + \frac{5}{2} - 2\sqrt{2}\right)\mathrm{BDF2}, \tag{8.5}$$

where, BDF2, BDF3, and BDF4 are the BD schemes which consider information from the previous two, three, and four time levels respectively [144]. The BDF2Opt(5) reduces the truncation error by a factor of 2.64 as compared to the basic BD2. Although, since unsteady flows exhibit a large spectrum of time scales, it is inefficient and cumbersome to compute the time-derivative terms using a single and constant time-step size. Therefore, a varying time step scheme, based on the CFL condition, which relies upon a user defined Courant number, called the adaptive time step has

been used to stabilize the solution; see Implicit Time-Stepping, Eq. 908, [144].

The diffusive term in Eq. 8.1 can be written as:

$$\hat{D}_f = \left(\hat{\Gamma}\nabla\hat{\phi}.\hat{a}\right)_f, \tag{8.6}$$

where, $\hat{\Gamma}$ is the face diffusivity. In order to define the fully discretized diffusive flux, $\hat{D}_f$, an accurate second order expression for the interior face gradient, $\nabla\hat{\phi}_f$, is defined and the fully decomposed diffusive flux at an interior face of the cell can then be written as [144]:

$$\hat{D}_f = \hat{\Gamma}_f \nabla\hat{\phi}_f.\hat{a}_f = \hat{\Gamma}_f \underbrace{\left[(\hat{\phi}_1 - \hat{\phi}_0)\overrightarrow{\hat{\alpha}_D} + \overline{\nabla\hat{\phi}} - (\overline{\nabla\hat{\phi}}.\mathrm{d}\hat{s})\overrightarrow{\hat{\alpha}_D}\right]}_{\nabla\hat{\phi}_f} .\hat{a}. \tag{8.7}$$

Here, $\hat{\Gamma}_f$ is the harmonic average of face diffusivity from the cells, $\overrightarrow{\hat{\alpha}_D} = \frac{\hat{a}}{\hat{a}.\mathrm{d}\hat{s}}$, and $\overline{\nabla\hat{\phi}}$ is average of the gradient of the cell values, $\hat{\phi}_0$, and, $\hat{\phi}_1$. In a similar way, the discretization can be extended at the boundary face as [144]

$$\hat{D}_f = \hat{\Gamma}_f \left[(\hat{\phi}_f - \hat{\phi}_0)\overrightarrow{\hat{\alpha}_D} + \nabla\hat{\phi}_0 - (\nabla\hat{\phi}_0.\mathrm{d}\hat{s})\overrightarrow{\hat{\alpha}_D}\right] .\hat{a}. \tag{8.8}$$

Here, $\mathrm{d}\hat{s} = \hat{x}_f - \hat{x}_0$. In addition to the values at the cell center in the FVM method, it must be calculated at the cell faces This requirement is fulfilled by developing variable gradients at cell centers as well as cell faces.

Gradients are also required to calculate the cross-diffusion term, i.e., secondary gradient, within the diffusive flux in Eq. 8.7 and Eq. 8.8, for the pressure gradients which are required for the pressure-velocity coupling. Moreover for calculating the strain and rotation rates in the turbulence models, gradients are utilized. STAR-CCM+ uses a Hybrid Gauss-Least Squares method originally developed by Shima *et al.* [150] in 2013. This method uses a blending factor, β, in order to select between the Least

Square method (LSQ), i.e., a blending factor of 1, and the Green-Gauss method (GG), i.e., blending factor of 0. Anything in between chooses a hybrid between the two [144]. Moreover, the gradient of a quantity must be limited in order to not have spurious oscillatory behaviour in the solutions. This will introduce new maxima/minima in the reconstructed face values [112] which can fall outside the range of the values in the neighboring cells. Therefore, to make sure the solutions are monotonic, i.e., no new maxima/minima is introduced, a Min-Mod flux limiter is used as it applies the least amount of limiting to the gradients. Additionally, sometimes the gradients can be excessively limited causing the convergence to slow down and consequently stall. To avoid this issue a Total Variation Bounded (TVB) gradient limiting scheme (see Eq. 859 in [144]) has been used after recommendations from SIEMENS, with an acceptable field variation factor, ψ, of 0.25 ($\psi = 1$, would mean no limiting at all). The TVB technique is extremely useful for high-fidelity, i.e., highly accurate, simulations using DES.

8.2 Meshing

There are two major steps of mesh generation in STAR-CCM+, the first is creating a surface mesh on the geometry and then developing a volume mesh from the generated surface mesh. Hence, the quality of the genrated volume mesh depends on that of the surface mesh. Capturing the geometry can be challenging, especially for complex designs such as the choke valve in the given problem. STAR-CCM+ recommends using the Surface Wrapper meshing model for such complex geometries as it captures the crtitical and minute features of the geometry [144]. Hence, initially a Surface Wrapper is used, and then the Surface Remesher meshing model is applied. As the initial surface of the geometry is not suitable for formation of a volume mesh, as it often consists of triangulated surfaces, i.e., tessellation, and contains highly skewed cells. The remeshing process improves the overall quality of these surfaces and eventually

the volume mesh.

For the volume mesh, an automated unstructured grid is generated using polyhedral cells. Additionally, the prism layer model is added to the mesh the near wall regions. STAR-CCM+ generates the polyhedral mesh from an underlying tetrahedral one using a dualization scheme, which makes it computationally costly as compared to the other available models. However, such scheme is recommended recommended for complex flows involving circulation. A typical polyhedral cell consists of 14 faces. The details of the mesh developed for this problem are shown in Table 9.1.

8.3 Boundary Conditions

In numerical methods such as the FVM, the convective and the diffusive fluxes satisfy all the interior cell faces. However, conditions need to be provided for the (outermost) cell faces at the boundaries of the computational domain. These conditions are generally termed as Boundary Conditions (BC). Hence, the solutions at the boundary surface are defined as a function of the applied BC and the values calculated from the interior cells. Mainly, there are two types of BCs used, the first being Dirichlet and the second Neumann type [112]. The former uses a constant specified value for the function at the boundary, whereas the latter uses a specified normal derivative of a function. In this case, for the compressible gas flow, the static temperature and static pressure has been specified at the boundaries, i.e., Dirichlet BC.

There are multiple ways of incorporating BCs in STAR-CCM+. The one used for this project, the pressure outlet, specifies the static pressure, i.e., downstream exit of the valve. Although, the pressure outlet condition is not recommended to be used as an inlet BC by SIEMENS, it has no such considerable effects on the results [145] (see Pressure Outlet in [144]).

9. Choke Valve Flow

For modelling the valve flow, a few assumptions and simplifications have been adopted, keeping in mind the reliability of the results in terms of the computation capacity. The natural gas, which is a multi-component fluid has been modelled as pure methane. In order to reduce the computational effort during the problem setup, necessary geometrical simplifications are carried out with the assistance from Master Flo Valve (USA) Inc. designing team. This has been achieved by stripping the exterior portions of the valve assembly, i.e., valve head parts and bolts.

9.1 Generated Mesh

As explained in Section 8.2, in order to solve the discretized (FVM) governing equations of the flow within the valve geometry, a mesh needs to be obtained. A fine mesh is desired for turbulent flows with unsteady phenomenon especially to capture details of the complex valve geometry. Since turbulence is broadband in nature, i.e., energy dissipation occurs over various length and time scales, fine meshes should be able capture the smaller length scale structures. Moreover, additional care must be taken close to the small nozzle port regions where high-velocity jets may form. Mesh refinement at regions of interest was not performed so as to avoid numerical reflection at the refined mesh boundaries [151, 152]. An unstructured volume mesh is generated using the combinations of surface wrapper, surface remesher, i.e., for the surface mesh, and polyhedral and prism layer mesher to extend the surface one to a volume mesh. The volume mesh is shown with one of the three planes (created using the derived plane feature in STAR-CCM+) used for visualizing the mesh and the solutions in Fig. 9.1. Among the total number of cells generated, only 13 had a face validity less than one, with the least face validity of 0.95-0.90 for two cells among the 13. The

mesh is also topologically valid and had no negative volume cells.

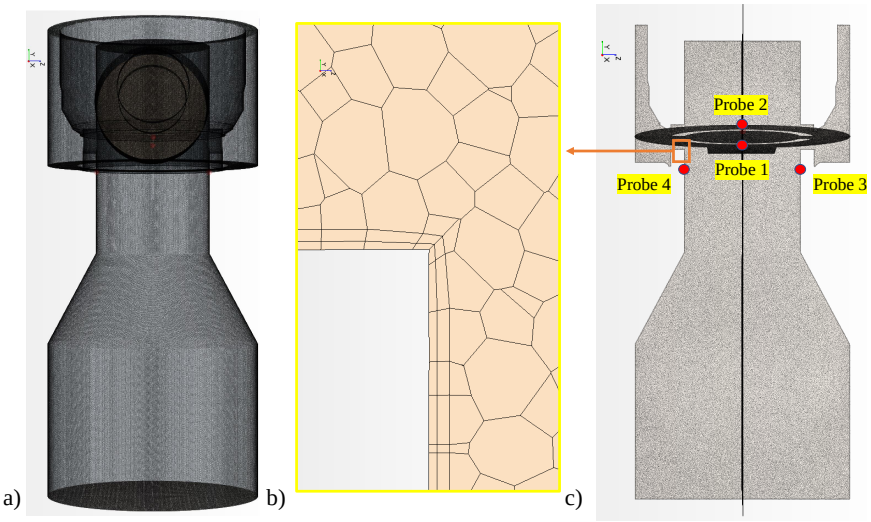

Figure 9.1: a) The generated volume mesh on the flow domain of the valve. b) Enlarged planar view of the generated volume mesh. c) The derived y-z plane (Plane A) and the four point probes where the pressure signals are measured.

The properties of the generated mesh are shown in Table 9.1. Two prism layers are used to model the boundary layer along with the high wall y+ treatment. A base size of 1 mm has been applied for the mesh cell size, as it is able to capture the critical details of the valve geometry. A higher resolution mesh with a base size of 0.5 mm was also generated to asses the mesh independence. A percentage change of 0.5% in accuracy is observed, which comes at a higher computational cost. Moreover, mesh quality was evaluated using the diagnostics tool available within STAR-CCM+ and it was found that 99.81% of the cells had ideal quality. Similarly, surface validity was checked to identify for any cells with zero surface area, which can cause an overflow or floating point error.

9.2 Implicit Unsteady Modelling

The implicit unsteady numerical approach is used since the time scales of the FIV phenomenon are of the same order as those of the convection and diffusion of the

Table 9.1: Properties of the generated mesh.

Mesh property	
Total # of cells	11,331,185
Base size	1 mm
Surface growth rate	1.3
# of prism layers	2
Prism layer thickness	33% of base size
Prism layer stretching	1.5

vortices being shed. Additionally, STAR-CCM+ offers ways to define the minimum and/or maximum inner iterations to converge to the solution within each physical time step. The minimum number of inner iterations is set to 15. Since the physical time step is dependent on the transient phenomenon that is being simulated, determination of its size is crucial. To capture the instantaneous velocities and pressure fluctuations critical to cause a FIV phenomenon, the time step needs to be decided based on the extent of the the frequency spectrum one wants to evaluate. Additionally, the mesh-cutoff frequency should always be checked in order to ascertain the generated mesh resolution is refine enough to capture them. These measures should be always taken in the case of unsteady-turbulent flows because of the fact that dissipation of the larger eddies in the turbulence energy cascade, i.e., broadband nature of turbulence [105]. A reasonable-enough physical time step must, therefore, be chosen, keeping in mind the machine epsilon limit [112] limit and the overall energy bill.

For this study, a physical time step of, $\Delta\hat{t} = 1 \times 10^{-6}$ s, has been chosen. The adaptive time stepping scheme is added to stabilize the flow solutions [144]. Since the sampling rate, i.e., physical time step, is critical to the FIV, lower and upper bound have been added to the physical time step change factor. The change factor is defined as the ratio of successive time steps and the suggested time step size (from the CFL condition). Based on recommendations from SIEMENS, a minimum change factor of zero and a maximum change factor of 1.1 is used for this case. In addition, a convective CFL condition is also enforced. This convective CFL condition, sets the physical

time step based on the CFL number, i.e., the convective time scale. The physical time step is adjusted in a way so that the actual CFL number approaches either the user-defined maximum CFL number or the user-defined mean CFL number, depending on whichever results in the minimum time step. The target mean and maximum CFL numbers are set to 50 and 100, respectively. It is important to note that the convective Courant number should be always less than one for explicit schemes, but can be more than one for implicit approach as in this case. Pseudo time-stepping is also enforced, i.e., iterations within each time step, with 15 inner-iterations within each time step. This is performed in order to converge and achieve a steady-state solution of the time-evolving governing equations. The CFL number defines the local time step and can be in the orders of 1000 s to speed up the flow solution which is one of the major advantages of using an implicit scheme [144]. Additionally, an mean monitor was applied to the flow domain in order to track the convective Courant number, which needs to be always less than one. In this case, the mean convective Courant number is found to be less than 0.7 at all times except for the initial transient, until 0.02 s (see Sec. 9.8).

9.3 Implicit Unsteady Flow Setup

Due to the nature of the problem, a transient simulation using STAR-CCM+ is desired. In this section, the specific configurations used to model the highly compressible and turbulent flow within the valve is described.

9.3.1 Initial Conditions

Initial conditions define the original values of the quantities in a the simulation. Appropriate initial conditions reduce the computational effort required to reach convergence as compared to poor initialization, especially in the case of a steady-state simulation. If there is a substantial difference in the initialization as compared to the converged solutions, it can cause divergence. This is because of the fact that

Table 9.2: Specified initial conditions for the transient problem.

Initial Condition	
Pressure	150 bar
Specific Dissipation Rate ($\hat{\omega}$)	1×10^{-4} s^{-1}
Static Temperature	372 K
Synthetic Turbulence Specification	None
Turbulence Specification	k + Omega
Specific Turbulent Kinetic Energy	0.001 J/kg
Velocity at the inlet	6.54 m/s

implicit schemes rely upon linearization techniques to advance the solution of equations toward convergence. One way to avoid convergence-related problem is by reducing the solution advancement by ramping up the Courant numbers and relaxation factors for the solvers [144]. Although not used in this case, often times a transient simulation can be initialized using the steady-state solution, as it reduces the chances of the specification of imperfect initial conditions, particularly when the physics of the problem is complex.

Moreover, each physics model in STAR-CCM+ requires information regarding the fundamental solution data to solve for the primary variables that are associated with the each models. For certain models such as turbulence schemes, one can specify the initial conditions in terms of turbulence intensity and viscosity ratio. Otherwise the turbulent kinetic energy and dissipation rate can be defined. The specified initial conditions used for the transient simulation have been defined in Table 9.2. The velocity field and temperature field initialization is from the specified operational velocity and temperature of the natural gas at the upstream inlet of the choke module, provided by Master Flo Valve (USA) Inc.

9.3.2 Boundary Conditions & Solver Specifications

As discussed in Section 8.3, the Dirichlet BCs are set at the inlet and outlet of the choke valve manifold. A pressure-outlet BC is set at both the valve upstream inlet and the downstream outlet and which is given in Table 9.3. The upstream inlet here

Table 9.3: Specified boundary conditions at the inlet and outlet of the choke valve.

Inlet Boundary Conditions	
Pressure	278.7 bar
Specific Dissipation Rate ($\hat{\omega}$)	1×10^{-4} s^{-1}
Static Temperature	372.15 K
Specific Turbulent Kinetic Energy	0.001 J/kg
Outlet Boundary Conditions	
Pressure	89.15 bar
Specific Dissipation Rate ($\hat{\omega}$)	1×10^{-4} s^{-1}
Static Temperature	372.15 K
Specific Turbulent Kinetic Energy	0.001 J/kg

Table 9.4: Solver Configurations.

AMG Linear solver specifications	
Max. cycles	30
Cycle type	V cycle
$\hat{k} - \hat{\omega}$ turbulence	
Under relaxation factor (URF)	0.75
Cycle type for the AMG solver	Flex cycle

represents the inflow of the compressed natural gas into the choke valve manifold, and should not be confused with the port inlets on the nozzle as shown in Fig. 6.1. The Reynolds number [1] at the upstream inlet is about 19.25 million at the given choking condition of 32% of the C_v. The modified solver and physics model configurations have been described in Tables 9.4 and 9.5. All the other system-specified values have been kept the same to the values specified by STAR-CCM+ v.2019.2.1. Detailed DDES SST $\hat{k} - \hat{\omega}$ model coefficient values are provided in Appendix B.2.2.

9.4 Transient Flow Results

The transient simulation is run for a total physical time of 0.12 s. The simulation has been run on the Sabine Cluster at the Research Computing Data Core (RCDC) of the University of Houston. The computing has been parallelized using 6 nodes

[1] The Reynolds number at the inlet is defined by, $Re_{inlet} = \hat{V}_g \hat{D}_{Inlet}/\hat{\nu}$.

Table 9.5: Physics model configurations.

Coupled Flow	
Upwind Blending Factor for BD	0.9
Secondary gradients	Enabled
Coupled Inviscid Flux	Roe FDS
SST $\hat{k}-\hat{\omega}$ DES	
Reliazibility option	Durbin Scale Limiter
Convection	2^{nd} order
Constitutive option	Linear
Formulation option	DDES

with 28 tasks per node. The total computing time was approximately 408 hours with the specified parallel configuration. The results are summarized through three sections. The Mach, pressure and temperature profiles are discussed in detail in sections 9.4.1, 9.4.2 and 9.4.3, respectively. The mean Mach number, pressure and temperature contours are represented in the planes of interest, i.e., plane A, B, and, C described in Figs. 9.2-9.7. The three considered planes are all orthogonal to each other, i.e., y-z plane (Plane A), x-z plane (Plane B), and y-x plane (Plane C). Finally the post processing, i.e., FFT, results from the monitors at the probe locations and is discussed in section 9.4.4. The pressure ratio, P_r, and temperature ratio, T_r, have been defined using the upstream inlet pressure and temperature scales, i.e., $T_r = 1$, represents a temperature of 372.15 K and, $P_r = 1$, defines a pressure of 278.7 bar.

9.4.1 Mach Number Profiles

The Mach number profiles are used to describe the flow regime across planes A and B. The highest instantaneous Mach number at 0.12 s is of 1.78 (not shown here for brevity) and occurs within the large structures shed from the two highly underexpanded jet interactions. These two highly underexpanded jets interact with each head on which can be visualized in Fig. 9.2c. The jets go eventually dissipate each other's energy across the jet interaction plane shown in Fig. 9.3. Also it is interesting to note that, although jets look fairly symmetrical across planes A and B in Figs. 9.2a

and b, plane C shows a unsymmetrical Mach number profile in Fig. 9.2c. It should also be noticed that the higher mach region ($M \approx$ 0.781) in Fig. 9.2c, which is towards the left of the two highly underexpanded jets when looked along plane C, i.e., head on from the smaller port on the right in Fig. 9.2a. Furthermore, the jet interaction plane in Fig. 9.3, i.e, plane C in Fig. 9.2c, has a mean mach number of less than one across the whole flow domain. This fact can be verified by observing Fig. 9.2c. In addition to that, the energy dissipation of the two jets through interaction occurs at about $M > 0.5$, with the bias as explained before. The higher mean gas velocity bias can be a precursor to generate oscillatory behaviour of the flow field through the whole flow domain of the valve. Subsequently the jet slicing phenomena that will occur about plane C, would generate a stronger structure being shed. Hence, this phenomena will lead to be one of the possible sources of the dominant vibration modes observed within the flow.

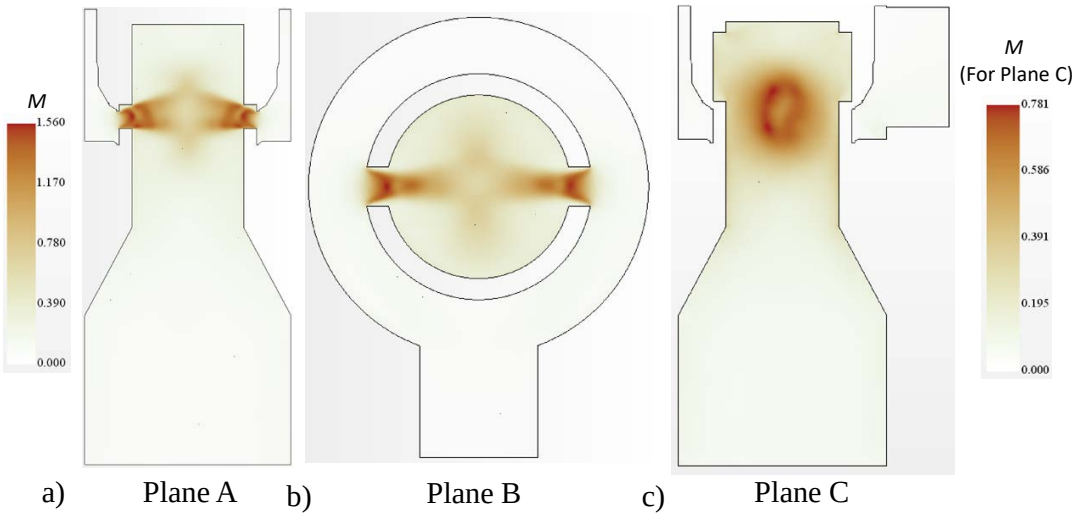

Figure 9.2: Mean Mach number contours at $\hat{t} = 0.12$ s across the three planes of interest A, B and C.

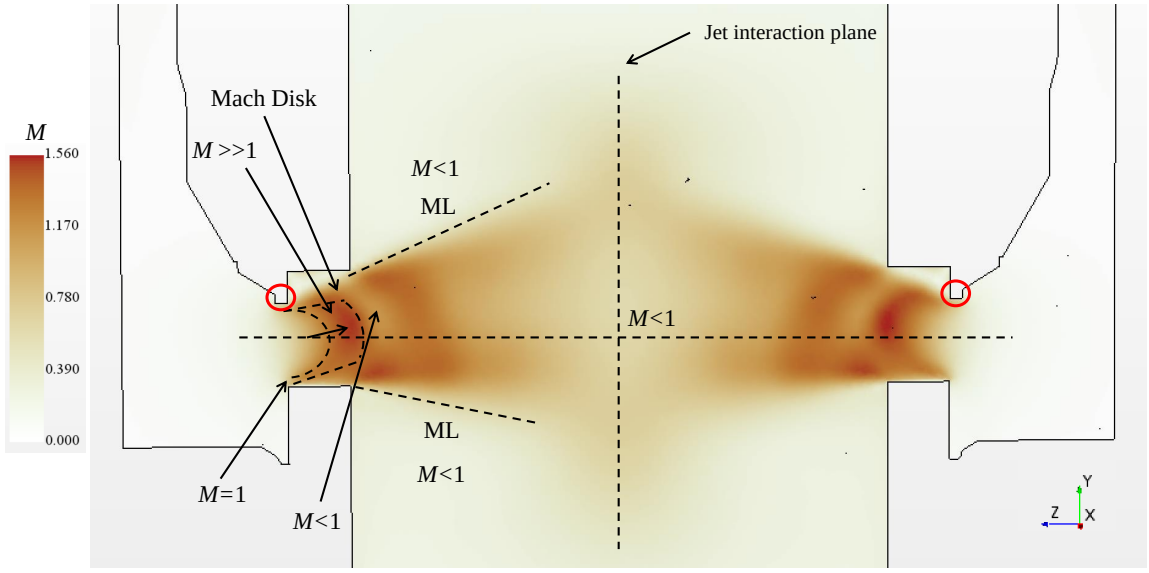

Figure 9.3: Schematic representation of the mean Mach number profile of the highly underexpanded jets as seen through plane A, at $\hat{t} = 0.12$ s. Symbols, dashed lines and markers are explained in details within the text.

As explained in Sec. 7.1, the highly underexpanded jet structure is represented in this case, based on the study by Franquet *et al.* [115] in Fig. 9.3. The mean Mach profile is able capture the barrel-shape shock and the MD formation (the first MD in the mean profile is shown in Fig. 9.3). Although a fully developed shock diamond cannot be observed, it can be noticed that the area ahead of the MD has a Mach number less than one. The region behind the MD has considerably higher Mach numbers ($M > 1.3$). The transition between these two regions is accompanied by the MD, which appears due to a singular reflection within jet [115]. The jet boundary can be observed in Fig. 9.3, through the mixing layer (ML). In the outer regions of the ML the Mach numbers are always less than one as expected from the definition of a highly highly underexpanded jet. Based on the description provided about underexpanded methane jets, in Sec. 7.1, mixing does not occur before the MD. This results in a strong Mach number region ($M > 1.4$) right until the MD as seen in this case in Fig. 9.3 [127]. As explained by Hamzehloo *et al.* [127], the high penetration of the jets is due of the lack of turbulent fluctuations right after the nozzle-exit. Consequently, less amounts of

vortices get initiated before the MD [128]. Subsequently, primary mixing is observed to occur only after the MD and nearabout regions at the jet boundaries as seen in Fig. 9.5a. This is because of the large-scale turbulence at these regions [127].

Moreover, the oblique orientation of both the highly underexpanded jets in Fig. 9.3 can be observed. Right after the entrance, the jet exits the valve-nozzle with a Mach number of one but tilted upwards, above the dotted horizontal line shown in Fig. 9.3. The observed obliqueness comes from the partial closing (from the valve sleeve at 32% of maximum C_v) of the smaller ports on the valve-nozzle (marked with red circle in Fig. 9.3). This causes the jets to expand upwards as compared to the bottom half. Consequently acting as a perturbator, eventually giving rise to instantaneous oscillatory behaviour of the flow field. The dissipation of these oscillatory-velocity fields generated at the nozzle-exit and at the jet interaction plane will occur at the valve-nozzle walls. This will lead to possibly large-oscillatory stresses at the wall, especially at lower frequency regions (explained in detail in Sec. 9.4.4).

9.4.2 Pressure Profiles

The mean P_r profiles are shown in Fig. 9.4. Its observed that the compressed methane gas from the upstream inlet is unable to expand within the jets from the two smaller ports. This is an expected phenomenon in the case of high underexpansion. Although, eventually the pressure reduces downstream of the valve to correspond to the outlet pressure of 89.15 bar, i.e., $P_r \approx$ 0.32. In Fig. 9.4 the sudden pressure drop from the inlet of the valve-nozzle ports, to a pressure of $\approx$ 0.4 times of it is observed around the trim region. Giving rise to power losses of $\approx$ 2.91 MW (see Sec. 7.3). This adverse pressure drop can give rise to possible erosion wear near the valve-trim regions, making the valve-nozzle vulnerable as compared to the other parts of the choke valve [153]. The oblique jets are surrounded by high pressure zone circumscribing the ML with a $P_r \approx$ 1.09 and can be observed in Figs. 9.4a and b. Based on the description provided by Franquet *et al.* [115], in Fig. 9.4b, this zone

of $P_r \approx$ 1.09 can be described by the nearfield zone (see Fig.9 in [115]). The high pressure region diminishes and reduction in pressure occurs outside the transition zone within the underexpanded jet boundary [115]. Furthermore, in part c of Fig. 9.4, the imprint of the bias in the Mach numbers can be seen but is comparatively subtle in terms of the P_r values.

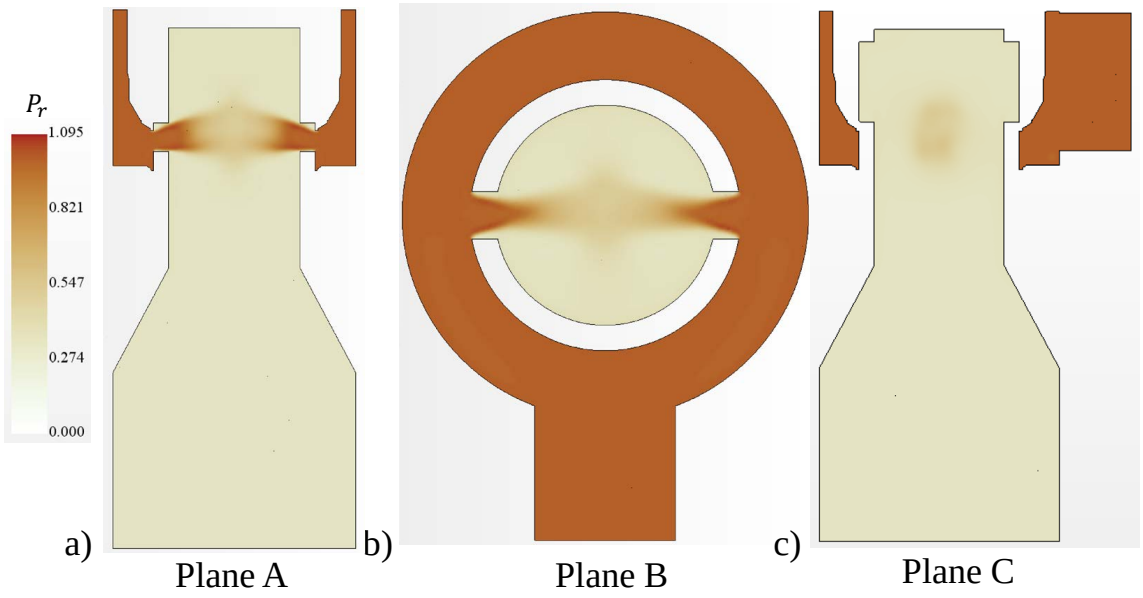

Figure 9.4: Mean P_r contours over at $\hat{t} = 0.12$ s across a) plane A, b) plane B, and c) plane C.

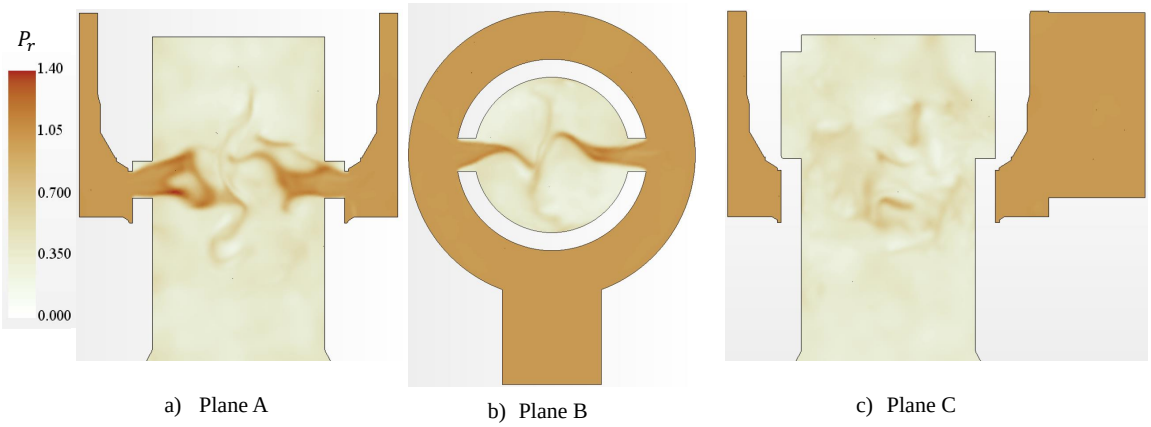

Figure 9.5: Elnarged representation of instantaneous P_r contours at $\hat{t} = 0.12$ s across plane A, B, and C.

The instantaneous P_r profiles for the three planes are shown in Fig. 9.5. In part a and b, the jet interaction causes shedding of structures, with high pressure ratios ($P_r > 0.5$). But it is noteworthy, that in Fig. 9.5a, the shed structures orthogonal to plane A, dissipate before reaching the valve head. Moreover, in Fig. 9.5b, the underexpanded jets can be observed to be surrounded by high pressure regions, i.e., $P_r \approx 1$. These two jets collide and shed two large scale ($\approx$ 0.0508 m, i.e.,inner radius of the valve-nozzle) structures, which get dissipated at the walls. This visualization can be used to extrapolate the physics of these high-pressure oscillatory structures. These structures would eventually dissipate and endure stresses at the nozzle walls. Also it is worth noting that the large structures have an orthogonality relative to the underexpanded jets from the two ports on the nozzle. Hence, making the structure gain fatigue over time at these diametrically opposite zones on the inner wall of the nozzle body. Over time the oblique underexpanded jets will swing back and forth (oscillating) and consequently the shedding will also reverse. This can easily induce even greater cyclic stresses which can cause failure at this diametrically opposite positions. Finally, a lot of pressure pulsations ($P_r > 0.5$) can be observed from the instantaneous P_r profiles on the jet interaction plane in Fig. 9.5c. Since this turbulent mixing is self dissipative in nature, explains the Mach numbers being lower than one in this plane. Therefore, dissipation of these high pressure pulsations accompanied with the velocity oscillations can couple up at the walls, which goes onto account for the existence of dominant vibration modes.

9.4.3 Temperature Profiles

As described in Sec. 7.1, when a fluid flows through the valve-nozzle ports, the pressure of the fluid drops adiabatically (due to expansion) and is commonly known as the JT effect. Hence, the underexpansion pressure-temperature correlation of the supersonic jets can be explained by the JT coefficient (see Eq. 7.14). The JT coefficient can either be negative or positive for a real gas (zero for an ideal gas). Moreover, if

the gas is below the inversion temperature (for methane its 400 K [154]), $\hat{\mu}_J > 0$ and the gas always cools down. Based on the study performed by Ernst *et al.* [155], $\hat{\mu}_J$ is approximately greater than 0.677 ± 0.010 at 300 bar and $\approx$ 370 K. Hence this goes onto explain for the reduction in temperature as observed in the T_r profiles across the expanded flow domain in Fig. 9.7. It can be noticed that the mean temperature profile across the upstream ($T_r \approx$ 1 in Figs. 9.7a and c) before the flow expands through the nozzle-exit ports.

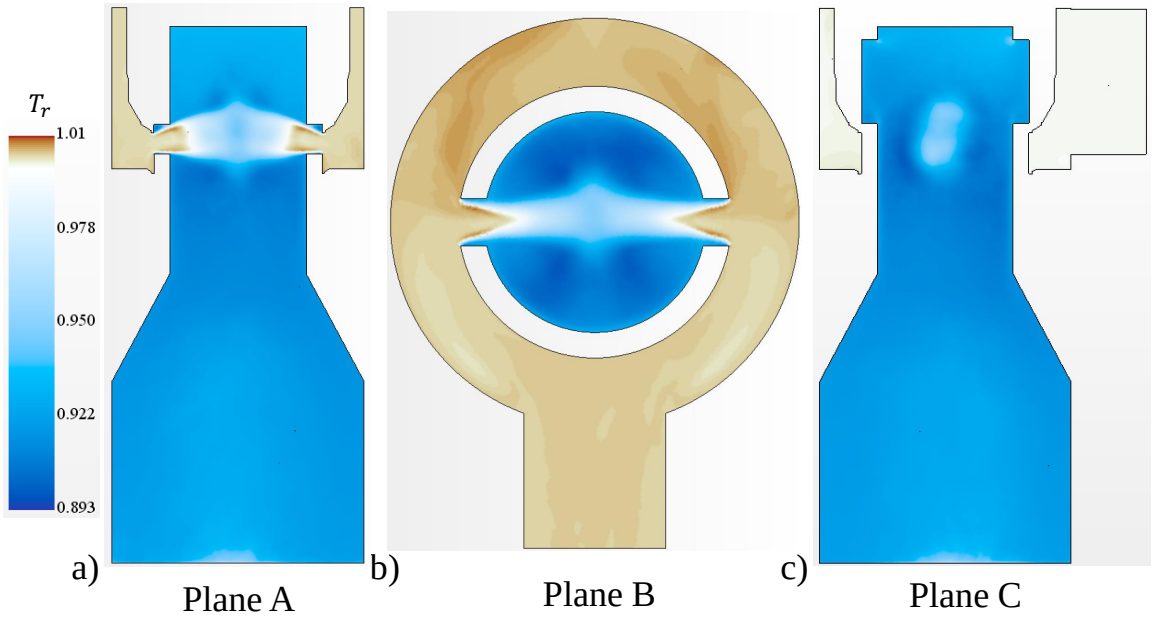

Figure 9.6: Mean temperature contours over at $\hat{t} = 0.12$ 0.12 s across planes a) A, b) B, and c) C. Here, $T_r = 1$, i.e., ambient temperature at inlet and outlet, is set to pure white color for better visualization.

Eventually, the highly underexpanded jets with $T_r \approx$ 1.005 eventually cool down to $T_r \approx$ 0.925 (see Fig. 9.7) once the jets dissipate each other out. The JT cooling extends to the downstream and throughout the valve head. Observing the $T_r \approx$ 1 profiles across the highly underexpanded jet regions in Fig. 9.7a is surrounded by $T_r > 1$. Outside the jet ML boundary (see Fig. 9.3) in Figs. 9.7a and b, the cooling intensifies ($P_r < 0.93$) as the gas expands. Plane C in Fig. 9.7 adds to the evidence of a bias forming over time.

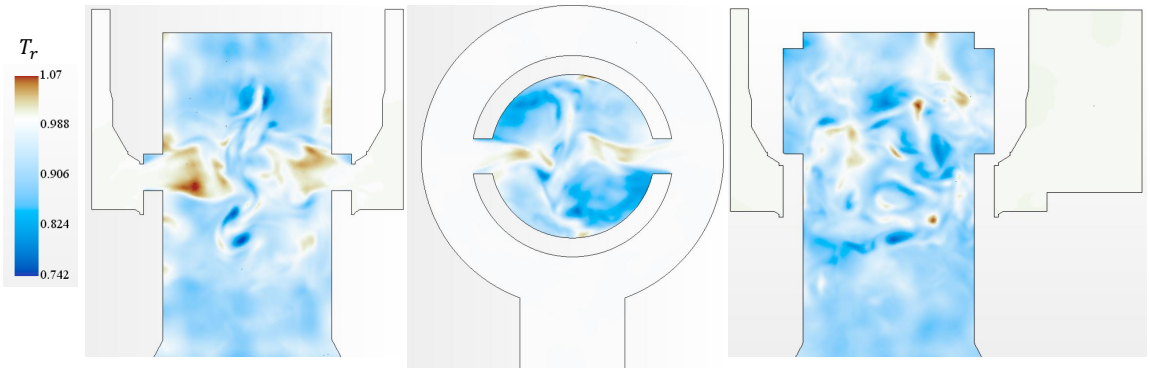

Figure 9.7: Enlarged depiction of instantaneous T_r contours at $\hat{t} = 0.12$ s across plane A, B, and C. Similar to Fig. 9.7, $T_r = 1$ is set to pure white color.

The transport of the colder temperature can be understood by evaluation of the instantaneous T_r profiles in Fig. 9.4.3. The cooled-temperature oscillations occur about the the jet interaction plane, which can be visualized through Fig. 9.4.3a and b. These cooling pulsations ($T_r \approx$ 0.742, i.e., 276 K in plane C) eventually reach the valve head and are flushed downstream of the valve. This phenomena eventually gives rise to the mean $T_r \approx$ 0.93 across the flow domain as represented by the mean P_r profiles. Further visualization of jet interaction plane, i.e., plane C, in Fig. 9.4.3c, large amounts of non-homogeneous distribution of T_r can be observed. It is noticed, that smaller zones of $T_r > 1$ are spread throughout plane C and can add to the pressure oscillations at the interior walls of the valve-nozzle. A similar observation can be made about the colder temperatures at the walls. Although, the colder temperatures are not significant enough but can be considerable over time. As the lower temperatures at the tugsten carbide (WC) nozzle walls can cause the material to become more brittle in nature. This can escalate the failure process. Although, JT effect acts as an advantage for cryogenic gas production, it can also be avoided to a certain extent by preheating the gas before it enters the pressure reduction mechanism.

9.4.4 Frequency Analysis

To measure the transient pressure oscillations at the inner nozzle wall, four probes are installed on the nozzle wall, i.e., probe 1, 2, 3, and 4. It should be noted that Probe 1/Probe3 and Probe 2/Probe4 are diametrically apart by 0.102 m. Four monitors are defined with one at each probe. It should be noted probe 1 and 2 are located upstream on the y-x plane, and the other two being on the y-z plane downstream of the two smaller ports. Finally, a FFT is performed to extract the frequency spectrum of the pressure oscillations at the four probes using a point time Fourier transform from the available data set functions within STAR-CCM+.

Since the flow within the valve is sensitively time dependent, i.e., the statistical properties of the flow vary over time. Therefore, in order to asses for stationarity of such a transient/stochastic process, i.e., the statistical properties of the fluid-flow (in this case) do not change over time, covariance is performed. This analysis has been performed to filter out major transient nature that occurs during the initialzation of the problem. The covariance of the velocities in the x,y and z direction are probed at a point in the center of plane B. The results are plotted in Fig. 9.8. Essentially, the covariance measures the joint variability of two velocities at a time instant, i.e., $\hat{u}_x - \hat{u}_y$, $\hat{u}_y - \hat{u}_z$ and $\hat{u}_z - \hat{u}_x$, over the time of 0.12 s. It is observed that initially higher variability exists until 0.02 s. Although, 0.02 s is succeeded by comparatively smaller joint variability which is desirable, it still does not signify any weak/strong statistical stationarity. The transient pressure oscillations at the four points are presented in Fig. 9.9. It can be noted that there is an overall instantaneous pressure bias towards the right of plane A, B and C. which can be observed in Fig. 9.9a and c as compared to parts b and d. This can be observed from the amplitudes of pressure oscillation at probes 2 and 4 which are less as compared to the amplitude of the oscillatory behaviour observed at probes 1 and 3. Such phenomena can be caused due to unsymmetrical energy dissipation from the swaying of the underexpanded jets after interaction across

plane C. It is quite possible, the large structures that are being shed dissipates strongly towards the right side of plane A, B and C.

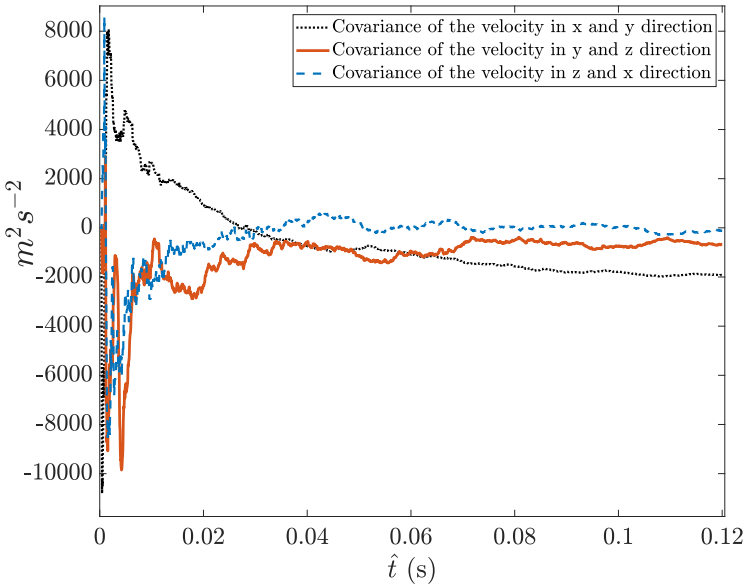

Figure 9.8: Covariance plots of the velocities probed at the center of plane B.

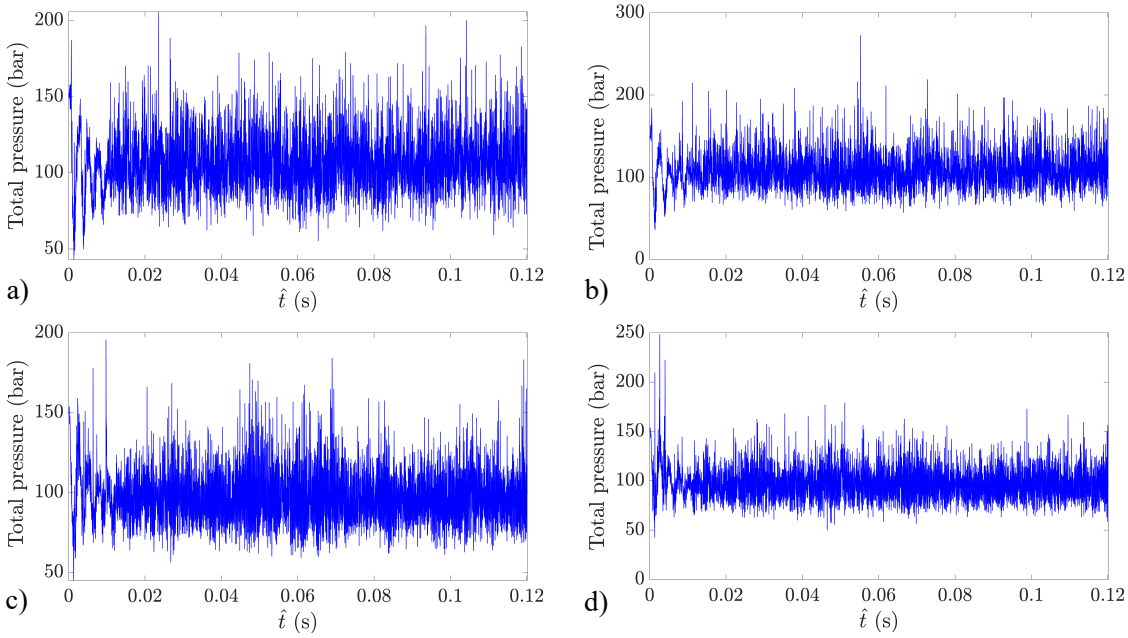

Figure 9.9: The pressure variations recorded for at $\hat{t} = 0.12$ s at probes 1-4 shown in parts a-d respectively.

The transient pressure signals are imported into point time Fourier transform function within STAR-CCM+ to perform the FFT processing [144]. Additionally, a Hann window function with an overlap factor of 0.5 to ascertain periodicity is applied. Moreover, an initial transient nature exists in the pressure oscillations. Therefore, the intial 0.02 s of the measured pressure signals are not considered. The FFT results are shown in Fig. 9.10. The power spectral density (PSD) plots show the existence of dominant frequency modes at 4500 to 5000 Hz and at 9500 to 10000 Hz, with the most dominant mode occurring at around 4600 Hz. Interestingly, the theoretical peak frequency of the broadband frequency spectrum calculated from Eq. 7.35 be around 4660 Hz. The insets in Fig. 9.10 are the FFT of the transient pressure signals upto 0.06 s. Over time the dominant frequency modes around 5000 Hz, govern all the localized dissipation of the oscillatory pressure across the four probes.

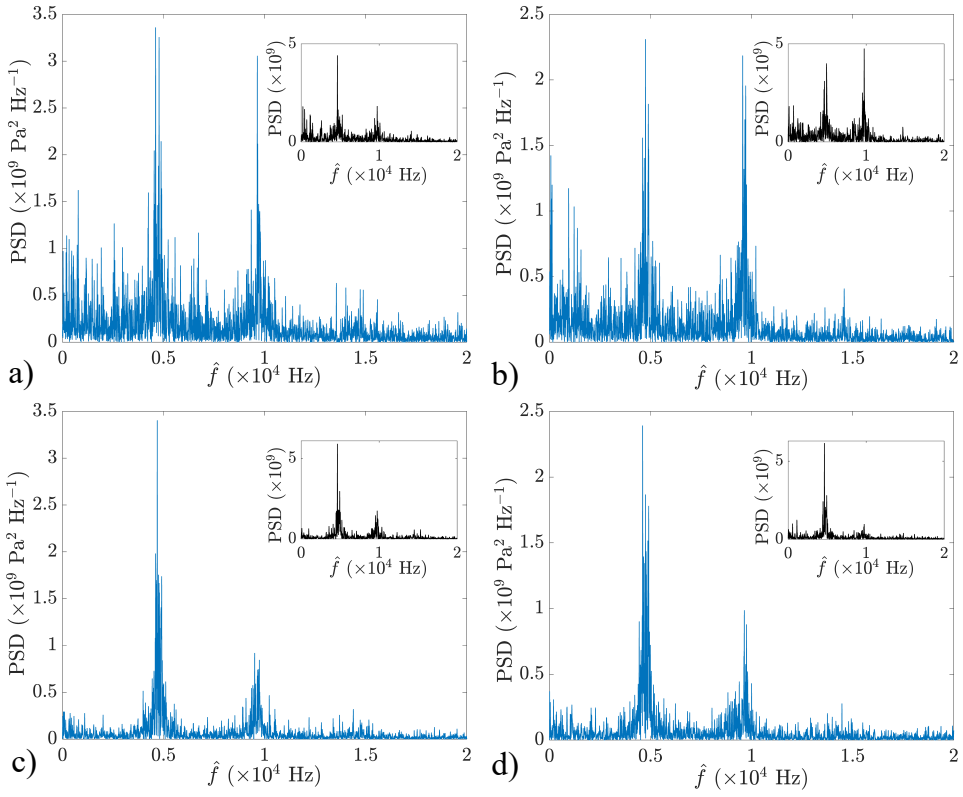

Figure 9.10: FFT of the pressure oscillations from 0.02 to 0.12 s of physical time at probes 1-4 (parts a-d respectively). The insets are the FFT of the transient pressure upto 0.06 s.

Moreover, the dissipation takes place in a more consistent manner (in both cases of 0.06 and 0.12 s) about 5000 Hz as compared to its higher dominant mode counterpart, i.e., $\approx$ 10000 Hz. This is because, the pressure oscillations at 5000 Hz are stronger as compared to the ones at 10000 Hz and hence the latter's PSD diminish downstream, i.e., probe 3 and 4. Consequently, this also bolsters the fact that the observed dominant modes exist throughout the flow over time, i.e. time independent. The existence of these two dominant frequency modes at the wall arises from the two large structures that are being shed (see Fig. 9.5b). Moreover, by the time the pressure oscillations accompanied by these two large-scale structures reach the valve-nozzle wall, they have dissipated to a certain extent. The dissipated structures give rise to low-pressure and high-frequency pressure oscillations, which go onto collide with the valve walls. Subsequently over time these high-frequency pressure oscillations incur large amounts of cyclic stresses in localized regions on the wall. This can weaken the nozzle material at these strained regions and over time induce hoop stress within the cylindrical structure of the valve-nozzle.

Furthermore, in the study performed by Yonezawa *et al.* [91], the amplitude of the peak frequencies hold little importance because of the broadband nature of turbulence itself. In other words, the eigenfrequencies can be matched and the generated oscillations can be scaled asymptotically into the structure at these resonant frequencies even if the frequencies generated from the flow are non-dominant as compared to the peak frequency, $\hat{f}_p$. Again, it can be noticed that in the two downstream probes 3 and 4, i.e., Fig. 9.10c and d, the low amplitude frequency modes have reduced in terms of their PSD values which is expected because of dissipation downstream. Interestingly, a ring test has been performed by Master Flo Valve (USA) Inc., on the four port nozzle to evaluate the eigenfrequencies of the system. For this extraction of resonant frequencies, an FFT is carried out on the acoustic response to an forced excitation (within the audible range) and peaks are observed at 2800 Hz and 7600 Hz, with the

former being the most dominant. Although, it has to be kept in mind, frequencies in the nearabout regions of the observed resonant modes that can amplify the vibrations transmitted into the valve-nozzle which can lead to failure (see insets of Fig. 9.10). Although, the resonant frequencies found out for the nozzle using this test can be different from the well head assembly at its subsea operating conditions. So, the reliability of the valve can still be questioned because of the lack of information on the damping factor of the combined system and the eigenfrequencies of the P5E assembly.

10. Summary & Outlook

FIV is one of the most well-known phenomenons that can compromise structure's reliability but still can go unnoticed at times. Despite its well-known existence, especially as shown in studies performed in the available literature in context to piping systems, it is generally not used to investigate possible choke valve manifold failures. The purpose of this purely numerical study is to show how because of the turbulent nature of the flow within such choke systems, broadband frequencies are generated with the possible existence of dominant modes, as in this case. Although, the dominant modes are accompanied around the peak frequency of 4600 Hz, other frequency modes exist at comparable PSDs which can excite the eigenfrequencies of the system and cause a resonance in a purely undamped system.

The two ways to avoid such a failure from FIV are introduction of materials which are more suitable and have a more appropriate damping factor. The second possible way to is to modify the valve design accordingly to diminish the existence of dominant modes of vibration. However, the former requires an eigenmode analysis of the structural system and matching of the stresses with their respective vibration modes. Such detailed information about the the material can be absent in this regards, a crude assumption can be made that the damping ratio is the same across all the frequency modes [106]. In this study, the resonant frequencies found out for the nozzle using a simplified ring test can be different for the whole subsea well head assembly as mentioned before. This fact asks for better way to approximate or empirically calculate the possible eigenfrequencies of the P5E assembly as it is impossible to measure the eigenfrequencies in its regular subsea operation condition. The second approach suggested from this study is a way to utilize the numerical results to modify the designed prototypes. Such as introducing more ports in order to increase turbulent

mixing. This process of checking for the existence of dominant modes and consequently calculated modifications can be brought until the dominant modes are diminished. This can save a lot of time and money at both the manufacturer's and user's end. The design can be modified accordingly from the feedback received from the vibrational study. Although, it should also be kept in mind the computational overhead that comes with such complex fluid flows. Based on the above two approach, the P5E valve can be modified, in order to avoid induction of hoop stress within the nozzle body, design modifications can be brought in. Specifically, more ports can be included in order to distort the large scale structures that are being shed. But this has to be done in a calculated approach until it is ascertain that the dominant modes get diminished.

Bibliography

[1] S. E. Spagnolie. "Complex fluids in biological systems". *Biological and Medical Physics, Biomedical Engineering* (2015).

[2] R. H. Ewoldt, M. T. Johnston, and L. M. Caretta. "Experimental challenges of shear rheology: how to avoid bad data" (2015), 207–241.

[3] E. W. Merrill, E. R. Gilliland, G. Cokelet, H. Shin, A. Britten, and R. E. Wells Jr. "Rheology of human blood, near and at zero flow: effects of temperature and hematocrit level". *Biophysical Journal* 3.3 (1963), 199–213.

[4] E. W. Errill. "Rheology of blood". *Physiol. Rev.* 49.4 (1969), 863–888.

[5] O. K. Baskurt and H. J. Meiselman. "Blood rheology and hemodynamics". In: *Semin. Thromb. Hemost.* Vol. 29. 05. Copyright© by Thieme Medical Publishers, Inc., 333 Seventh Avenue, NY, USA. 2003, 435–450.

[6] A. Z. Valant, L. Žiberna, Y. Papaharilaou, A. Anayiotos, and G. C. Georgiou. "The influence of temperature on rheological properties of blood mixtures with different volume expanders—implications in numerical arterial hemodynamics simulations". *Rheologica Acta* 50.4 (2011), 389–402.

[7] M. M. Alves, C. Rocha, and M. P. Gonçalves. "Study of the rheological behaviour of human blood using a controlled stress rheometer". *Clin. Hemorheol. Microcirc.* 53.4 (2013), 369–386.

[8] P. C. Sousa, J. Carneiro, R. Vaz, A. Cerejo, F. T. Pinho, M. A. Alves, and M. S. N. Oliveira. "Shear viscosity and nonlinear behavior of whole blood under large amplitude oscillatory shear." eng. *Biorheology* 50.5-6 (2013), 269–282. ISSN: 1878-5034.

[9] L. Campo-Deaño, R. P. A. Dullens, D. G. A. L. Aarts, F. T. Pinho, and M. S. N. Oliveira. "Viscoelasticity of blood and viscoelastic blood analogues for use in polydymethylsiloxane in vitro models of the circulatory system". *Biomicrofluidics* 7.3 (2013), 034102.

[10] J. S. Horner, M. J. Armstrong, N. J. Wagner, and A. N. Beris. "Measurements of human blood viscoelasticity and thixotropy under steady and transient shear and constitutive modeling thereof". *Journal of Rheology* 63.5 (2019), 799–813.

[11] J. S. Horner, M. J. Armstrong, N. J. Wagner, and A. N. Beris. "Investigation of blood rheology under steady and unidirectional large amplitude oscillatory shear". *Journal of Rheology* 62.2 (2018), 577–591.

[12] G. B. Thurston. "Viscoelasticity of human blood". *Biophysical journal* 12.9 (1972), 1205–1217.

[13] A. J. Apostolidis, M. J. Armstrong, and A. N. Beris. "Modeling of human blood rheology in transient shear flows". *Journal of Rheology* 59.1 (2015), 275–298.

[14] M. Armstrong, J. Horner, M. Clark, M. Deegan, T. Hill, C. Keith, and L. Mooradian. "Evaluating rheological models for human blood using steady state, transient, and oscillatory shear predictions". *Rheologica Acta* 57.11 (2018), 705–728.

[15] I. Andia and N. Maffulli. "Platelet-rich plasma for managing pain and inflammation in osteoarthritis". *Nat. Rev. Rheumatol.* 9.12 (2013), 721–730.

[16] B. J. Cole, S. T. Seroyer, G. Filardo, S. Bajaj, and L. A. Fortier. "Platelet-rich plasma: where are we now and where are we going?" *Sports health* 2.3 (2010), 203–210.

[17] A. Mishra, K. Harmon, J. Woodall, and A. Vieira. "Sports medicine applications of platelet rich plasma". *Curr. Pharm. Biotechnol.* 13.7 (2012), 1185–1195.

[18] L. G. Glynn, A. Mustafa, M. Casey, J. Krawczyk, J. Blom, R. Galvin, A. Hannigan, C. P. Dunne, A. W. Murphy, and C. Mallen. "Platelet-rich plasma (PRP) therapy for knee arthritis: a feasibility study in primary care". *Pilot and feasibility studies* 4.1 (2018), 93.

[19] G. Malanga and P. Jayaram. "Need for proper classification of PRP: letter to the editor". *Am. J. Sports Med.* 45.6 (2017), NP23–NP24.

[20] P. Jayaram, P. C. Yeh, and J. Cianca. "Platelet-rich plasma protocols can potentiate vascular emboli: Contraindications to platelet-rich plasma". *J. Int. Soc. Phys. Rehabil. Med.* 2.3 (2019), 103.

[21] F. Russo, M. D'Este, G. Vadalà, C. Cattani, R. Papalia, M. Alini, and V. Denaro. "Platelet rich plasma and hyaluronic acid blend for the treatment of osteoarthritis: Rheological and biological evaluation". *PloS one* 11.6 (2016), e0157048.

[22] G. Vadalà, F. Russo, M. Musumeci, M. D'Este, C. Cattani, G. Catanzaro, M.C. Tirindelli, L. Lazzari, M. Alini, and R. Giordano. "Clinically relevant hydrogel-based on hyaluronic acid and platelet rich plasma as a carrier for mesenchymal stem cells: Rheological and biological characterization". *J. Orthop. Res.* 35.10 (2017), 2109–2116.

[23] Y. Kobayashi, A. Okamoto, and K. Nishinari. "Viscoelasticity of hyaluronic acid with different molecular weights". *Biorheology* 31.3 (1994), 235–244.

[24] J. C. Caygill and G. H. West. "The rheological behaviour of synovial fluid and its possible relation to joint lubrication". *Medical and biological engineering* 7.5 (1969), 507–516.

[25] R. H. Ewoldt, A. E. Hosoi, and G. H. McKinley. "Nonlinear viscoelastic biomaterials: meaningful characterization and engineering inspiration". *Integrative and comparative biology* 49.1 (2009), 40–50.

[26] R. H. Ewoldt, G. H. McKinley, and A. E. Hosoi. "Fingerprinting soft materials: A framework for characterizing nonlinear viscoelasticity". *arXiv preprint arXiv:0710.5509* (2007).

[27] C. Saengow, A. J. Giacomin, and A. S. Dimitrov. "Unidirectional large-amplitude oscillatory shear flow of human blood". *Physics of Fluids* 31.11 (2019), 111–903.

[28] K. Hyun, J. G. Nam, M. Wilhelm, K. H. Ahn, and S. J. Lee. "Nonlinear response of complex fluids under LAOS (large amplitude oscillatory shear) flow". *Korea-Australia Rheology Journal* 15.2 (2003), 97–105.

[29] S. O'Callaghan, M. Walsh, and T. McGloughlin. "Numerical modelling of Newtonian and non-Newtonian representation of blood in a distal end-to-side vascular bypass graft anastomosis". *Medical engineering & physics* 28.1 (2006), 70–74.

[30] M. Bureau, J. C. Healy, D. Bourgoin, and M. Joly. "Rheological hysteresis of blood at low shear rate". *Biorheology* 17.1-2 (1980), 191–203.

[31] S-H. Yun, E-H. Sim, R-Y. Goh, J-I. Park, and J-Y. Han. "Platelet activation: the mechanisms and potential biomarkers". *BioMed research international* 2016 (2016).

[32] B. Estevez and X. Du. "New concepts and mechanisms of platelet activation signaling". *Physiology* 32.2 (2017), 162–177.

[33] C. Storm, J. J. Pastore, F. C. MacKintosh, T. C. Lubensky, and P. A. Janmey. "Nonlinear elasticity in biological gels". *Nature* 435.7039 (2005), 191–194.

[34] P. Jayaram, P. Yeh, S. J. Patel, R. Cela, T. B. Shybut, M. W. Grol, and B. H. Lee. "Effects of Aspirin on Growth Factor Release From Freshly Isolated Leukocyte-Rich Platelet-Rich Plasma in Healthy Men: A Prospective Fixed-

Sequence Controlled Laboratory Study". *Am. J. Sports Med.* 47.5 (2019), 1223–1229.

[35] H. J. Braun, H. J. Kim, C. R. Chu, and J. L. Dragoo. "The effect of platelet-rich plasma formulations and blood products on human synoviocytes: implications for intra-articular injury and therapy". *The American journal of sports medicine* 42.5 (2014), 1204–1210.

[36] J. Fitzpatrick, M. K. Bulsara, P. R. McCrory, M. D. Richardson, and M. H. Zheng. "Analysis of platelet-rich plasma extraction: variations in platelet and blood components between 4 common commercial kits". *Orthopaedic journal of sports medicine* 5.1 (2017), 2325967116675272.

[37] R. Yan, Y. Gu, J. Ran, Y. Hu, Z. Zheng, . Zeng, B. C. Heng, X. Chen, Z. Yin, and W. Chen. "Intratendon delivery of leukocyte-poor platelet-rich plasma improves healing compared with leukocyte-rich platelet-rich plasma in a rabbit Achilles tendinopathy model". *The American journal of sports medicine* 45.8 (2017), 1909–1920.

[38] W. R. Parrish, B. Roides, J. Hwang, M. Mafilios, B. Story, and S. Bhattacharyya. "Normal platelet function in platelet concentrates requires non-platelet cells: a comparative in vitro evaluation of leucocyte-rich (type 1a) and leucocyte-poor (type 3b) platelet concentrates". *BMJ open sport & exercise medicine* 2.1 (2016).

[39] J. C. Riboh, B. M. Saltzman, A. B. Yanke, L. Fortier, and B. J. Cole. "Effect of leukocyte concentration on the efficacy of platelet-rich plasma in the treatment of knee osteoarthritis". *The American journal of sports medicine* 44.3 (2016), 792–800.

[40] D. Mazzucco, G. McKinley, R. D. Scott, and M. Spector. "Rheology of joint fluid in total knee arthroplasty patients". *Journal of Orthopaedic Research* 20.6 (2002), 1157–1163.

[41] P. Bhuanantanondh. "Rheology of synovial fluid with and without viscosupplements in patients with osteoarthritis: a pilot study". PhD thesis. University of British Columbia, 2009.

[42] P. Bhuanantanondh, D. Grecov, and E. Kwok. "Rheological study of viscosupplements and synovial fluid in patients with osteoarthritis". *CMBES Proceedings* 33 (2010).

[43] S. D. Masouros, A. M. J. Bull, and A. A. Amis. "(i) Biomechanics of the knee joint". *Orthopaedics and Trauma* 24.2 (2010), 84–91.

[44] M. Petrtyl, J. Lisal, and J. Danesova. "Biomechanical properties of synovial fluid in/between peripheral zones of articular cartilage". *Biomaterials-Physics and Chemistry* (2006), 490.

[45] C. Picart, J-M. Piau, H. Galliard, and P. Carpentier. "Human blood shear yield stress and its hematocrit dependence". *Journal of Rheology* 42.1 (1998), 1–12.

[46] D. R. Bland. *The theory of linear viscoelasticity*. Courier Dover Publications, 2016.

[47] S. A. Rogers. "In search of physical meaning: Defining transient parameters for nonlinear viscoelasticity". *Rheologica Acta* 56.5 (2017), 501–525.

[48] G. Tomaiuolo, A. Carciati, S. Caserta, and S. Guido. "Blood linear viscoelasticity by small amplitude oscillatory flow". *Rheologica Acta* 55.6 (2016), 485–495.

[49] K. Hyun, M. Wilhelm, C. O. Klein, K. S. Cho, J. G. Nam, K. H. Ahn, S. J. Lee, R. H. Ewoldt, and G. H. McKinley. "A review of nonlinear oscillatory shear tests: Analysis and application of large amplitude oscillatory shear (LAOS)". *Progress in Polymer Science* 36.12 (2011), 1697–1753.

[50] N. W. Tschoegl. *The phenomenological theory of linear viscoelastic behavior: an introduction*. Springer Science & Business Media, 2012.

[51] P. K. Singh, J. M. Soulages, and R. H. Ewoldt. "Frequency-sweep medium-amplitude oscillatory shear (MAOS)". *Journal of Rheology* 62.1 (2018), 277–293.

[52] R. H. Ewoldt. "Predictions for the northern coast of the shear rheology map: XXLAOS". *Journal of Fluid Mechanics* 798 (2016), 1–4.

[53] R. H. Ewoldt, A. E. Hosoi, and G. H. McKinley. "New measures for characterizing nonlinear viscoelasticity in large amplitude oscillatory shear". *Journal of Rheology* 52.6 (2008), 1427–1458.

[54] S. A. Rogers and M. P. Lettinga. "A sequence of physical processes determined and quantified in large-amplitude oscillatory shear (LAOS): Application to theoretical nonlinear models". *Journal of rheology* 56.1 (2012), 1–25.

[55] S. A. Rogers, B. M. Erwin, D. Vlassopoulos, and M. Cloitre. "A sequence of physical processes determined and quantified in LAOS: Application to a yield stress fluid". *Journal of Rheology* 55.2 (2011), 435–458.

[56] J. Läuger and H. Stettin. "Differences between stress and strain control in the non-linear behavior of complex fluids". *Rheologica acta* 49.9 (2010), 909–930.

[57] C. S. Cook and P. A. Smith. "Clinical update: why PRP should be your first choice for injection therapy in treating osteoarthritis of the knee". *Current reviews in musculoskeletal medicine* 11.4 (2018), 583–592.

[58] S-J. Jang, J-D. Kim, and S-S. Cha. "Platelet-rich plasma (PRP) injections as an effective treatment for early osteoarthritis". *European Journal of Orthopaedic Surgery & Traumatology* 23.5 (2013), 573–580.

[59] K. E. Whitney, A. Liebowitz, I. K. Bolia, J. Chahla, S. Ravuri, T. A. Evans, M. J. Philippon, and J. Huard. "Current perspectives on biological approaches for osteoarthritis". *Annals of the New York Academy of Sciences* 1410.1 (2017), 26–43.

[60] W. Kanchanatawan, A. Arirachakaran, K. Chaijenkij, N. Prasathaporn, M. Boonard, P. Piyapittayanun, and J. Kongtharvonskul. "Short-term outcomes of platelet-rich plasma injection for treatment of osteoarthritis of the knee". *Knee Surgery, Sports Traumatology, Arthroscopy* 24.5 (2016), 1665–1677.

[61] W. Goossens, V. Van Duppen, and R. L. Verwilghen. "K2-or K3-EDTA: the anticoagulant of choice in routine haematology?" *Clinical & Laboratory Haematology* 13.3 (1991), 291–295.

[62] Z. Huczek, J. Kochman, K. J. Filipiak, G. J. Horszczaruk, M. Grabowski, R. Piatkowski, J. Wilczynska, A. Zielinski, B. Meier, and G. Opolski. "Mean platelet volume on admission predicts impaired reperfusion and long-term mortality in acute myocardial infarction treated with primary percutaneous coronary intervention". *Journal of the American College of Cardiology* 46.2 (2005), 284–290.

[63] R. J. F. C. do Amaral, N. P. da Silva, N. F. Haddad, L. S. Lopes, F. D. Ferreira, P. A. Cappelletti, W. de Mello, E. Cordeiro-Spinetti, and A. Balduino. "Platelet-rich plasma obtained with different anticoagulants and their effect on platelet numbers and mesenchymal stromal cells behavior in vitro". *Stem cells international* 2016 (2016).

[64] H. Mani, B. Luxembourg, C. Kläffling, M. Erbe, and E Lindhoff-Last. "Use of native or platelet count adjusted platelet rich plasma for platelet aggregation measurements". *Journal of clinical pathology* 58.7 (2005), 747–750.

[65] I. Tonogai, F. Hayashi, T. Iwame, T. Takasago, T. Matsuura, and K. Sairyo. "Platelet-rich plasma does not reduce skeletal muscle fibrosis after distraction osteogenesis". *Journal of experimental orthopaedics* 5.1 (2018), 26.

[66] F. Cantini, C. Salvarani, I. Olivieri, L. Macchioni, A. Ranzi, L. Niccoli, A. Padula, and L. Boiardi. "Erythrocyte sedimentation rate and C-reactive protein

in the evaluation of disease activity and severity in polymyalgia rheumatica: a prospective follow-up study". In: *Seminars in arthritis and rheumatism*. Vol. 30. 1. Elsevier. 2000, 17–24.

[67] R. P. Chhabra and J. F. Richardson. *Non-Newtonian flow and applied rheology: engineering applications*. Butterworth-Heinemann, 2011.

[68] J. M. Clark, A. G. Norman, M. J. Kääb, and H. P. Nötzli. "The surface contour of articular cartilage in an intact, loaded joint". *The Journal of Anatomy* 195.1 (1999), 45–56.

[69] V. C. Mow, A. Ratcliffe, and S. L. Y. Woo. *Biomechanics of diarthrodial joints*. Vol. 1. Springer Science & Business Media, 2012.

[70] S. M. Taghavi, K. Alba, and I. A. Frigaard. "Buoyant miscible displacement flows at moderate viscosity ratios and low Atwood numbers in near-horizontal ducts". *Chem. Eng. Sci.* 69 (2012), 404–418.

[71] L. Dintenfass. "Internal viscosity of the red cell and a blood viscosity equation". *Nature* 219.5157 (1968), 956.

[72] G. Késmárky, P. Kenyeres, M. Rábai, and K. Tóth. "Plasma viscosity: a forgotten variable". *Clin. Hemorheol. Microcirc.* 39.1–4 (2008), 243–246.

[73] E. W. Merrill, E. R. Gilliland, T. S. Lee, and E. W. Salzman. "Blood rheology: effect of fibrinogen deduced by addition". *Circulation Research* 18.4 (1966), 437–446.

[74] E. W. Merrill, G. C. Cokelet, A. Britten, and R. E. Wells Jr. "Non-newtonian rheology of human blood-effect of fibrinogen deduced by" subtraction"". *Circulation research* 13.1 (1963), 48–55.

[75] S. Chien, S. Usami, R. J. Dellenback, and M. I. Gregersen. "Shear-dependent interaction of plasma proteins with erythrocytes in blood rheology". *American Journal of Physiology-Legacy Content* 219.1 (1970), 143–153.

[76] A. J. Apostolidis, M. J. Armstrong, and A. N. Beris. "Modeling of human blood rheology in transient shear flows". *Journal of Rheology* 59.1 (2014), 275.

[77] Z. S. Marton, G. Kesmarky, J. Vekasi, A. Cser, R. Russai, B. Horvath, and K. Toth. "Red blood cell aggregation measurements in whole blood and in fibrinogen solutions by different methods". *Clinical hemorheology and microcirculation* 24.2 (2001), 75–83.

[78] S. Chien and K-M. Jan. "Ultrastructural basis of the mechanism of rouleaux formation". *Microvascular research* 5.2 (1973), 155–166.

[79] F. Peyvandi, I. Garagiola, and L. Baronciani. "Role of von Willebrand factor in the haemostasis". *Blood Transfusion* 9.Suppl 2 (2011), s3.

[80] H. P. Sdougos, S. R. Bussolari, and C. F. Dewey. "Secondary flow and turbulence in a cone-and-plate device". *J. Fluid Mech.* 138 (1984), 379–404.

[81] Y. A. Çengel, R. H. Turner, J. M. Cimbala, and M. Kanoglu. *Fundamentals of thermal-fluid sciences*. McGraw-Hill New York, NY, 2005.

[82] B. Eslami, S. Shariatnia, H. Ghasemi, and K. Alba. "Non-isothermal buoyancy-driven exchange flows in inclined pipes". *Phys. Fluids* 29 (2017), 062108(1)–(17).

[83] A. Akpek, C. Youn, A. Maeda, N. Fujisawa, and T. Kagawa. "Effect of thermal convection on viscosity measurement in vibrational viscometer". *J. Flow Control Meas. Visual.* 2.01 (2014), 12.

[84] M. J. Simmonds, H. J. Meiselman, and O. K. Baskurt. "Blood rheology and aging". *J. Geriatr. Cardiol.* 10.3 (2013), 291.

[85] E. A. Femia, M. Pugliano, G. Podda, and M. Cattaneo. "Comparison of different procedures to prepare platelet-rich plasma for studies of platelet aggregation by light transmission aggregometry". *Platelets* 23.1 (2012), 7–10.

[86] A. Rana, E. Westein, B. Niego, and C. E. Hagemeyer. "Shear-dependent platelet aggregation: mechanisms and therapeutic opportunities". *Frontiers in cardiovascular medicine* 6 (2019).

[87] M. Brust, C. Schaefer, R. Doerr, L. Pan, M. Garcia, P. E. Arratia, and C. Wagner. "Rheology of human blood plasma: Viscoelastic versus Newtonian behavior". *Physical review letters* 110.7 (2013), 078305.

[88] J. L. Schrag. "Deviation of velocity gradient profiles from the "gap loading" and "surface loading" limits in dynamic simple shear experiments". *Trans. Soc. Rheol.* 21.3 (1977), 399–413.

[89] J. V. Shah and P. A. Janmey. "Strain hardening of fibrin gels and plasma clots". *Rheologica Acta* 36.3 (1997), 262–268.

[90] S. Tattersall. "Choke Valve Technology in Subsea Environments". *Measurement and Control* 49.3 (2016), 104–108.

[91] K. Yonezawa, R. Ogawa, K. Ogi, T. Takino, Y. Tsujimoto, T. Endo, K. Tezuka, R. Morita, and F. Inada. "Flow-induced vibration of a steam control valve". *Journal of Fluids and Structures* 35 (2012), 76–88.

[92] R. M. Baldwin and H. R. Simmons. "Flow-induced vibration in safety relief valves" (1986).

[93] J. T. Coffman and M. D. Bernstein. "Failure of safety valves due to flow-induced vibration" (1980).

[94] R. D. Blevins. "Flow-Induced Vibration Second Edition". *Florida, Krieger Publishing Co.* (1990).

[95] W. K. Blake. *Mechanics of flow-induced sound and vibration, Volume 2: Complex flow-structure interactions*. Academic press, 2017.

[96] K. Yonezawa, Y. Tsujimoto, K. Tezuka, M. Mori, R. Morita, and F. Inada. "Transonic flow vibration in a steam control valve for a power plant". *Flow Induced Vibration* (2008), 599–604.

[97] L. M. Novak. "Numerical investigation of vibration in a steam turbine control valve". PhD thesis. North Dakota State University, 2017.

[98] F. L. Eisinger and R. Sullivan. "Acoustic Power and Acoustic Pressure in Piping Systems Handling High Velocity Steam and Gases Through a Pressure Reducing Device". In: *ASME 2010 Pressure Vessels and Piping Division/K-PVP Conference*. American Society of Mechanical Engineers Digital Collection. 2010, 11–16.

[99] J. Kolenc. "Understanding the Impact of Acoustic Induced Vibration on Piping Systems". In: *2018 Spring Meeting and 14th Global Congress on Process Safety*. AIChE. 2018.

[100] R. D. Bruce, A. S. Bommer, and T. E. LePage. "Solving acoustic-induced vibration problems in the design stage". *Sound and Vibration* 47.8 (2013).

[101] M. Agar and L. Ancian. "Acoustic-induced vibration: A new methodology for improved piping design practice". In: *Offshore Technology Conference Asia*. Offshore Technology Conference. 2016.

[102] V. A. Carucci. "Acoustically induced piping vibration in high capacity pressure reducing systems". *ASME Paper 82-WA/PVP-8* (1982).

[103] M. Jaouhari. "Bechtel Oil, Gas & Chemicals, Inc. Houston, Texas, USA" (2018).

[104] S. Fu, J. Wang, R. Baarholm, J. Wu, and C. M. Larsen. "Features of vortex-induced vibration in oscillatory flow". *Journal of Offshore Mechanics and Arctic Engineering* 136.1 (2014).

[105] C. Bailly and G. Comte-Bellot. "Introduction to turbulence". In: *Turbulence*. Springer, 2015, 1–31.

[106] N. E. Ligterink, R. de Groot, E. Gharaibah, and H. J. Slot. "Flow induced vibration of subsea gas production systems caused by choke valves" (2012).

[107] C. B. Domnick, F-K. Benra, D. Brillert, H. J. Dohmen, and C. Musch. "Investigation on flow-induced vibrations of a steam turbine inlet valve considering fluid–structure interaction effects". *Journal of Engineering for Gas turbines and Power* 139.2 (2017), 022507.

[108] K. Yonezawa, K. Ogi, T. Takino, Y. Tsujimoto, T. Endo, K. Tezuka, R. Morita, and F. Inada. "Experimental and numerical investigation of flow induced vibration of steam control valve". In: *ASME 2010 3rd Joint US-European Fluids Engineering Summer Meeting collocated with 8th International Conference on Nanochannels, Microchannels, and Minichannels*. American Society of Mechanical Engineers. 2010, 575–583.

[109] R. Morita, F. Inada, M. Mori, K. Tezuka, and Y. Tsujimoto. "CFD simulations and experiments of flow fluctuations around a steam control valve". *Journal of Fluids Engineering* 129.1 (2007), 48–54.

[110] K. E. Widel. "Governing valve vibrations in a large steam turbine". *Practical Experiences with Flow-Induced Vibrations, Springer-Verlag, New York* (1980), 320–322.

[111] A. H. Shapiro. *The dynamics and thermodynamics of compressible fluid flow*. BOOK. John Wiley & Sons, 1953.

[112] M. Zingale. *Introduction to Computational Astrophysical Hydrodynamics*. 2017.

[113] K. Kubo, Y. Miyazato, and K. Matsuo. "Study of choked flows through a convergent nozzle". *Journal of Thermal Science* 19.3 (2010), 193–197.

[114] B. J. Cantwell. *Fundamentals of compressible flow*. 1996.

[115] E. Franquet, V. Perrier, S. Gibout, and P. Bruel. "Free underexpanded jets in a quiescent medium: A review". *Progress in Aerospace Sciences* 77 (2015), 25–53.

[116] S. Crist, D. R. Glass, and P. M. Sherman. "Study of the highly underexpanded sonic jet." *AIAA journal* 4.1 (1966), 68–71.

[117] R. Courant and K. O. Friedrichs. *Supersonic flow and shock waves*. Vol. 21. Springer Science & Business Media, 1999.

[118] R. Von Mises, H. Geiringer, and G. S. S. Ludford. *Mathematical theory of compressible fluid flow*. Courier Corporation, 2004.

[119] P. S. Cumber, M. Fairweather, S. Falle, and J. R. Giddings. "Predictions of the structure of turbulent, highly underexpanded jets" (1995).

[120] D-Y. Peng and D. B. Robinson. "A new two-constant equation of state". *Industrial & Engineering Chemistry Fundamentals* 15.1 (1976), 59–64.

[121] M. E. Voulgaris, C. J. Peters, and J. de Swaan Arons. "Prediction of the Condensation Behavior of Natural Gas: A Comparative Study of the Peng-Robinson and the Simplified-Perturbed-Hard-Chain Theory Equations of State". *Industrial & engineering chemistry research* 37.5 (1998), 1696–1706.

[122] R. J. Steffensen and R. C. Smith. "The importance of Joule-Thomson heating (or cooling) in temperature log interpretation". In: *Fall Meeting of the Society of Petroleum Engineers of AIME*. Society of Petroleum Engineers. 1973.

[123] J. F. App. "Field cases: nonisothermal behavior due to Joule-Thomson and transient fluid expansion/compression effects". In: *SPE Annual Technical Conference and Exhibition*. Society of Petroleum Engineers. 2009.

[124] K. Gasem, W. Gao, Z. Pan, and R. L. Robinson Jr. "A modified temperature dependence for the Peng–Robinson equation of state". *Fluid phase equilibria* 181.1-2 (2001), 113–125.

[125] Daniel. Edgington-Mitchell, D. R. Honnery, and J. Soria. "The underexpanded jet Mach disk and its associated shear layer". *Physics of Fluids* 26.9 (2014), 1578.

[126] F. Bonelli, A. Viggiano, and V. Magi. "A numerical analysis of hydrogen underexpanded jets under real gas assumption". *Journal of fluids engineering* 135.12 (2013).

[127] A. Hamzehloo and P. G. Aleiferis. "Large eddy simulation of highly turbulent under-expanded hydrogen and methane jets for gaseous-fuelled internal combustion engines". *International Journal of Hydrogen Energy* 39.36 (2014), 21275–21296.

[128] W. S. Saric. "Görtler vortices". *Annual Review of Fluid Mechanics* 26.1 (1994), 379–409.

[129] B. Andersson, R. Andersson, L. Håkansson, M. Mortensen, R. Sudiyo, and B. Van Wachem. *Computational fluid dynamics for engineers*. Cambridge University Press, 2011.

[130] F. G. Schmitt. "About Boussinesq's turbulent viscosity hypothesis: historical remarks and a direct evaluation of its validity". *Comptes Rendus Mécanique* 335.9-10 (2007), 617–627.

[131] W.P. Jones and B. E. Launder. "The prediction of laminarization with a two-equation model of turbulence". *International journal of heat and mass transfer* 15.2 (1972), 301–314.

[132] P. Spalart and S. Allmaras. "A one-equation turbulence model for aerodynamic flows". In: *30th aerospace sciences meeting and exhibit*. 1992, 439.

[133] S. Sarkar and L. Balakrishnan. "Application of a Reynolds stress turbulence model to the compressible shear layer" (1990).

[134] C.G. Speziale, S. Sarkar, and T.B. Gatski. "Modelling the pressure–strain correlation of turbulence: an invariant dynamical systems approach". *Journal of fluid mechanics* 227 (1991), 245–272.

[135] D. C. Wilcox. *Turbulence modeling for CFD*. Vol. 2. DCW industries La Canada, CA, 1998.

[136] D. C. Wilcox. "Formulation of the kw turbulence model revisited". *AIAA journal* 46.11 (2008), 2823–2838.

[137] F.R. Menter. "Two-equation eddy-viscosity turbulence models for engineering applications". *AIAA journal* 32.8 (1994), 1598–1605.

[138] F. Menter. "Zonal two equation kw turbulence models for aerodynamic flows". In: *23rd fluid dynamics, plasmadynamics, and lasers conference*. 1993, 2906.

[139] P. R. Spalart. "Comments on the feasibility of LES for wings, and on a hybrid RANS/LES approach". In: *Proceedings of first AFOSR international conference on DNS/LES*. Greyden Press. 1997.

[140] K. Hanjalić and B. E. Launder. "A Reynolds stress model of turbulence and its application to thin shear flows". *Journal of fluid Mechanics* 52.4 (1972), 609–638.

[141] A. Diring, L. Fromme, M. Petry, and E. Weizel. "Comparison Between COMSOL Multiphysics® and STAR-CCM+® Simulation Results and Experimentally Determined Measured Data for a Venturi Tube" (2017).

[142] Z. Yong, Z. Zhi, Z. Li, and W. Tianlin. "Turbulence model investigations on the boundary layer flow with adverse pressure gradients". *Journal of Marine Science and Application* 14.2 (2015), 170–174.

[143] F. R. Menter and M. Kuntz. "Adaptation of eddy-viscosity turbulence models to unsteady separated flow behind vehicles". In: *The aerodynamics of heavy vehicles: trucks, buses, and trains*. Springer, 2004, 339–352.

[144] CD Adapco. *STAR-CCM+ User's Manual*. Version 14.04.013, 2019.

[145] JH R. "Numerical Simulation of the Flow Past an Exhaust Valve in a Two-Stroke Diesel Engine". MA thesis. 2800 Kgs. Lyngby, Denmark: Technical University of Denmark, Oct. 2011.

[146] I. L. Ver and L. L. Beranek. *Noise and Vibration Control Engineering-Principles and Applications, Wiley, 2006: Noise and Vibration Control Engineering-Principles and Applications*. Vol. 1. Bukupedia, 2006.

[147] F. J. Harris. "On the use of windows for harmonic analysis with the discrete Fourier transform". *Proceedings of the IEEE* 66.1 (1978), 51–83.

[148] B. Zhang, M. Kong, and C. B. WU. "Research of spectrum leakage with window function [J]". *Informationization* 11 (2009), 10–12.

[149] B. Van Leer and P. R. Woodward. "The MUSCL code for compressible flow: philosophy and results". *TICOM Conferece* (1979).

[150] E. Shima, K. Kitamura, and T. Haga. "Green–gauss/weighted-least-squares hybrid gradient reconstruction for arbitrary polyhedra unstructured grids". *AIAA journal* 51.11 (2013), 2740–2747.

[151] J. G. Baker and J. R. van Meter. "Reducing reflections from mesh refinement interfaces in numerical relativity". *Physical Review D* 72.10 (2005), 104010.

[152] R. Vichnevetsky. "Propagation through numerical mesh refinement for hyperbolic equations" (1981).

[153] H. N. Raghavendra, M. R. Shivashankar, and P. A. Ramalingam. "Simulation of Erosion Wear in Choke Valves using CFD". In: 2014.

[154] M. Bohnet. *Ullmann's encyclopedia of industrial chemistry*. Wiley-Vch, 2003.

[155] G. Ernst, B. Keil, H. Wirbser, and M. Jaeschke. "Flow-calorimetric results for the massic heat capacitycpand the Joule–Thomson coefficient of CH4, of (0.85

CH4+ 0.15 C2H6), and of a mixture similar to natural gas". *The Journal of Chemical Thermodynamics* 33.6 (2001), 601–613.

[156] J. C. Cianca and P. Jayaram. "Musculoskeletal injuries and regenerative medicine in the elderly patient". *Phys. Med. Rehabil. Clin.* 28.4 (2017), 777–794.

[157] I. Peter, K. Wu, R. Diaz, and J. Borg-Stein. "Platelet-rich plasma". *Phys. Med. Rehabil. Clin.* 27.4 (2016), 825–853.

[158] N. Vanker and H. Ipp. "Large Unstained Cells: A Potentially Valuable Parameter in the Assessment of Immune Activation Levels in HIV Infection". *Acta haematologica* 131 (Nov. 2013), 208–212.

[159] K. D. Stone, C. Prussin, and D. D. Metcalfe. "IgE, mast cells, basophils, and eosinophils". *Journal of Allergy and Clinical Immunology* 125.2 (Feb. 2010), S73–S80.

[160] G. W. Schmid-Schonbein, Y. Y. Shih, and S. Chien. "Morphometry of human leukocytes". *Blood* 56.5 (Nov. 1980), 866–875. ISSN: 0006-4971.

[161] A. Zipursky, E. Bow, R. S. Seshadri, and E. J. Brown. "Leukocyte density and volume in normal subjects and in patients with acute lymphoblastic leukemia". *Blood* 48.3 (Sept. 1976), 361–371. ISSN: 0006-4971.

[162] M. Hu, J. Wang, H. Zhao, S. Dong, and J. Cai. "Nanostructure and nanomechanics analysis of lymphocyte using AFM: From resting, activated to apoptosis". English. *Journal of Biomechanics* 42.10 (2009). Copyright - © 2009 Elsevier Ltd; Last updated - 2018-10-06, 1513–1519.

[163] *Sajben Transonic Diffuser*. Provided by the NPARC Alliance Validation Archive and curated by JW Slater. Website is a collection of multiple works done by Sabjen M. testing transonic diffusers.

[164] T. Wang, H. Wang, and G. Tang. "Benchmarking the Star-CCM+ Compressible Flow Solver by Simulating Typical Compressible Flow Problems: A Case Study and Comparison". In: *Theory, Methodology, Tools and Applications for Modeling and Simulation of Complex Systems*. Ed. by L. Zhang, X. Song, and Y. Wu. Singapore: Springer Singapore, 2016, 379–391. ISBN: 978-981-10-2669-0.

[165] B. Apaçoğlu and S. Aradağ. "CFD Analysis of Uncontrolled and Controlled Turbulent Flow over a Circular Cylinder". In: *6th International Advanced Technologies Symposium (IATS'11)*. Vol. 16. 2011, 18.

[166] A. Travin, M. Shur, M. M. Strelets, and P. R. Spalart. "Physical and numerical upgrades in the detached-eddy simulation of complex turbulent flows". In: *Advances in LES of complex flows*. Springer, 2002, 239–254.

Appendices

A. Rheology of PRP

A.1 Cell counts & Volume Fractions

Even with identical means of preparation, PRP samples can differ from one another, a fact that has long limited widespread applicability of research studies [156]. The five different PRP samples analyzed in this study contain increasing counts of RBCs across PRP1 to PRP5. A typical PRP mixture approximately contains 5 times the platelet count as that of WB, represented as 5X. The PRP samples (1-5) in this study contained 4.94X , 8.43X, 4.40X, 5.01X, and 4.96X, respectively, and the P3 and PPP sample have platelet counts of 1.04X and 0.04X respectively; see Table A.1. This difference in RBC and platelet counts may be used to explain observed differences in rheological measurements of PRP samples. Compared to WB [157], all the PRP samples exhibit higher amounts of platelets and WBCs and reduced amount of RBCs. Since, PRP samples are essentially a suspension, defining a total volume fraction, ϕ_{total}, is convenient as

$$\phi_{total} = \phi_{RBC} + \phi_{Platelet} + \phi_{WBC}, \tag{A.1}$$

where,

$$\phi_{WBC} = \phi_{neutrophil} + \phi_{lymphocyte} + \phi_{eosinophil} + \phi_{monocyte} + \phi_{basophil} + \phi_{LUC}, \tag{A.2}$$

see values given in Table A.2. Large Unstained Cells (LUC) are made up of activated leuokocytes, and contribute approximately 0.01% to the volume fractions [158]. The ϕ for each cell was found using the count as given in Table A.1 and the corresponding average volume of each type of cell [159–162]. Fig. 3.1 shows microscopy images

Table A.1: Red blood cell (RBC), white blood cell (WBC) and platelet counts for various solutions used in this study, measured by scatter cytogram and platelet-integrated analysis.

Sample	RBC ($\times 10^6$ / μL)	WBC ($\times 10^3$ / μL)	Platelets ($\times 10^3$ / μL)
PRP1	0.23	5.45	864
PRP2	0.25	5.54	1475
PRP3	0.79	8.73	771
PRP4	1.14	12.04	878
PRP5	1.44	11.06	868
P3	0.14	1.56	183
PPP	0.02	0.02	41
WB	3.93	2.66	175

Table A.2: Evaluated volume fractions, ϕ, for the PRP samples used in this study along with P3 (diluted PRP3), PPP, and WB provided for comparison.

	PRP1	PRP2	PRP3	PRP4	PRP5	P3	PPP	WB
ϕ_{WBC}	0.30	0.15	0.24	0.34	0.31	0.04	0.0005	0.07
$\phi_{Platelet}$	0.85	1.45	0.85	0.73	0.71	0.18	0.03	0.14
ϕ_{RBC}	2.00	2.18	6.87	9.92	12.54	1.22	0.17	34.22
ϕ_{total}	3.15	3.78	7.96	10.99	13.56	1.44	0.21	34.43

of PRP3, P3, and PPP solutions identifying various existing elements within these mixture. Additionally, it should be noted that the measured mean corpuscular volume (MCV), mean platelet volume (MPV), and hemoglobin (HGB) were within $86.8 \sim 89.6$ femtoliters (fL), $7.8 \sim 9.8$ fL, and $2.5 \sim 3.6$ g/dL respectively for five different PRP samples.

A.2 PRP solutions fitting results

The fitting results from the four different rheological models as described in Sec. 2.1 are outlaid here. The fittings are performed using the MATLAB curve fitting tool. The parameters for the best achieved best fit have been described in Tables A.3-A.6.

Table A.3: Power-law model curve-fitting parameters for PRP samples at two different temperatures.

	$\hat{\kappa}$ ($\times 10^{-3}$) (Pa.s^n)	n	R^2
At 25°C			
PRP1	7.915 ± 0.444	0.7365 ± 0.0130	0.9993
PRP2	39.630 ± 0.484	0.3773 ± 0.0316	0.9752
PRP3	4.775 ± 0.614	0.8413 ± 0.0146	0.9970
PRP4	2.784 ± 0.201	0.9758 ± 0.0162	0.9994
At 37°C			
PRP1	1.899 ± 0.128	0.7365 ± 0.0130	0.9993
PRP2	21.140 ± 3.445	0.4683 ± 0.0405	0.9746
PRP3	1.838 ± 0.077	0.9842 ± 0.0093	0.9998
PRP4	2.941 ± 0.390	0.9068 ± 0.0300	0.9972

Table A.4: Casson model curve-fitting parameters for PRP samples at two different temperatures.

	$\hat{\kappa}_c$ ($\times 10^{-3}$) (Pa.s)	$\hat{\tau}_0$ ($\times 10^{-3}$) (Pa)	R^2
At 25°C			
PRP1	5.124 ± 0.014	9.875 ± 2.634	0.9943
PRP2	4.608 ± 0.031	47.950 ± 5.615	0.9687
PRP3	4.675 ± 0.069	6.968 ± 1.531	0.9982
PRP4	99.890 ± 3.69	8.162 ± 16.037	0.9903
At 37°C			
PRP1	3.380 ± 0.013	1.476 ± 0.023	0.9999
PRP2	3.679 ± 0.021	29.240 ± 3.885	0.9764
PRP3	3.461 ± 0.019	0.294 ± 3.248	0.9998
PRP4	82.690 ± 2.030	52.780 ± 8.870	0.9952

Table A.5: Herschel-Bulkely model curve-fitting parameters for PRP samples at two different temperatures.

	$\hat{\kappa}$ ($\times 10^{-3}$) (Pa.s)	$\hat{\tau}_0$ ($\times 10^{-3}$) (Pa)	n	R^2
At 25°C				
PRP1	6.556 ± 0.043	2.617 ± 1.020	0.781 ± 0.028	0.9996
PRP2	1.144 ± 1.842	32.17 ± 3.130	0.649 ± 0.068	0.9969
PRP3	3.262 ± 0.036	5.597 ± 1.331	0.923 ± 0.028	0.9991
PRP4	2.361 ± 0.166	2.467 ± 0.866	1.011 ± 0.030	0.9997
At 37°C				
PRP1	1.515 ± 0.070	1.799 ± 3.535	1.027 ± 0.010	0.9999
PRP2	6.695 ± 1.211	20.340 ± 38.650	0.716 ± 0.038	0.9965
PRP3	1.635 ± 0.114	0.816 ± 0.621	1.012 ± 0.015	0.9998
PRP4	2.034 ± 0.262	3.923 ± 1.51	0.988 ± 0.027	0.9988

Table A.6: Carreau model curve-fitting parameters for PRP samples at two different temperatures.

	$\hat{\lambda}$ (s)	$\hat{\eta}_\infty$ ($\times 10^{-3}$) (Pa.s)	$\hat{\eta}_0$ ($\times 10^{-3}$) (Pa.s)	n	R^2
At 25°C					
PRP1	5.5	1.85	21.56	0.474	0.9972
PRP2	127.7	1.66	2429	0.178	0.9979
PRP3	4.0	2.29	27.22	0.135	0.8205
PRP4	20.37	2.457	57.52	0.006	0.9213
At 37°C					
PRP1	43.6	1.47	88.13	0.010	0.9928
PRP2	99.4	2.17	1587	0.098	0.9832
PRP3	12.7	1.67	20.01	0.003	0.9520
PRP4	181.84	1.97	607.10	0.004	0.9361

B. Flow Induced Vibration

B.1 CFD Benchmarking

Our benchmarking tests consisted of four cases, where the first is for validation purpose of the STAR-CCM+ Compressible flow solver, followed by flow over an inclined airfoil. This is done to validate the shock wave capturing. This is succeeded by flow over a cylinder to gain insight into the vortex shedding phenomena and the factors that affect the flow physics. Finally, the comparison with the study performed by Yonezawal *et al.*is conducted to check for FIV dominant frequency modes within a control valve.

B.1.1 Sajben Transonic Diffuser

The first validation case examines the transonic air flow through a converging-diverging which is based on experimental data obtained by Sajben *et al.* [163]. The simulation is mostly derived from the benchmarking test case as described in the Master's thesis by June Holm Rasmussen [145]. Boundary conditions used are described in Table B.1. The dimensions of the diffuser are extracted from the NPARC Alliance Validation Archive [163], with the throat of the diffuser being 44 mm.

Table B.1: Boundary and initial conditions for the Sajben transonic diffuser simulation [163].

Inlet Pressure	134.4 kPa
Outlet Pressure	110.7 kPa
Total Inlet Temperature	227.8 K
Turbulence intensity	5%
Turbulent length scale	5 mm
Initial Pressure	110.7 kPa
Initial Temperature	277.8 K
Initial horizontal velocity	200 m/s

The volume mesh was generated as shown in Figure B.1, consisting of polyhedral cells for the main flow domain and rectangular prism layer cells along the walls, with a total cell count of 2166 cells

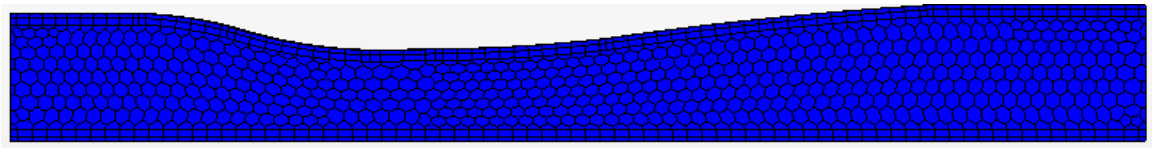

Figure B.1: The volume mesh used in Sajben transonic diffuser [163] benchmarking case using a polyhedral mesh and prism layer.

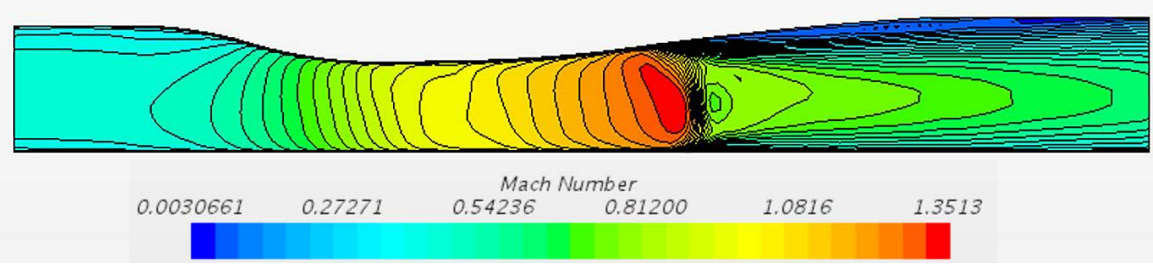

(a)

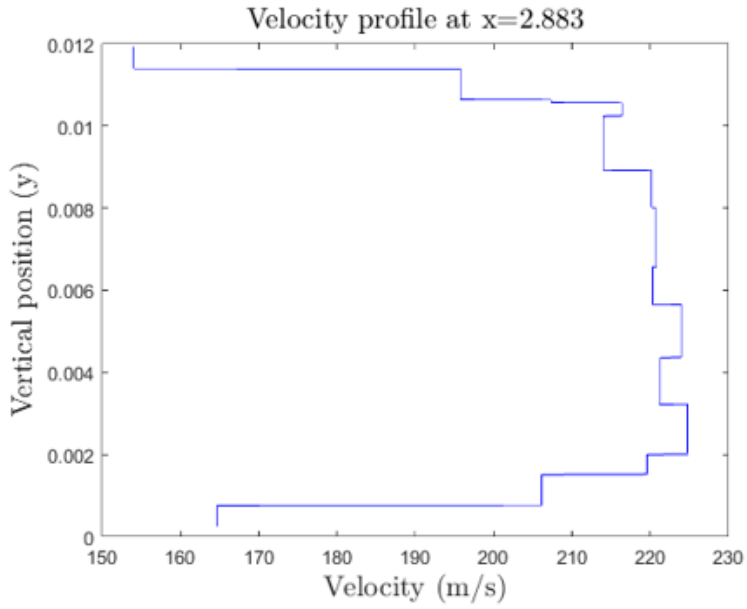

(b)

Figure B.2: (a) Mach number contours of transonic diffuser, (b) velocity profile at choke position (for comparison see Fig. 4.4a, m4 in [145]).

It should be noted that at a vertical position, $y \approx 0$, in Fig. B.2b, the velocity is

not zero. This does not satisfy the no-slip condition ascertained at the walls. This is due to the low resolution of the mesh achieved by the two prism layers at $y \approx 0$. This is because of the fact that a low y+ treatment needs a higher mesh resolution within the boundary layers.

B.1.2 Flow over an Airfoil

Flow over an airfoil is modeled in order to validate shock wave generation in the STAR-CCM+ compressible solver. Based on the simulation performed by Wang *et al.* [164] as shown below. Their study concluded that the results obtained using the STAR-CCM+ compressible solver are closest to the analytical data available in their study (see Table 1 in [164]) as compared to the other CFD software. The benchmarking results are shown in Fig. B.5 and comparable results are obtained to the Mach, pressure, and temperature contours shown by Wang *et al.* [164] (see Fig. 3 in [164]).

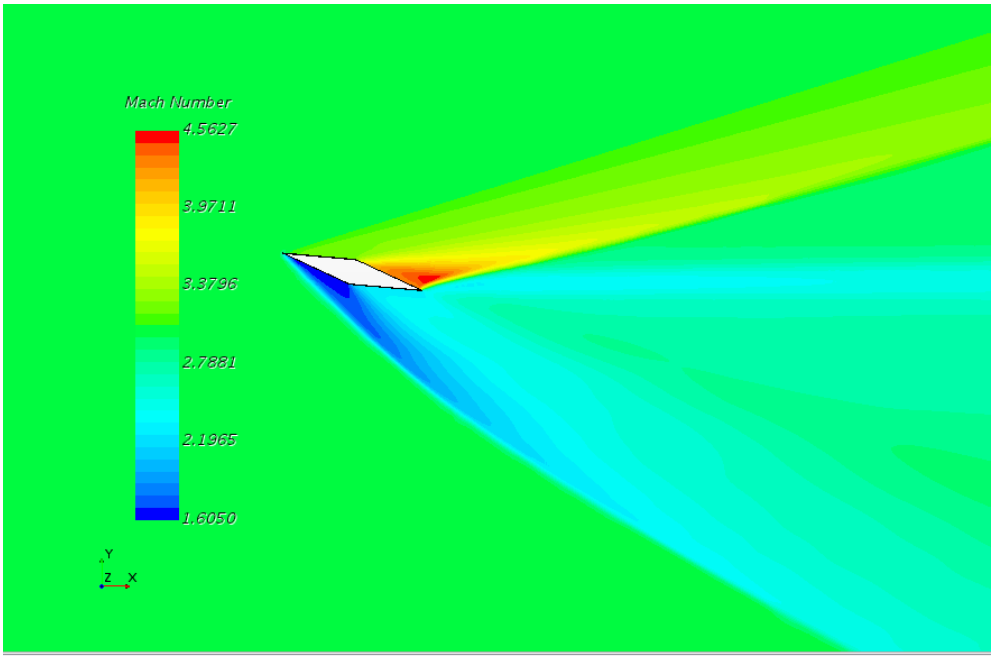

Figure B.3: Mach number contours for the airfoil design laid out by Wang *et al.* [164] and the expected shock regions created by the compressible flow over the airfoil.

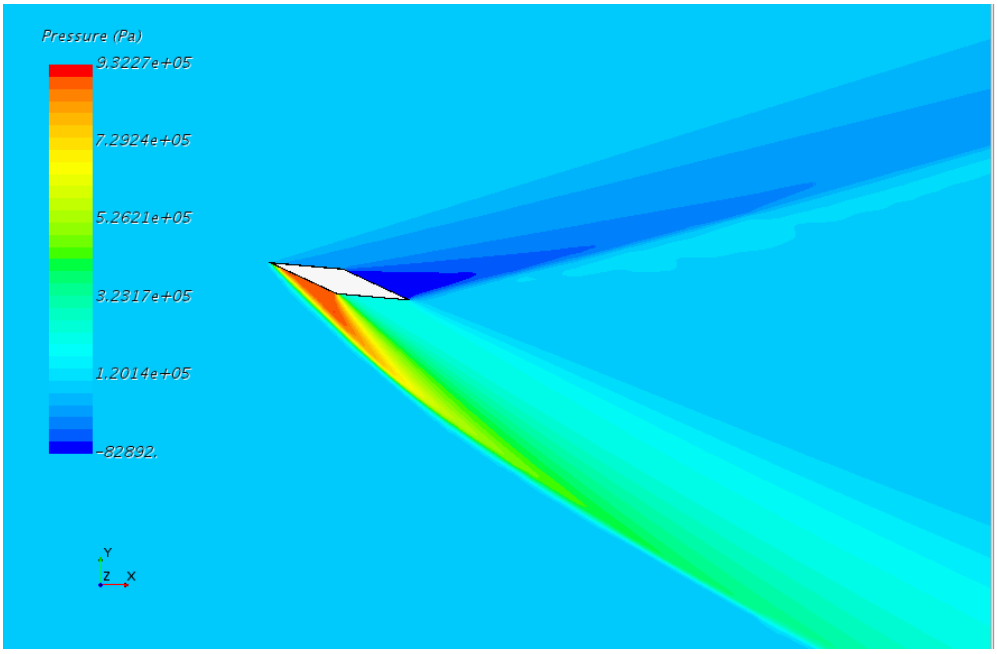

Figure B.4: Pressure contours for the airfoil benchmarking test [164].

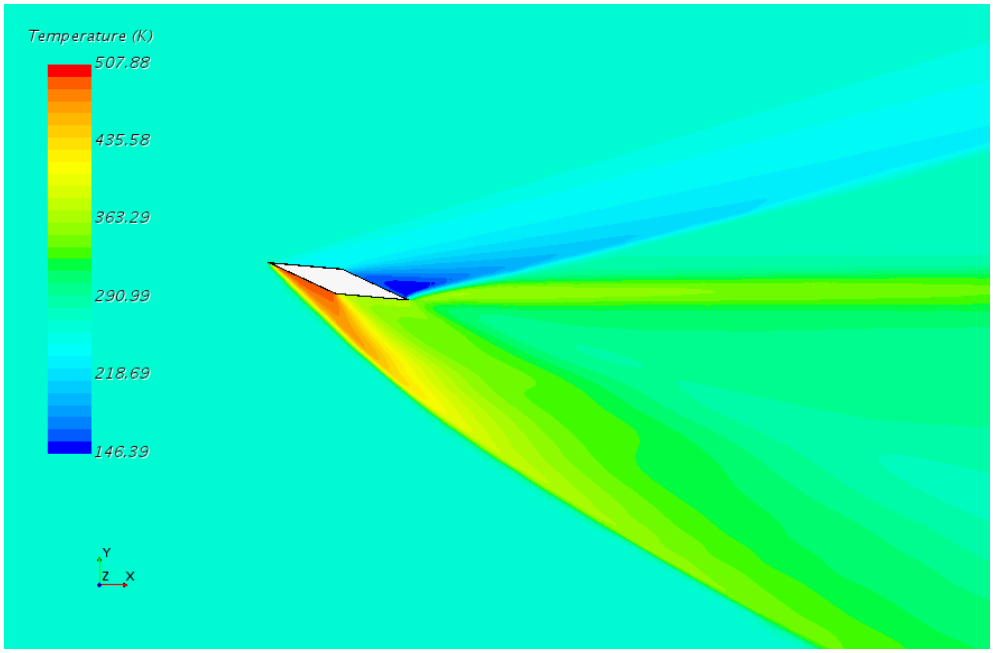

Figure B.5: Temperature contours for the airfoil bechmarking [164].

B.1.3 Flow over a Cylinder

In order to further verify whether our CFD simulations can capture the vortex shedding present in the Yonezawa *et al.*[91] and Master Flo Valve (USA) Inc. valve, we perform another classic cases of benchmarking for studying vortex shedding i.e. the flow over a 2D cylinder. Moreover, this is performed in order to gauge the sensitivity of mesh refinement at regions critical for capturing the shedding phenomenon. This simulation is based off of a paper by B. Apaçoğlu and S. Aradağ [165] and the results are closely validated against their findings. The generated mesh in our case is comparable to the one in the study performed by Apaçoğlu and Aradağ [165] and is shown in Fig. B.6. The only difference in the mesh being the use of polyhedral 2D mesh in our simulations, as compared to the tetrahedral mesh in Apaçoğlu and Aradağ's study.

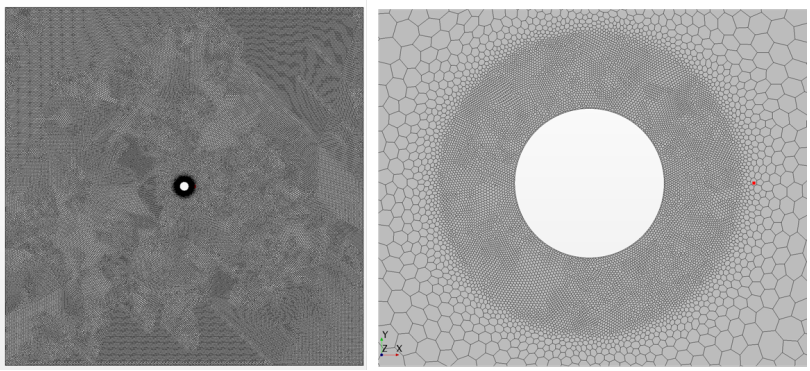

Figure B.6: Mesh structure used in benchmarking case of flow over 2D cylinder [165]: (left) over entire domain, (right) close-up of the area surrounding the cylinder.

As demonstrated in Fig. B.7, the dominant frequency of the lift coefficient oscillation is approximately 8 Hz whereas B. Apaçoğlu and S. Aradağ reported a close value of 5.5 Hz [165]. The pressure oscillations are captured and the frequency spectrum of the oscillations are represented in Fig. B.7. Vortex shedding is observed, reflecting the code's ability to capture such effect as will be seen in additional benchmarking case (B.1.4) as well as Master Flo Valve (USA) Inc. valves. Although, it should be

noted that, mesh refinement can induce heavy errors if meshed too fine or too coarse, especially near the regions of interest.

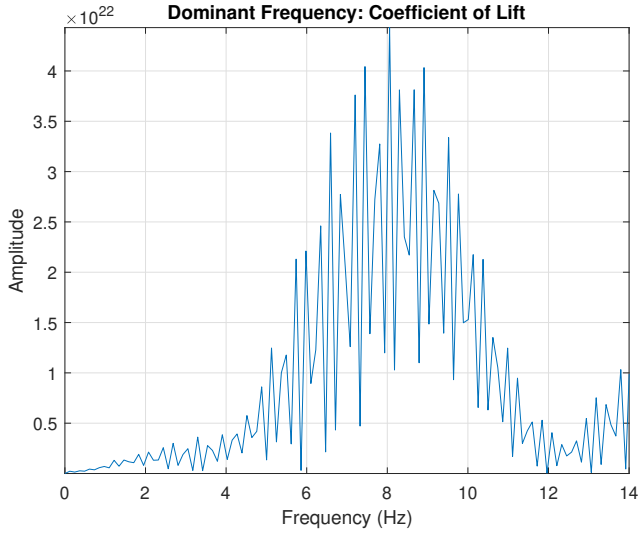

Figure B.7: Fast Fourier Transform (FFT) analysis carried out for flow over a 2D cylinder depicting a peak at approximately 8 Hz.

B.1.4 Choke valve study by Yonezawa *et al.* [91]

In order to validate whether the code can capture complex turbulent flow within control valve similar to those of Master Flo Valve (USA) Inc., we have conducted additional simulation specifically comparing against the novel study of Yonezawa *et al.* [91]. The physical model parameters are chosen such that they closely resemble those of Yonezawa *et al.* [91] study. It is worth noting though that, although STAR-CCM+ does offer fifth-order temporal discretization but is not able to allow fifth/sixth-order accurate spatial discretization schemes as adopted by customized code of Yonezawa *et al.* [91]. It is, however, reported that second-order (in space and time) accurate models can lead to acceptable results under certain circumstances [91, 96].

We have adopted a turbulent, second-order (in time) implicit unsteady flow model which utilizes a coupled solver equipped with DES and SA model to solve the NS equations for the simulation. The fluid used is air characterized as an ideal gas to

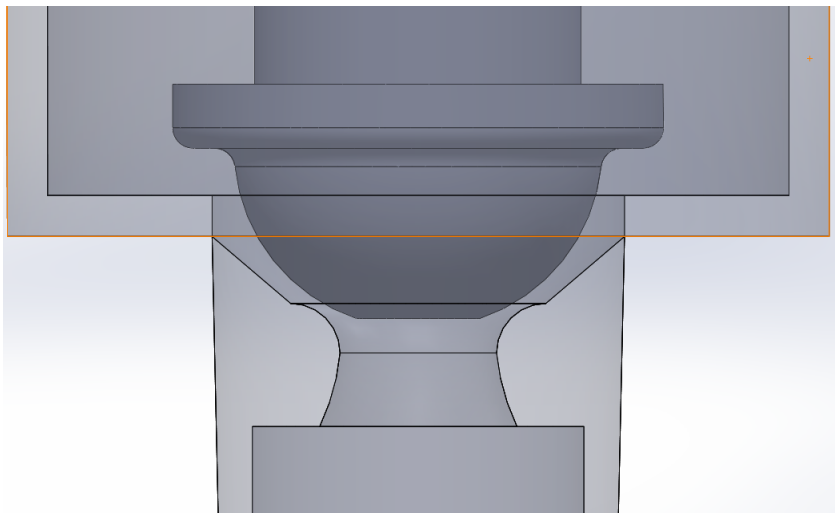

Figure B.8: The CAD model of the valve used by Yonezawa *et al.* based on the measurement provided in their paper [91]

save computational costs. Initial and flow conditions are the same as those stated by Yonezawa *et al.* [91] The valve used by Yonezawa *et al.* [91] was recreated using Solid Works. This was conducted through additional information on the design of valves provided by the thesis work of Luke Novak [97].

The mesh used has 3,297,059 cells with a base size of 0.01 m and a refinement of 5 $\times$ 10^{-4} m around the plunger head and valve seat to reduce computational costs while increasing the sensitivity close to the region of interest. The need for the refinement came apparent as the computational time on the UH Sabine cluster was many times longer with a base size of 5 $\times$ 10^{-4} and no refined area. The probes used to monitor pressure are placed in similar locations as specified by Yonezawa *et al.* relative to the center of the plunger.

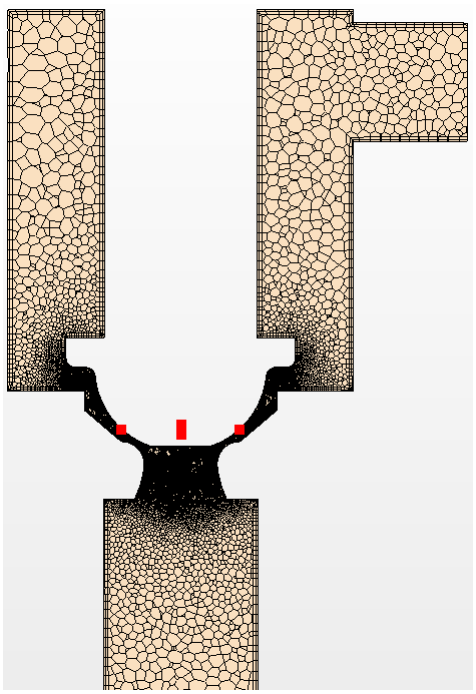

Figure B.9: Cross sectional of the 3D mesh used to benchmark against steam control valve case of Yonezawa *et al.* [91].

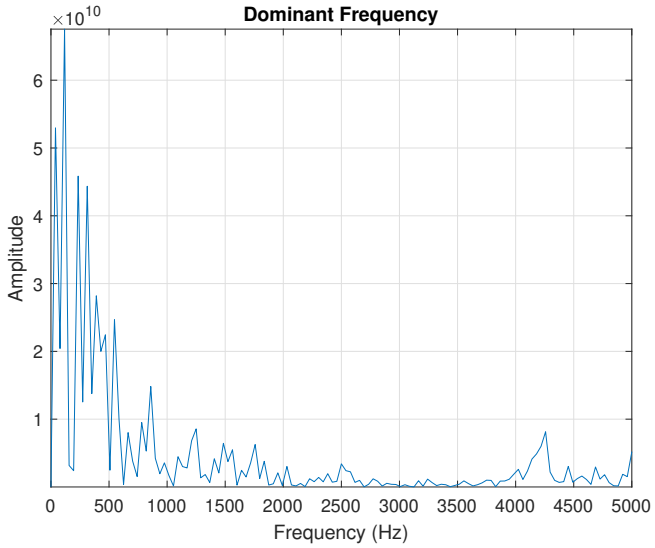

Figure B.10: FFT analysis of average pressure oscillation on plunger for steam control valve of Yonezawa *et al.* [91]

The dominant frequency found by Yonezawa *et al.* is in the range of 3500-4000 Hz. The recreated valve gives a value of 3600-4500 Hz. This difference may come from an

issue with the recreation of the Yonezawa valve used i.e. plunger position, angle of flow entrance to choked region, as well as position and size of the inlet. Although, all the information reported by Yonezawa group has been implemented. However, some parameters are missing in their work, for which the closest approximation to the best of our knowledge has been used. It also could be due to the difference in physical models available in STAR-CCM+ relative to writing a custom code as carried out in the Yonezawa *et al.* [91].

B.2 Turbulence model definitions

B.2.1 SST $\hat{k}-\hat{\omega}$ model coefficients and relations

The closure coefficients and auxiliary relations for the SST $\hat{k}-\hat{\omega}$ model are defined as [137, 138]. The production term, $\hat{P}_k$, is a sum of the turbulent production, buoyancy production, and the non-linear production, it is given by,

$$\hat{P}_k = \min\left[\hat{\tau}_{ij}\frac{\partial \hat{U}_i}{\partial \hat{x}_j}, 10\beta^*\hat{k}\hat{\omega}\right]. \tag{B.1}$$

Similarly, the other ω-production term can be defined as $\hat{P}_\omega$, and is the sum of specific dissipation production and the cross diffusion term. This has been explicitly shown in Eq. 7.29. The stress tensor term, $\hat{\tau}_{ij}$, in Eq. B.1 is defined as

$$\hat{\tau}_{ij} = \hat{\mu}_t\left(2\hat{S}_{ij} - \frac{2}{3}\frac{\partial \hat{U}_k}{\partial \hat{x}_k}\delta_{ij}\right) - \frac{2}{3}\hat{\rho}\hat{k}\delta_{ij}, \tag{B.2}$$

where,

$$\hat{S}_{ij} = \frac{1}{2}\left(\frac{\partial \hat{U}_i}{\partial \hat{x}_j} + \frac{\partial \hat{U}_j}{\partial \hat{x}_i}\right), \tag{B.3}$$

and,

$$\hat{\mu}_t = \frac{a_1\hat{\rho}\hat{k}}{\max(a_1\hat{\omega}, \hat{S}F_2)}. \tag{B.4}$$

Here, model coefficient for $\hat{k}-\hat{\omega}$, β^*, is defined as:

$$\beta^* = F_1\beta^* + (1-F_1)\beta^*. \tag{B.5}$$

The blending function, F_1, combines the near wall contribution of a coefficient with its value far away from the wall and is defined as is defined by

$$F_1 = \tanh\left\{\left[\min\left(\max\left(2\frac{\sqrt{\hat{\mathrm{k}}}}{\beta^*\hat{\omega}\hat{\mathrm{d}}}, \frac{500\hat{\nu}}{\hat{\mathrm{d}}^2\hat{\omega}}\right), \frac{4\hat{\rho}\sigma_{\omega 2}\hat{\mathrm{k}}}{\mathrm{CD}_{\mathrm{k}\omega}\hat{\mathrm{d}}^2}\right)\right]^4\right\}, \tag{B.6}$$

where, $\hat{d}$, is the distance to the wall and, $CD_{k\omega}$ is the cross-diffusion coefficient and is defined as

$$\mathrm{CD}_{k\omega} = \max\left(2\hat{\rho}\sigma_{\omega 2}\frac{1}{\hat{\omega}}\frac{\partial\hat{k}}{\partial\hat{x}_j}\frac{\partial\hat{\omega}}{\partial\hat{x}_j}, 10^{-20}\right), \tag{B.7}$$

F_2, a second blending function calculated as

$$F_2 = \tanh\left\{\left[\max\left(2\frac{\sqrt{\hat{k}}}{\beta^*\hat{\omega}\hat{d}}, \frac{500\hat{\nu}}{\hat{d}^2\hat{\omega}}\right)\right]^2\right\}. \tag{B.8}$$

Here, the values are, $\beta_1 = \frac{3}{40}$, $\beta_2 = 0.0828$, $a_1 = 0.31$, $\alpha = \alpha_1 = \frac{5}{9}$, $\alpha_2 = 0.44$, $\sigma_{k1} = 0.85$, $\sigma_{k2} = 1$, $\sigma_{\omega 1} = 0.5$, and $\sigma_{\omega 2} = 0.856$. More comprehensive definitions and relations of the terms can be found in the STAR-CCM+ user manual [144].

B.2.2 DDES SST $\hat{k}-\hat{\omega}$ model coefficients and relations

Based on the work of Menter and Kuntz [143], $\hat{l}_{ratio}$, $\hat{l}_{RANS}$, and, $\hat{l}_{LES}$, are defined as:

$$\begin{aligned} l_{ratio} &= \frac{\hat{l}_{RANS}}{\hat{l}_{LES}}, \\ \hat{l}_{RANS} &= \frac{\sqrt{\hat{k}}}{f_{\beta^*}\beta^*\hat{\omega}}, \\ \hat{l}_{LES} &= C_{DES}\hat{\Delta}, \end{aligned} \tag{B.9}$$

where, f_{β^*}, is the free-shear modification factor, β^*, is a model coefficient for $\hat{k}-\hat{\omega}$, and, $\hat{\Delta}$, is the largest distance between the cell center under consideration and the centers of the neighboring cells. The free-shear modification factor, f_{β^*}, is defined by:

$$f_{\beta^*} = \begin{cases} 1 & \text{for } \chi_k \leq 0 \\ \frac{1+680{\chi_k}^2}{1+400{\chi_k}^2} & \text{for } \chi_k > 0 \end{cases} \tag{B.10}$$

In the above equation, χ_k, is the ratio as defined below,

$$\chi_k = \frac{\nabla\hat{k} \cdot \nabla\hat{\omega}}{\hat{\omega}^3}. \tag{B.11}$$

Using the blending factor from Eq. B.8,

$$F = 1 - F_2. \tag{B.12}$$

The model coefficient, C_{DES}, which is used for blending the values obtained from the independent calibration of $\hat{k}-\hat{\epsilon}$ and $\hat{k}-\hat{\omega}$ parts of the SST $\hat{k}-\hat{\omega}$ model [166], is evaluated as

$$C_{DES} = C_{DES,\hat{k}-\hat{\omega}} F_1 + C_{DES,\hat{k}-\hat{\epsilon}} F_1(1-F_1), \tag{B.13}$$

where the model coefficients, $C_{DES,\hat{k}-\hat{\omega}}$, and , $C_{DES,\hat{k}-\hat{\epsilon}}$, are equal to 0.78 and 0.61 respectively.